Theory of Quantum Transport and Molecular Electronics

Wafa Mohammed Al Malki

Ph.D. Thesis in Physics

Department of Physics, Lancaster University, UK

Declaration

I certify that the work in this dissertation is a record of original and independent effort by the author during the period from April 2019 to September 2022 at the Department of Physics, Lancaster University, UK, under the supervision of Professor Colin J. Lambert and Dr. Iain M. Grace and funded by Taif University, KSA. I further declare that this thesis has not been previously submitted in part or full for the award of a higher degree elsewhere, and the information derived from the literature has been duly acknowledged in the text and a list of references provided.

Wafa Al Malki

September 2022

Dedication

To my late parents

The reason for what I become today

May Allah bless your souls

and grant you a place in heaven

Acknowledgments

Above all, my great thanks to ALLAH for his mercy and blessing.

Then, I would like to acknowledge and give my warmest thanks to my supervisor, Professor Colin J. Lambert for excellent supervision and all his great effort and time spent in tutorials to share with us his immense knowledge regarding molecular electronics. I really appreciate his kindness and patience to explain in detail any question related to that, and I am grateful to him for allowing me to join his group and benefit of his extensive experience, which always inspire and motivate me.

Furthermore, I would like to thank my Deputy Supervisor, Dr. Iain M. Grace, who gave me a lot of help on my work. This thesis would not be completed without his excellent guidance, patience, useful discussion and feedback. The tutorials he delivered provide me a deep understanding of SIESTA, GOLLUM and Fortran codes, which would be really helpful for my future study and research. Also, I would like to thank all my friends and colleagues in Colin's group for their cooperation and help.

My sincere thanks also go to my sponsor, the Saudi Ministry of Higher Education, Saudi culture mission in London and Taif University in Saudi Arabia, for given me this opportunity to study a Ph.D. in the United Kingdom.

Finally, I would like to express a deep sense of gratitude to my beloved husband and son. There are not enough words to explain how grateful I am for all you have done for me. I could never have reached this stage without your continuous support, tolerance and understanding.

Abstract

This thesis has investigated the electronic properties of organic molecular junctions, which form gold|single-molecule|gold structures, using a combination of density functional theory (DFT) and the equilibrium Green's function formalism of transport theory. The first project considers the role of symmetric and asymmetric anchor groups for controlling charge transfer in molecular junctions, and how that relates to the position of the electrode Fermi level relative to the molecular resonances through various molecules. The results indicated that symmetric anchors such as thiol and pyridyl yield pinning of the electrode Fermi level to the resonances, whereas this pinning behaviour does not appear with asymmetric anchors such as pyridyl and SMe. It is found that changing the basis set has no effect on the transmission curves, when the pinning occurs, and that is likely due to the shape of the gold surface. This behaviour does not occur in the absence of the tip gold with using SAMs approach, which clarifies that the shape of the electrode plays a role in controlling the relative position of its Fermi energy.

The second project concentrates on studying the effect of vibrations of the molecule on electron transport, and how it controls the value of the Seebeck coefficient. Different side groups are investigated for a series of fluorene-based molecules. The results indicated that the Seebeck coefficient of meta-connected molecules is more sensitive to the fluctuations of the side groups compared to the para case, which means that varying the pendant groups in molecular junctions can be exploited to control quantum interference (QI) and enhance the thermoelectric properties. Although C≡C and C≡N pendant groups behave similarly at room temperature, the transmission behaviour of the whole molecules different, where most of the curves in the C≡N case have this parallel shape (i.e., the anti-resonance is alleviated), leading to more enhancement in the Seebeck. In contrast, a less rigid pendant group such as $C_{13}(F_5)_2$ results in a large shift of the resonances causing broader conductance and Seebeck distributions. It is

believed that the charge distribution of fluorine atoms could produce a gating environment on the backbone of the molecule leading to this large shift.

The final project investigates the electron transport behaviour of para and meta connected molecules with and without the metal atoms, due to the presence of $PdCl_2$. Introducing a metal atom into the path of the molecule creates another transmission path, which may play a role in disrupting or changing the QI. The complex structure of these molecules leads to multiple binding locations for attachment to gold electrodes and therefore multiple junction configurations can be formed. The results showed that the addition of the palladium with the chlorine atoms to the ligand molecules enhanced the conductance for both connectivities through the SMe anchor group due to the shift of the LUMO resonance to the Fermi energy. However, the different junction geometries do not enhance the Seebeck value.

Table of Contents

List of abbreviations

TTF   Tetrathiafulvalene

TCNQ   Tetracyanoquinodimethane

AFM   Atomic Force Microscope

STM   Scanning Tunnelling Microscopy

MCBJ   Mechanically Controllable Break-Junction

QI   Quantum Interference

CQI   Constructive Quantum Interference

DQI   Destructive Quantum Interference

HOMO   Highest Occupied Molecular Orbital

LUMO   Lowest Unoccupied Molecular Orbital

DFT   Density Functional Theory

SIESTA   Spanish Initiative for Electronic Simulations with Thousands of Atoms

LDA   Local Density Approximation

GGA   Generalized Gradient Approximation

DZ   Double-ξ basis set

DZP   Double- ξ polarized basis set

$T(E)$ Transmission coefficient

G Electrical conductance

S Seebeck Coefficient

ZT   Thermoelectric figure of merit

E_F Electrode Fermi energy

SAM   Self-Assembled Monolayer

Chapter 1

Introduction and Background

1.1. Molecular Electronics

Today's world is so surrounded by electronic devices that it is difficult to imagine life without them. There has been a significant advancement in computer efficiency, speed and size from the earliest computers (ENIAC, 1947) to modern laptops. The evolution of transistor technology with the ability to increase its number into a small area of a single piece of an integrated circuit are the key to understand this startlingly rapid improvement. This miniaturisation process to build small silicon-based electronic devices has been predicted by Moore's Law in 1965 [1]. However, the continuing trend in scaling down the dimensions of the transistors towards the molecular level is extremely challenging [2] and requiring an enormous effort both technologically and economically. Therefore, the exploration of alternative fabrication methods is demanded to achieve future generations of electronic devices. The area of molecular electronics, which builds systems from atoms or molecules, could be a promising candidate as active components, providing the required size, flexibility of design, and vast availability using facile bulk synthesis [2].

Molecular electronics might offer various advantages over conventional solid state electronic devices. The diminutive size of molecules means that their utilisation as electronic circuits within devices at the nanoscale level, i.e. several nanometres, is extremely attractive, especially in relation to the cost-effectiveness of scaled-up synthesis, and their capacity to self-form onto surfaces during which the molecular components self-configure into regular conformations via

non-covalent attachments. Chemists can create a wide variety of molecular structures, allowing for rational and systematic modification of molecule properties. As a result, new effects and physical phenomena not seen in conventional materials have been discovered, such as quantum interference. For industrial purposes, some compounds can be easily produced in large quantities, potentially leading to low-cost manufacturing. Furthermore, silicon circuits lose current and heat at the nanoscale, making them inefficient, and on the other hand, a good molecular wire would diminish the transit period of typical transistors ($\sim 10^{-14}$ s), decreasing the time required for a procedure [3]. Nevertheless, appreciation of a single molecule's characteristics is paramount in order to produce molecular devices, as the capacity to utilise a particular intermolecular engagement and to build such devices without error whilst governing the electron transfer between the molecule and the electrodes is complex, owing to the molecular size and the lack of stability at elevated temperatures.

1.2. History of Molecular Electronics

The idea that organic molecules can be used in electrical circuits firstly proposed in the late 1950s [4], but the first serious attempt which sparked this filed was published by Aviram and Ratner in 1974. They discussed theoretically the idea of a molecular rectifier, behaving like a p-n junction, in which an individual molecule containing an electron donor unit, tetrathiafulvalene (TTF) and an electron acceptor unit, tetracyanoquinodimethane (TCNQ), separated by a rigid alkane bridge as an insulator to disconnect the π orbitals of the donor and acceptor groups [5]. Shortly afterwards, additional interest in this sphere was generated following the innovation of scanning tunnelling (STM) and atomic force (AFM) microscopies, in the latter part of the 1980s. Following the work of Aviram, in 1995, Joachim and Gimzewski [6] reported the initial quantification data relating to the conductance of a single molecule using

an STM-based method. Reed and Tour (1997) subsequently documented the initial transport study evaluating single-molecule junctions; these scientists employed a mechanical break junction technique, attaching two electrodes constructed using gold to a molecular conductor (1,4-benzenedithiol). This generated a symmetrical configuration that could, theoretically, be incorporated into more involved circuitry [7]. Despite the fact that this measurement has shed a great deal of light on how charges move via molecular junctions, important details about the electrical structure cannot be gleaned just from conductance properties. As an example, the p-type or n-type of molecular junctions. Therefore in 2007, Reddy's group [8] were the first who measured the Seebeck coefficients of benzenedithiol, dibezenedithiol and tribenzenedithiol using STM break junction in order to provide information about the sign of charge carrier and the relative position of the electrode Fermi energy with respect to the HOMO and LUMO levels.

Currently, there is swift progress within the sphere of molecular electronics, from both experimental and academic perspectives in relation to single-molecule junctions derived from metal-molecule-metal templates. Numerous methodologies have been designed in order to explore these systems. Such techniques encompass scanning tunnelling microscopy break-junction (STM-BJ) [9] and mechanically controllable break-junction (MCBJ) [10], wherein both are based on thousands repeating formation/breaking of single-molecule junctions.

The advances in hypothetical strategies together with practical studies offer dependable and high standard techniques for computing the electronic configuration of atomic entities. Moreover, the combination of the theory with the experimental data has provided essential feedback to obtain a more accurate descriptions of molecular junctions and established a route for comprehending the characteristics of electron transport within these molecular junctions. These devices can be appraised using the mixture of academic knowledge and experimental data; the ultimate objective is to enhance the chemical structure in order to offer the most

effective electrical and thermal transport properties for making high performance thermoelectric materials.

1.3. Molecular Junctions
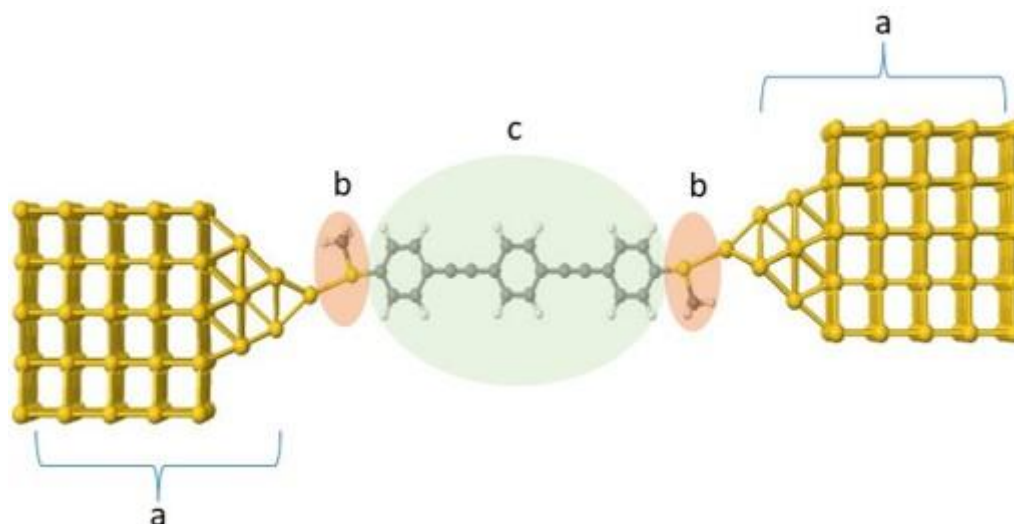
Figure (1.2): Schematic representing a molecular junction comprising: (a) left and right electrodes; (b) linker; and (c) core molecule. In this example, the electrodes are gold, a methyl sulfide (-SMe) is employed as the anchor group, and the central molecule is oligo (phenylene-ethynylene) (OPE).

The term 'molecular junction' refers to the extended metal-molecule-metal configuration. Such a system includes left and right electrodes, linkers or anchor groups, and the core molecule, as illustrated in figure (1.2). One of the most important components in building good molecule-electrode contacts is the electrode material choice. Non-metallic electrode, such as graphene, considered to be a good electrode candidate for molecular junctions. It has been the subject of numerous studies in organic-based electronics [11]–[13]. The graphene material is a highly

stable two-dimensional structure composed of covalently bonded carbon atoms; a π-conjugated configuration confers notable stability and chemical plasticity with high thermal conductivity. In contrast, metallic electrodes are most frequently chosen, such as gold, silver, copper and platinum [14], [15]. Gold is often preferred due to its chemical inertness in reactions, chemical stability, significant conductivity, and the fact that it is straightforward to construct into numerous formats that facilitate studies. It also has well-developed self-assembling methods with molecules [16]. The second important element for building molecule-electrode contacts is the anchoring groups. The chemical nature of the anchor group is selected based on the characteristics of the electrodes, so a chemical reaction can occur between the molecule and the electrode by forming a chemical bond. Numerous molecular junctions have been evaluated in the presence of gold electrodes, incorporating a range of anchoring groups [17]–[19], such as amine ($-NH_2$), thiol ($-SH$), pyridine ($-C_5H_4N$) or nitro ($-NO_2$), which can be defined as an atom, or a group of atoms, that are chemically introduced into both ends of a molecular wire to bind to the source and drain electrodes and enable transport through the molecule. The chemical binding group's nature has a significant impact on the charge distribution across a molecular junction and the ultimate energy level alignment (i.e., the relative locations of the HOMO/LUMO to the electrode Fermi level), and this will be more discussed in chapter 4. Finally, as part of the process of designing a molecule-electrode contact, the backbone or the bridge of the molecule can be modified by manipulating molecular structures or conformations, depending on the goal or the desired outcome for the studied system.

One of the major challenges in single molecule junction research is understanding the relationships between molecular structure and electronic transport characteristics. Employing DFT molecular dynamics (MD) on molecular junctions at room temperature is a computational strategy that can capture some of the conformational variability inherent to the experiments, such as bond-making/breaking events, compression and extension of the molecule (vibrational

frequencies) and variation of the molecular dihedral angles. All these aspects play a role in controlling the transport characteristics. As an example, Au-alkanedithiol-Au junction has been extensively studied to investigate the effect of the stretching of the junction on the conductance during the MD simulations [20], [21]. As the junction is being stretched, the molecule is initially bonded to the electrodes through the anchor and then mechanically extended until it breaks. Thus, when the molecule is compressed at the beginning of pulling, gauche conformations with low conductance features are adopted, but as the molecule is pulled into a straight alkane chain, these gauche defects disappear, leading to an increase in the conductance. The fluctuations of Au-S bond, which anchors the molecule to the gold surface, allow multiple coordination geometries, and junction compression or elongation during the MD process are all have influences on the changes in the conductance and Seebeck behaviours. In chapter 5, I will investigate the vibrational effect of fluorene-based molecule having different side groups using MD simulation. The addition of side group(s) can play a role in changing or tunning the single molecule conductance without modifying the molecular backbone structure. In an alkene chain, for example, the stick-loop side group can be adjusted to produce constructive and destructive interference patterns [22]. Moreover, Sadeghi et al. [23] obtained that the QI can be tuned to give low or high conductance (switching behaviour) by only varying the position and conformation of side groups in OPE-derived molecules. The side group with the presence of QI can also create a Fano resonance which will be discussed in the following section.

1.4. Quantum Interference

Quantum interference (QI) effects have been the subject of considerable attention within the domain of charge transport in experimental work at the single molecule level as they offer a unique opportunity to tune the charge transport through molecular devices and materials at the

phase-coherent scale [24]–[26]. QI can promote or diminish conductance within the molecular system, effects referred to as constructive (CQI) or destructive (DQI) quantum interference, respectively [27]. Both academic and practical work have been conducted in relation to QI since 1988. A straightforward configuration has been employed to assess QI, i.e., a benzene ring with para and meta connection patterns (figures 1.3 and 1.4) within a tight binding model. In this example, a quantum interference feature occurs when electrons with energy E transport through multiple paths from an origin to another point in the ring and upon arrival at the point of interest, they merge or superimpose. When the wave functions from the different pathways are in phase, constructive interference will take place, in contrast, out of phase (i.e. one wave has a phase shift of π) will give rise to destructive interference cancelling the transmission at a specific energy (i.e. a zero-transmission node in the HOMO-LUMO gap).

Quantum Interference effects are also present in the case of molecules with pendant groups. Figure 1.5 shows a simple linear chain with a single site attached. The resulting transmission in figure (1.6) shows three Breit-Wigner peaks, which are related to the three atomic orbitals of the sites ε_1, whereas the peak (resonance) at $E = 0.9$ and the dip (anti-resonance) at $E = \varepsilon_b$ are called a Fano resonance. The Fano resonance is formed of a resonance followed by an anti-resonance [28] due to the interference between the discrete state ε_b (the pendant group) and the continuum state ε_1 (figure 1.5). This type of resonance is of strong interest in designing molecules for use in thermoelectric materials since it can lead to an enhancement of the efficiency in single molecule devices [29] if its peak is at the Fermi level.

The room temperature QI in molecular junctions, particularly the anti-resonance, can be exploited to increase the efficiency of molecular components through enhanced molecular Seebeck coefficients [30], [31], with the aim of shifting its position towards the metallic electrodes Fermi level. In other words, boosting the thermopower (Seebeck coefficient) of a molecular junction can be achieved if the electrode Fermi energy coincides with a steep slope

of the electron transmission coefficient $T(E)$. There are different strategies to improve the Seebeck coefficient S [30], one of which is by controlling the position of intra-molecular energy levels via manipulating the side groups, which has been investigated more in chapter 5.
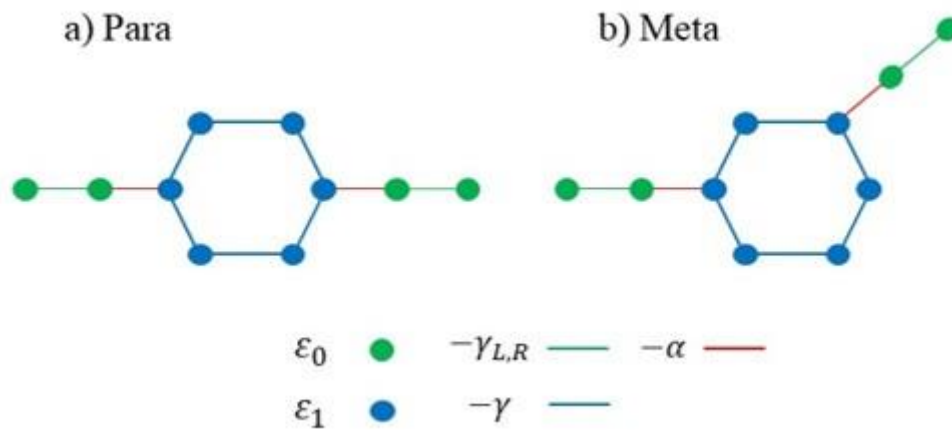

Figure (1.3): A 6-atom ring (equivalent to a benzene molecule), which is linked to left and right electrodes with different types of connection patterns: a) para and b) meta, where ε_0 and ε_1 refer to the site energies of the atoms in the leads and the molecule, respectively, and $-\gamma_{L,R}$, $-\gamma$ and $-\alpha$ represent the coupling between them.
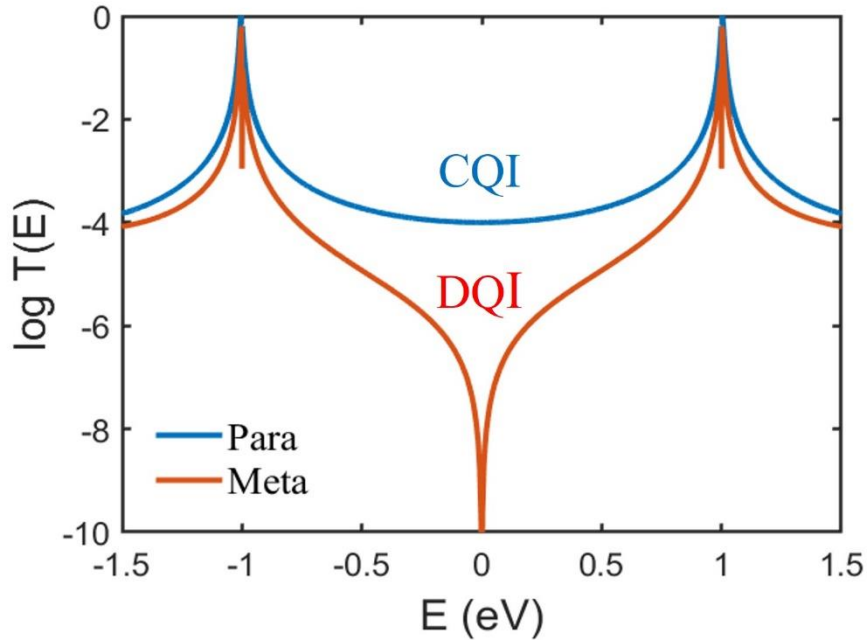
Figure (1.4): Constructive and destructive transmission curves of the benzene ring shown in the above figure due to para and meta connectivities, respectively.
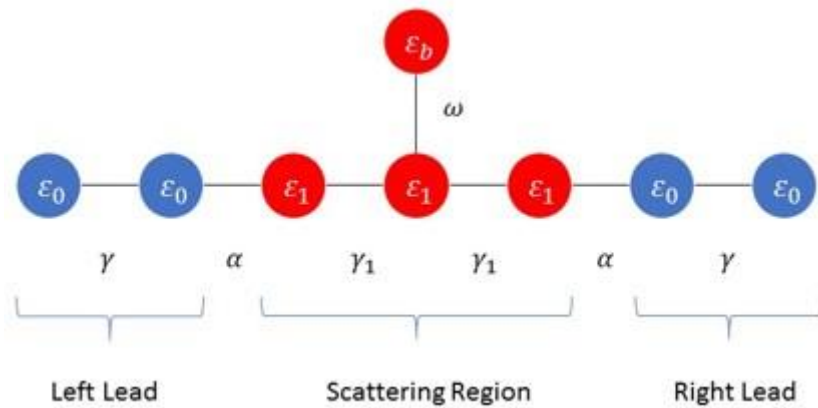
Figure (1.5): A 1-dimensional system consisting of delocalized molecular orbitals (ε_1) connected by a coupling α to left and right electrodes with a site energy (ε_0) and hopping element γ, where a discrete energy level (ε_b) is localized and weakly coupled by the bond (ω) to the linear chain system.
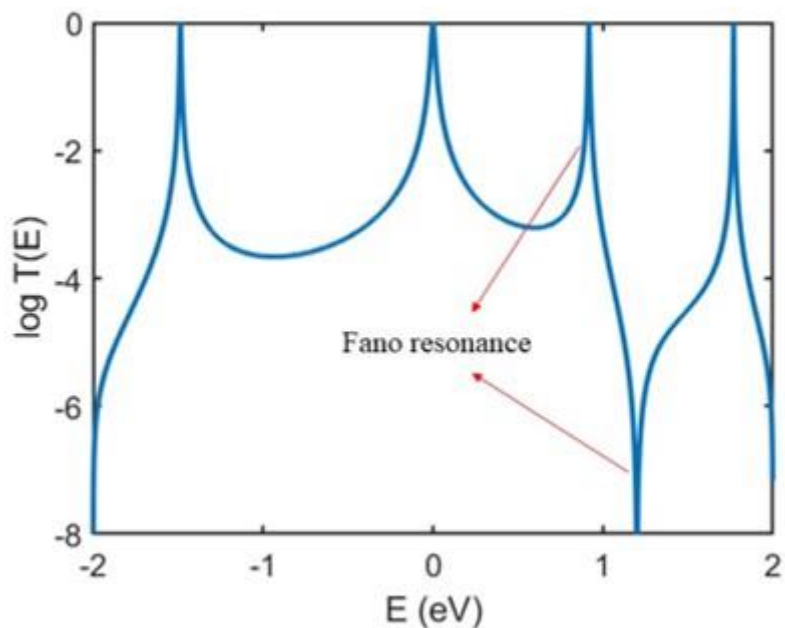
Figure (1.6): The transmission coefficient of the dangling system in figure 1.4, where the Fano resonance occurs.

1.4. Thesis Outline

The aim of the research presented in this dissertation is to investigate electron transfer within molecular junctions. The theoretical strategies include two key approaches: density functional theory (DFT) in combination with the equilibrium Green's function formalism of transport. Chapter 2 discusses the physical theories that have been extended and developed to investigate and understand the electronic properties of molecules, starting by simplifying the Schrödinger equation using Born-Oppenheimer approximation and ending with Hohenberg-Kohn and Kohn-Sham theorems, which led to substantial progress in converting DFT to a data processing code (SIESTA) and hence opened the door to applications for actual physical systems. Next, as an introduction to molecular junctions, which are made up of a single molecule bridging two macroscopic electrodes, the flow of electrical currents through a single molecule can be studied

via a one-dimensional scattering problem. Thus, the transport theory of molecular junction based on scattering theory and the Green's function technique to calculate the transmission function are investigated in chapter 3. Chapter 4 looks at the role of anchor groups, and how they control the charge transfer in a molecular junction, as well as how this relates to the relative location of the electrode Fermi level to molecular resonances. From this investigation, it is found that the structure of the junction (the shape of the leads) plays a role on the relative position of the electrode Fermi level. In chapter 5, I focus on quantum interference effects in para and meta compounds, with different pendant groups. Besides the connectivity effect, I investigate the vibrational effects of the pendant groups in electron transport through single molecule junctions. These effects are important and can enhance the Seebeck coefficient. Varying the side groups with meta connectivity is shown to have a profound influence on the transport characteristics of a molecular junction. Chapter 6 studies the transport properties of para and meta connected molecules with and without the metal atom of $PdCl_2$. The results reveal that the inclusion of this metal atom in molecular wires causes a shifting of the LUMO resonance closer to the DFT calculated Fermi energy, resulting in small enhancement in the conductance. Finally, this thesis is concluded with a summary and future works in chapter 7.

Bibliography

[1]   Moore, G.E., 1965. Cramming more components onto integrated circuits. pp.114-117.

[2]   Xiang, D., Wang, X., Jia, C., Lee, T. and Guo, X., 2016. Molecular-scale electronics: from concept to function. *Chemical reviews*, *116*(7), pp.4318-4440.

[3]   Cuevas, J.C. and Scheer, E., 2017. The Birth of Molecular Electronics. *Molecular Electronics: An Introduction to Theory and Experiment*, pp.3-17.

[4]   Hush, N.S., 2003. An overview of the first half-century of molecular electronics. *Annals of the New York Academy of Sciences*, *1006*(1), pp.1-20.

[5]   Aviram, A. and Ratner, M.A., 1974. Molecular rectifiers. *Chemical physics letters*, *29*(2), pp.277-283.

[6]   Joachim, C., Gimzewski, J.K., Schlittler, R.R. and Chavy, C., 1995. Electronic transparence of a single C 60 molecule. *Physical review letters*, *74*(11), p.2102.

[7]   Reed, M.A., Zhou, C., Muller, C.J., Burgin, T.P. and Tour, J.M., 1997. Conductance of a molecular junction. *Science*, *278*(5336), pp.252-254.

[8]   Reddy, P., Jang, S.Y., Segalman, R.A. and Majumdar, A., 2007. Thermoelectricity in molecular junctions. *Science*, *315*(5818), pp.1568-1571.

[9]   Binnig, G. and Rohrer, H., 1987. Scanning tunneling microscopy—from birth to adolescence (Nobel Lecture). *Angewandte Chemie International Edition in English*, *26*(7), pp.606-614.

[10]   Moreland, J. and Ekin, J.W., 1985. Electron tunneling experiments using Nb-Sn ''break''junctions. *Journal of applied physics*, *58*(10), pp.3888-3895.

[11]   Liu, J., Yin, Z., Cao, X., Zhao, F., Lin, A., Xie, L., Fan, Q., Boey, F., Zhang, H. and Huang, W., 2010. Bulk heterojunction polymer memory devices with reduced graphene oxide as electrodes. *ACS nano*, *4*(7), pp.3987-3992.

[12]   Di, C.A., Wei, D., Yu, G., Liu, Y., Guo, Y. and Zhu, D., 2008. Patterned graphene as source/drain electrodes for bottom-contact organic field-effect transistors. *Advanced Materials*, *20*(17), pp.3289-3293.

[13]   Jo, G., Choe, M., Cho, C.Y., Kim, J.H., Park, W., Lee, S., Hong, W.K., Kim, T.W., Park, S.J., Hong, B.H. and Kahng, Y.H., 2010. Large-scale patterned multi-layer graphene films as transparent conducting electrodes for GaN light-emitting diodes. *Nanotechnology*, *21*(17), p.175201.

[14]   Kiguchi, M., Miura, S., Takahashi, T., Hara, K., Sawamura, M. and Murakoshi, K., 2008. Conductance of single 1, 4-benzenediamine molecule bridging between Au and Pt electrodes. *The Journal of Physical Chemistry C*, *112*(35), pp.13349-13352.

[15]   Nakazumi, T., Kaneko, S. and Kiguchi, M., 2014. Electron transport properties of Au, Ag, and Cu atomic contacts in a hydrogen environment. *The Journal of Physical Chemistry C*, *118*(14), pp.7489-7493.

[16]   Jia, C. and Guo, X., 2013. Molecule–electrode interfaces in molecular electronic devices. *Chemical Society Reviews*, *42*(13), pp.5642-5660.

[17]   Frei, M., Aradhya, S.V., Hybertsen, M.S. and Venkataraman, L., 2012. Linker dependent bond rupture force measurements in single-molecule junctions. *Journal of the American Chemical Society*, *134*(9), pp.4003-4006.

[18]   Park, Y.S., Whalley, A.C., Kamenetska, M., Steigerwald, M.L., Hybertsen, M.S., Nuckolls, C. and Venkataraman, L., 2007. Contact chemistry and single-molecule conductance: a comparison of phosphines, methyl sulfides, and amines. *Journal of the American Chemical Society*, *129*(51), pp.15768-15769.

[19]   Kamenetska, M., Quek, S.Y., Whalley, A.C., Steigerwald, M.L., Choi, H.J., Louie, S.G., Nuckolls, C., Hybertsen, M.S., Neaton, J.B. and Venkataraman, L., 2010. Conductance and geometry of pyridine-linked single-molecule junctions. *Journal of the American Chemical Society*, *132*(19), pp.6817-6821.

[20]   Li, Z. and Franco, I., 2019. Molecular electronics: Toward the atomistic modeling of conductance histograms. *The Journal of Physical Chemistry C*, *123*(15), pp.9693-9701.

[21]   Mejía, L., Renaud, N. and Franco, I., 2018. Signatures of conformational dynamics and electrode-molecule interactions in the conductance profile during pulling of single-molecule junctions. *The Journal of Physical Chemistry Letters*, *9*(4), pp.745-750.

[22] Solomon, G.C., Andrews, D.Q., Van Duyne, R.P. and Ratner, M.A., 2008. When things are not as they seem: Quantum interference turns molecular electron transfer "rules" upside down. *Journal of the American Chemical Society*, *130*(25), pp.7788-7789.

[23] Jiang, F., Trupp, D.I., Algethami, N., Zheng, H., He, W., Alqorashi, A., Zhu, C., Tang, C., Li, R., Liu, J. and Sadeghi, H., 2019. Turning the Tap: Conformational control of quantum interference to modulate single-molecule conductance. *Angewandte Chemie*, *131*(52), pp.19163-19169.

[24] Baer, R. and Neuhauser, D., 2002. Phase coherent electronics: a molecular switch based on quantum interference. *Journal of the American Chemical Society*, *124*(16), pp.4200-4201.

[25] Cardamone, D.M., Stafford, C.A. and Mazumdar, S., 2006. Controlling quantum transport through a single molecule. *Nano letters*, *6*(11), pp.2422-2426.

[26] Guédon, C.M., Valkenier, H., Markussen, T., Thygesen, K.S., Hummelen, J.C. and Van Der Molen, S.J., 2012. Observation of quantum interference in molecular charge transport. *Nature nanotechnology*, *7*(5), pp.305-309.

[27] Liu, J., Huang, X., Wang, F. and Hong, W., 2018. Quantum interference effects in charge transport through single-molecule junctions: detection, manipulation, and application. *Accounts of Chemical Research*, *52*(1), pp.151-160.

[28] Papadopoulos, T.A., Grace, I.M. and Lambert, C.J., 2006. Control of electron transport through Fano resonances in molecular wires. *Physical review b*, *74*(19), p.193306.

[29] Finch, C.M., Garcia-Suarez, V.M. and Lambert, C.J., 2009. Giant thermopower and figure of merit in single-molecule devices. *Physical review b*, *79*(3), p.033405.

[30] Lambert, C.J., Sadeghi, H. and Al-Galiby, Q.H., 2016. Quantum-interference-enhanced thermoelectricity in single molecules and molecular films. *Comptes Rendus Physique*, *17*(10), pp.1084-1095.

[31] Perroni, C.A., Ninno, D. and Cataudella, V., 2016. Thermoelectric efficiency of molecular junctions. *Journal of Physics: Condensed Matter*, *28*(37), p.373001.

Chapter 2

Density Functional Theory (DFT)

2.1. Introduction

Over the past 40 years, the field of molecular electronics has taken advantage of expertise from physics and chemistry to explore and understand the electronic properties of molecules [1]. Hence, many physical theories have been expanded and developed to achieve this goal. One widely used tool in molecular chemistry is called density functional theory (DFT). The implementation of DFT is one of the most successful and unbiased tools used in physics, chemistry and materials science for computing the electronic structure of the ground state of many body systems, in particular atoms, molecules and the condensed phases [2]–[4]. This theory incorporates the Kohn-Sham method of fictitious non-interacting electrons to mimic that of interacting electrons, generating the same density as that of the interacting ones [3], [4].

This chapter is divided into two parts. The first part will introduce the physical theories that underpin the fundamental assertion of DFT, starting from simplifying the Schrödinger equation using the Born-Oppenheimer approximation. This is followed by a discussion of the two theorems; Hohenberg-Kohn and Kohn-Sham [5], which have the significant development to turn DFT to a data processing code (SIESTA) [4] and opened the door to applications for realistic models of bulk materials.

Finally, the second part will discuss the SIESTA code (Spanish Initiative for Electronic Simulations with Thousands of Atoms), which has been used extensively throughout this research work as an efficient theoretical tool to compute the ground state energy and provide

us all the physical properties of large systems having thousands of electrons with reasonable accuracy.

2.2. Many-Body Problem

In quantum statistical mechanics, one of the biggest challenges is solving the Schrödinger equation for many-body problem with large number of interacting particles, which has become a goal for physicists and chemists to achieve. The aim is to obtain the observable properties of such system, which can be accomplished by finding a solution to the Schrödinger equation:

$$\hat{H}\psi\,(r_1, \ldots, r_N, R_1, \ldots, R_M) = E\psi\,(r_1, \ldots, r_N, R_1, \ldots, R_M) \tag{2.1}$$

$\hat{H}$ represents the time-independent Hamiltonian operator, which provides a full description of the electronic structure of a system, ψ is the total eigenstate that has a set of solutions or eigenstates ψ_n, E is the associated energy eigenvalue, r_i and R_I represent the position of the of the $i - th$ electrons and $I - th$ nucleus, respectively. For a system consisting of N-electrons and M-nuclei interacting with each other. The general many body Hamiltonian of such a system is divided into five elements:

$$\hat{H} = \hat{T}_N + \hat{T}_M + \hat{V}_{N-N} + \hat{V}_{M-M} + \hat{V}_{N-M} \tag{2.2}$$

$$\hat{H} = -\overbrace{\sum_{i=1}^{N} \frac{\hbar^2}{2m_i} \nabla_i^2}^{\hat{T}_N} - \overbrace{\sum_{I=1}^{M} \frac{\hbar^2}{2M_I} \nabla_I^2}^{\hat{T}_M} + \overbrace{\frac{1}{2}\sum_{i \neq j}^{N} \frac{e^2}{4\pi\varepsilon_0 |r_i - r_j|}}^{\hat{V}_{N-N}} + \overbrace{\frac{1}{2}\sum_{I \neq J}^{M} \frac{e^2 Z_I Z_J}{4\pi\varepsilon_0 |R_I - R_J|}}^{\hat{V}_{M-M}}$$

$$- \overbrace{\frac{1}{4\pi\varepsilon_0} \sum_{iI=1}^{NM} \frac{Z_I e^2}{|r_i - R_I|}}^{\hat{V}_{N-M}} \tag{2.3}$$

Here, the Hamiltonian operator expresses the sum of the total energy of such system, including both kinetic energies of N-electrons $\hat{T}_N$ and M-nuclei $\hat{T}_M$, and the Coulomb interactions between them ($\hat{V}_{N-N}$, $\hat{V}_{M-M}$, $\hat{V}_{N-M}$). m_i and M_I are the mass of the $i-th$ electron and $I-th$ nuclei, respectively. ε_0 is the dielectric constant of vacuum, Z_I is the atomic number of the $I-th$ nucleus, and e is the electron charge.

As it can be seen from equation (2.3), there are many variables in the Hamiltonian where the interaction terms cannot be directly uncoupled and solved independently for a system with more than a few electrons and nuclei, and that makes the Schrödinger equation impractical or complicated to be solved. In an attempt to tackle this problem, we need to minimize the size of this equation, which can be achieved through the Born-Oppenheimer approximation [6].

2.3. Born-Oppenheimer approximation

A simple system such as two hydrogen atoms, where each atom has one electron, can be solved analytically, and the solution to the Schrödinger equation will be an exact. However, for a large system consists of more than a few electrons and nuclei finding the eigenvalues and eigenstates of the Schrödinger equation becomes more difficult. Therefore, the traditional Born-Oppenheimer approximation can solve this issue by separating the nucleon and electron degrees of freedom and reducing the size of that equation.

This approximation is based on the fact that the mass of the nuclei is approximately three orders of magnitude larger than the mass of electrons [6]–[8]. The heavier the nuclei are, the slower they will move compared to electrons, which thus can be treated as almost stationary sources. In other words, their kinetic and potential energy ($\hat{T}_M$, $\hat{V}_M$) can be negligible. This reduces the problem to electrons only, and thus equation (2.3) can be written as:

$$\hat{H}_e = -\sum_{i=1}^{N} \frac{\hbar^2}{2m_i}\nabla_i^2 + \frac{1}{2}\sum_{i \neq j}^{N} \frac{e^2}{4\pi\varepsilon_0 |r_i - r_j|} - \frac{1}{4\pi\varepsilon_0}\sum_{iI=1}^{NM} \frac{Z_I e^2}{|r_i - R_I|} \qquad (2.4)$$

This simplification by Born-Oppenheimer approximation was the first attempt to reach the aim. However, further steps are required to solve the Schrödinger equation. Therefore, Hohenberg and Kohn came up with a method to construct density functional theory (DFT) that determines all the electronic properties by the ground state density $\rho_0(r)$ [9], [10].

2.4. The Hohenberg-Kohn Theorems

The Hohenberg-Kohn (HK) theorems, a bedrock of modern density functional theory (DFT), play a fundamental role in the development of DFT. The formulation applies for any system consisting of electrons moving under the influence of an external potential $V_{ext}(r_i)$.

The Hohenberg-Kohn theorems include two simply stated assertions:

• **Theorem 1**. If there are two different external potentials $(V_{ext}^{~1})$ and $(V_{ext}^{~2})$ arising from the same density $\rho(\vec{r})$, then there will be two Hamiltonians H_1 and H_2 with the same ground state density, but different wavefunctions ψ_1 and ψ_2. From the variational principle, these two wavefunctions cannot be equal to each other, because they satisfy different Schrödinger equations, hence they have different Hamiltonians and different ground state energies, meaning that the ground state electronic density of a system is uniquely determined by only one specific external potential [10]–[12].

• **Theorem 2**. Consider the expression for the total energy E of a system with density ρ:

$$E_{total}(\rho) = \underbrace{T_{int}(\rho) + V_e(\rho)}_{F_{H-K}(\rho)} + \int dr\, V_{ext}(r)\rho(\vec{r}) \qquad (2.5)$$

18

The kinetic energy term T_{int} for interacting systems and the internal interaction of the electrons V_e are treated as the same for the whole system. Therefore, they are called a universal functional $F_{H-K}(\rho)$, depending only on the density $\rho(\vec{r})$. Consequently, if this universal functional is known, then by minimizing the energy (Eq. 2.5), we can obtain the ground-state of the system, and all physical quantities of interest could be calculated [10]–[12].

Although the Hohenberg-Kohn theorems are extremely powerful, they do not offer a way of computing the ground-state density of a system in practice, because the exact form of the functional $F_{H-K}(\rho)$ is not known. The kinetic term and internal energies of the interacting electrons cannot generally be expressed as functional of the density (i.e., the direct minimization will not provide us the ground state energy, but by the simpler procedure of Kohn-Sham).

2.5. Kohn-Sham theorem

Even though the wave function of non-interacting particles is dissimilar from that of the interacting ones and so is the density, the Kohn–Sham approach is based on the approach that a fictitious system of the non-interacting particles yields, in such a way, the same density as that of the interacting particles (a self-consistent method) [2], [5].

The idea of this formalism is to replace the original Hamiltonian of an interacting system with an effective Hamiltonian (H_{eff}) of a non-interacting system in an effective external potential $V_{eff}(r_i)$, which has the same ground-state density as the initial interacting system [13], [14]. Since there is no clear procedure for calculating this, the Kohn-Sham method is considered as an ansatz, but it is considerably easier to solve than the interacting problem. The Kohn-Sham method is based on the Hohenberg-Kohn universal functional:

$$F_{H-K}[\rho(\vec{r})] = T_{int}[\rho(\vec{r})] + \underbrace{V_e[\rho(\vec{r})]}_{\substack{zero\ for \\ non-interacting \\ system}} \tag{2.6}$$

The Hohenberg-Kohn functional for non-interacting electrons has only the kinetic energy, and the internal interaction of the electrons V_e is equal to zero. The energy functional of the Kohn-Sham functional $F_{KS}[\rho(\vec{r})]$, in contrast to (Eq. 2.5), is given by:

$$F_{KS}[\rho(\vec{r})] = T_{non}[\rho(\vec{r})] + E_{Hart}[n\rho(\vec{r})] + \int V_{ext}(\vec{r})\rho(\vec{r})\,d\vec{r} + E_{xc}[\rho(\vec{r})] \tag{2.7}$$

where T_{non} is the kinetic energy of the non-interacting system, which is different from T_{int} (for interaction system) in equation (2.5), E_{Hart} is called the Hartree energy, and that is the classical electrostatic energy or classical self-interaction energy of the electron gas associated with density $\rho(\vec{r})$. The last term (E_{xc}) is called the exchange-correlation energy functional, which is defined as the difference between the kinetic energy for the interacting, non-interacting systems and the electron-electron interaction energy, as shown in equation (2.8).

$$E_{xc}[\rho(\vec{r})] = F_{H-K}[\rho(\vec{r})] - \overbrace{\frac{1}{2}\int \frac{\rho(\vec{r}_1)\rho(\vec{r}_2)}{|\vec{r}_1-\vec{r}_2|}\,d\vec{r}_1 d\vec{r}_2}^{E_{Hart}[\rho(\vec{r})]} - T_{non}[\rho(\vec{r})] \tag{2.8}$$

Since E_{xc} does not have an exact form, enormous efforts have been directed toward finding a better approximation. Currently, the functionals can investigate and predict the physical properties of a wide range of solid-state systems and molecules. For the last three terms in equation (2.7), the functional derivatives are taken to construct the effective single particle potential, $V_{eff}(\vec{r})$:

$$V_{eff}(\vec{r}) = V_{ext}(\vec{r}) + \underbrace{\frac{\partial E_{Hart}[\rho(\vec{r})]}{\partial \rho(\vec{r})}}_{V_H} + \underbrace{\frac{\partial E_{xc}[\rho(\vec{r})]}{\partial \rho(\vec{r})}}_{V_{xc}} \tag{2.9}$$

where, V_H is the Hartree potential of the electrons, and V_{xc} is the exchange-correlation potential. Then, this potential can be used to calculate the Hamiltonian of the single particle:

$$H_{KS} = T_{non} + V_{eff} \qquad (2.10)$$

By utilizing this Hamiltonian, the Schrödinger equation becomes:

$$[T_{non} + V_{eff}]\psi_i(r) = \varepsilon_i \psi_i(r) \qquad (2.11)$$

This is known as Kohn-Sham equation, where ψ_i is the wave function of electronic state i, and ε_i is the Kohn-Sham eigenvalue. The Kohn-Sham approach shows that a complicated interacting many-body system can be mapped onto a set of simple non-interacting equations exactly if the exchange-correlation functional is known. However, this functional is not known exactly, so approximations must be made.

2.5.1. Exchange and correlation

If the exchange correlation functional (E_{xc}) is known precisely, the Kohn-Sham method could be a powerful approach to obtain an accurate ground-state density. However, as there is no exact form to evaluate (E_{xc}), this leads to the construction of approximation methods. As a result, the local density approximation (LDA) and the generalized gradient approximation (GGA) have become the most commonly used in many body problems [15].

The LDA, that has long been the standard choice [16], is the simplest approximation, in which the exchange correlation functional (E_{xc}) is based only on the local density. This approximation is an accurate and powerful functional for systems where the electron density is not rapidly changing. Moreover, the total correlation energy is overestimated in LDA, and the total exchange energy is underestimated, which cause errors in some systems, for example, semiconductors and insulators [17]. Therefore, it is essential to obtain an alternative approximation such as the generalized gradient approximation (GGA). The GGA to some

extent is LDA but involves the density with its gradient (the derivative of the density). As a result of that, it is more accurate approximation compared to LDA functional. To give more information about these two approximations, the following sections will briefly describe them.

2.5.1.1. Local Density Approximation (LDA)

As mentioned previously, the LDA approximation tends to underestimate distances and angles of optimized molecular geometries, and it only works accurately for systems where the electron density is varying slowly. Its functional (E_{xc}^{LDA}) is given by the expression [5]:

$$E_{xc}^{LDA}[\rho(\vec{r})] = \int \rho(\vec{r}) E_{xc}^{HGE}[\rho(\vec{r})] \, d(\vec{r}) \tag{2.12}$$

The term E_{xc}^{HGE} is known as the exchange-correlation energy of the homogeneous electron gas with density of $\rho(\vec{r})$. This term can be split into two parts; the sum of the exchange $E_x^{HGE}[\rho(\vec{r})]$, and the correlation energies $E_c^{HGE}[\rho(\vec{r})]$, which can be evaluated as:

$$E_{xc}^{LDA} = \int d(\vec{r}) \rho(\vec{r}) E_x^{HGE}[\rho(\vec{r})] + E_c^{HGE}[\rho(\vec{r})] \tag{2.13}$$

This type of functional performs well in the homogeneous systems with S and P orbitals like graphene and carbon nanotubes, while for atoms that have d and f type orbitals, a large error is predicted.

2.5.1.2. Generalized Gradient Approximation (GGA)

Since the LDA approximation fails in situations where the density is changing rapidly, the LDA has been expanded by involving the derivatives of the density into the functional form of the

exchange and correlation energies. To perform this is by including the gradient and the higher spatial derivatives of the total charge density into the approximation.

I.e., $(|\nabla \rho(\vec{r})|, |\nabla^2 \rho(\vec{r})|, \dots)$

$$E_{xc}^{GGA}[\rho(\vec{r})] = \int \rho(\vec{r})\varepsilon_{xc}^{GGA}[\rho(\vec{r}), |\nabla \rho(\vec{r})|]d(\vec{r}) \qquad (2.14)$$

This function E_{xc}^{GGA} is known as the generalised gradient approximation (GGA). This type of functional performs well in the non-homogeneous systems, and it tends to overestimate distances and angles of the optimized molecular geometries.

2.6. SIESTA

SIESTA is an acronym derived from the Spanish Initiative for Electronic Simulations with Thousands of Atoms. It is a well-known implementation of the DFT method to solve the Kohn-Sham equations, which is suitable for studying crystals and metallic electrodes and investigating their electronic properties [4]. Thus, to solve the Kohn-Sham equations, SIESTA uses various approximation schemes which are discussed in the following section.

2.6.1. The Pseudopotential Approximation

Investigating the electronic properties of typical systems of molecules consist of many atoms requires large computer time and memory. Therefore, using the pseudopotential approximation is useful to save time and memory in a simulation.

The pseudopotential approximation was proposed by Fermi in 1934 [18]. The principle of this approximation is based on replacing the core electrons, which occupy the filled shells of the

atomic orbitals, and leaving the valance electrons that are arranged in the partially filled outer shells. The reason for that is because the core electrons are not involved in the interaction between atoms compared to the valance ones, which are responsible in forming molecular orbitals via atomic interaction. In other words, core electrons are spatially localized about the nucleus, and valance electron states overlap when atoms are brought together, which means that the latter plays an essential role in determining most of the chemical properties. As a result of that, the significant decrease in the electrons number of a large system would lower the computational expenses for that system.

2.6.2. Calculating the Binding Energy (B.E)

The binding energy between different parts of configurations can be computed using the DFT method. This is achieved by calculating the ground state energy of the whole system (E_{AB}^{AB}) and then the energy of the individual components $(E_A^A)(E_B^B)$. However, this method is subject to errors when using a DFT code such as SIESTA, which uses localised basis sets that are focused on the nuclei. The basis-functions of interacted atoms will overlap when they become close together, causing artificial strengthening of atomic interactions, and this could affect the total energy of the system and give inaccurate calculation. To solve this type of error, the Basis Set Superposition Error correction (BSSE) method [19] or the counterpoise correction (CP) method [20] is instead used.

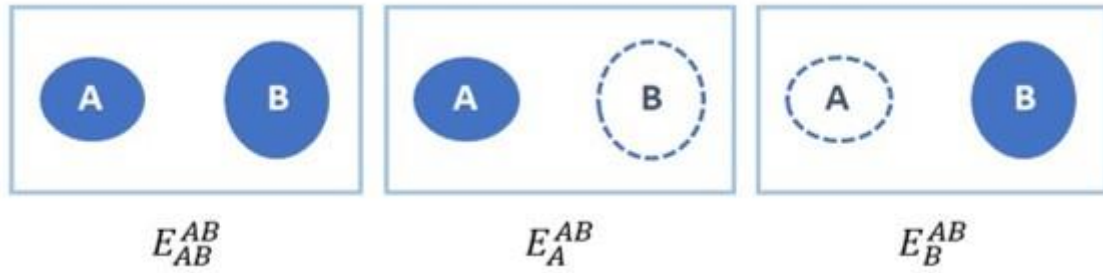Consider two systems, which are labelled as *A* and *B* as shown in the figure below.

Figure (2.1): Counterpoise method to calculate the binding energy, where A and B symbolize to the molecule and the lead, respectively.

The general definition of the binding energy of the interaction is given by:

$$B.E = \Delta E(AB) = E_{AB}^{AB} - (E_A^A + E_B^B)$$

In contrast, the definition of the binding energy using the counterpoise correction method is:

$$B.E = \Delta E(AB) = E_{AB}^{AB} - (E_A^{AB} + E_B^{AB})$$

where $E_{AB}^{AB} \Longrightarrow$ represents the total energy of the dimer systems A and B.

$E_A^{AB} \Longrightarrow$ represents the total energy of system A evaluated in the basis of the dimer.

while $E_B^{AB} \Longrightarrow$ represents the total energy of system B evaluated in the basis of the dimer.

This means that 'ghost' states (basis set functions which have no electrons or protons) are used to evaluate the total energy of the system A or B in the dimer basis. This method provides reliable and realistic results for the binding energy compared to the general definition [21], [22].

2.7. Calculations in Practice

There are several parameters which need to be determined within the SIESTA code to perform calculations. First, constructing the atomic configuration of the desired system, and then determining for each component the appropriate pseudopotentials, which can be distinct for each exchange-correlation functional. Secondly, the accuracy and speed of calculations are restricted to some parameters such as the type of the basis set, thus, it is important to choose a suitable basis set for each element. Furthermore, the grid fineness and density convergence tolerances parameter provide more precise calculations. Finally, the Pulay is another input parameter to control the convergence. It accelerates or maintains the stability of the convergence of the charge density in SIESTA.

After choosing the suitable parameters, the next step is finding the charge density for non-interacting system by using the self-consistency process within SIESTA. According to figure (2.2), the calculation starts with constructing an initial charge density as a guess to compute the effective potential, which is the sum of the external potential, Hartree potential and exchange-correlation potential. After that, a new charge density is obtained by solving the Kohn-Sham equation, and the next iteration is started and repeated many times till the necessary convergence criteria is reached, so the ground-state electron density is obtained, and from that all properties including Hamiltonian, force, energy and wave function, of the ground state are determined. For the geometric optimization, this process is performed in a loop, which is controlled via conjugate gradient method (CG) [23], [24] to obtain the minimum ground state energy and the corresponding atomic structure. Generating the Hamiltonian of a given system is the key ingredient for the quantum transport calculations in the next chapter.
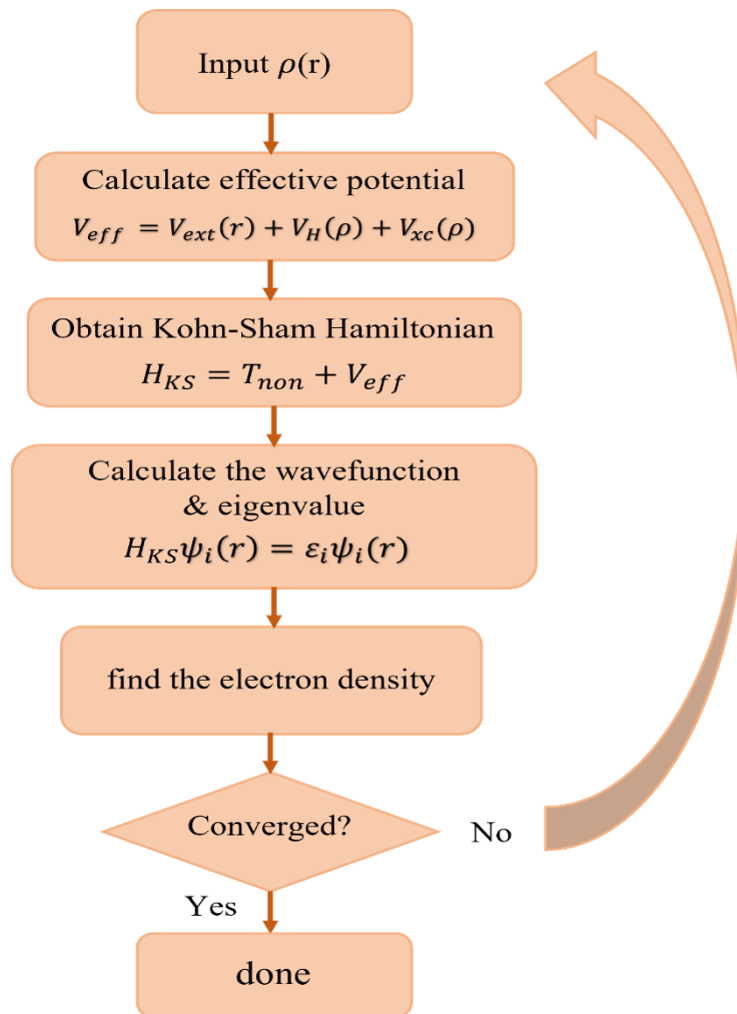
Figure (2.2): Schematic of the self-consistency process within SIESTA.

Bibliography

[1] Su, T.A., Neupane, M., Steigerwald, M.L., Venkataraman, L. and Nuckolls, C., 2016. Chemical principles of single-molecule electronics. *Nature Reviews Materials*, *1*(3), pp.1-15.

[2] Parr, R.G., 1980. Density functional theory of atoms and molecules. In *Horizons of quantum chemistry*. Springer, Dordrecht. pp.5-15.

[3] Argaman, N. and Makov, G., 2000. Density functional theory: An introduction. *American Journal of Physics*, *68*(1), pp.69-79.

[4] Soler, J.M., Artacho, E., Gale, J.D., García, A., Junquera, J., Ordejón, P. and Sánchez-Portal, D., 2002. The SIESTA method for ab initio order-N materials simulation. *Journal of Physics: Condensed Matter*, *14*(11), pp.2745-2779.

[5] Kohn, W. and Sham, L.J., 1965. Self-consistent equations including exchange and correlation effects. *Physical review*, *140*(4A), p.A1133.

[6] Sutcliffe, B.T. and Woolley, R.G., 2012. On the quantum theory of molecules. *The Journal of chemical physics*, *137*(22), p.22A544.

[7] Burke, K., 2007. The abc of dft. *Department of Chemistry, University of California*, *40*.

[8] Ismael, A., 2017. *Towards molecular-scale sensing and thermoelectric energy harvesting* (Doctoral dissertation, Lancaster University).

[9] Sahni, V., 2004. The Hohenberg-Kohn Theorems and Kohn-Sham Density Functional Theory. In *Quantal Density Functional Theory*. Springer, Berlin, Heidelberg. pp.99-123.

[10] Kohn, W., 1999. Nobel Lecture: Electronic structure of matter—wave functions and density functionals. *Reviews of Modern Physics*, *71*(5), p.1253.

[11] Martin, R.M., 2020. *Electronic structure: basic theory and practical methods*. Cambridge university press.

[12] Kohn, W., Becke, A.D. and Parr, R.G., 1996. Density functional theory of electronic structure. *The Journal of Physical Chemistry*, *100*(31), pp.12974-12980.

[13]   Levy, M., 1982. Electron densities in search of Hamiltonians. *Physical Review A*, *26*(3), p.1200.

[14]   Lieb, E. H., 1997. Thomas-Fermi and related theories of atoms and molecules. In *The Stability of Matter: From Atoms to Stars* (pp. 259-297). Springer, Berlin, Heidelberg.

[15]   Perdew, J.P., Burke, K. and Ernzerhof, M., 1996. Generalized gradient approximation made simple. *Physical review letters*, *77*(18), p.3865.

[16]   Jones, R.O. and Gunnarsson, O., 1989. The density functional formalism, its applications and prospects. *Reviews of Modern Physics*, *61*(3), p.689.

[17]   Zupan, A., Blaha, P., Schwarz, K. and Perdew, J.P., 1998. Pressure-induced phase transitions in solid Si, SiO 2, and Fe: Performance of local-spin-density and generalized-gradient-approximation density functionals. *Physical Review B*, *58*(17), p.11266.

[18]   Fermi, E., 1936. Motion of neutrons in hydrogenous substances. *Ricerca Scientifica*, *7*(2), pp.13-52.

[19]   Jansen, H.B. and Ros, P., 1969. Non-empirical molecular orbital calculations on the protonation of carbon monoxide. *Chemical Physics Letters*, *3*(3), pp.140-143.

[20]   Boys, S.F. and Bernardi, F.J.M.P., 1970. The calculation of small molecular interactions by the differences of separate total energies. Some procedures with reduced errors. *Molecular Physics*, *19*(4), pp.553-566.

[21]   Haynes, P.D., Skylaris, C.K., Mostofi, A.A. and Payne, M.C., 2006. Elimination of basis set superposition error in linear-scaling density-functional calculations with local orbitals optimised in situ. *Chemical physics letters*, *422*(4-6), pp.345-349.

[22]   Boese, A.D., Jansen, G., Torheyden, M., Höfener, S. and Klopper, W., 2011. Effects of counterpoise correction and basis set extrapolation on the MP2 geometries of hydrogen bonded dimers of ammonia, water, and hydrogen fluoride. *Physical Chemistry Chemical Physics*, *13*(3), pp.1230-1238.

[23]   Press, W.H., Teukolsky, S.A., Vetterling, W.T. and Flannery, B.P., 2007. *Numerical recipes 3rd edition: The art of scientific computing*. Cambridge university press.

[24]   Payne, M.C., Teter, M.P., Allan, D.C., Arias, T.A. and Joannopoulos, A.J., 1992. Iterative minimization techniques for ab initio total-energy calculations: molecular dynamics and conjugate gradients. *Reviews of modern physics*, *64*(4), p.1045.

Chapter 3

Quantum Transport Theory

3.1. Introduction

In molecular electronics, the theoretical study of a single-molecule junction can be treated as a scattering problem, which consists of three components; the leads (electrodes), the anchor group (part of the molecule which binds to the electrodes) and the molecule (scattering region). Since a molecule is connected between the electrodes, charge will travel from one side to the other. Thus, for designing more efficient materials, the goal is to understand the scattering process in the electrode junction and molecular bridge and investigate its electrical properties [1], such as, the transmission coefficient $T(E)$, the thermopower (or Seebeck coefficient S) and figure of merit ZT. The transmission coefficient $T(E)$, a key quantity of interest, is a property of the whole system, which includes information about the electrodes, the molecule and the linkers between them.

In this chapter, first, the scattering matrix will be introduced and followed by the discussion regarding the Landauer formula, which provides a link between the conductance and the transmission function. Then, illustrating the general method for computing the transmission coefficient $T(E)$ in a 1-dimensional system through solving the Schrödinger equation, and for describing the transmission curve of a system I will examine the Breit-Wigner formula. Finally, this chapter will discuss the equilibrium Green's function approach, which is an efficient method for solving scattering problems and calculating the transmission without explicitly solving the Schrödinger equation.
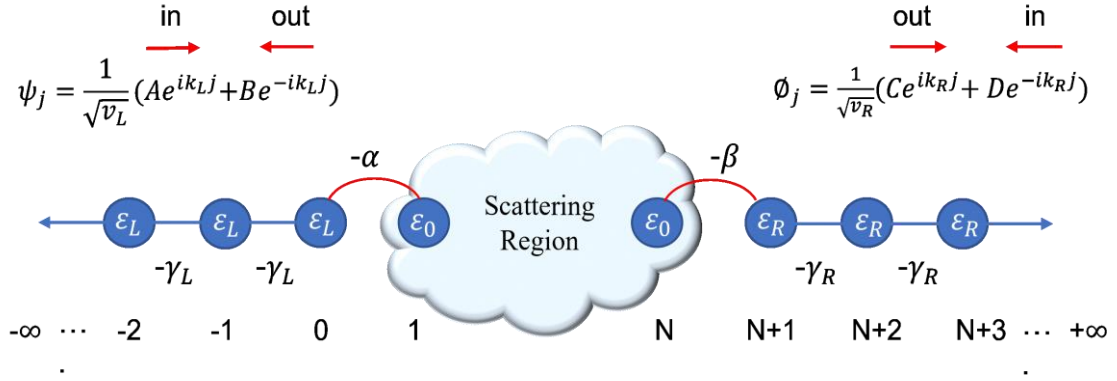
3.2. Scattering matrix

Figure (3.1): A 1-dimensional system which has a scattering region of N atoms connected by the hopping elements $-\alpha$ and $-\beta$ to left and right semi-infinite linear leads of site energyies ε_L and ε_R with couplings $-\gamma_L$ and $-\gamma_R$, respectively.

The scattering-matrix is an effective tool to calculate the transport properties in scattering theory, and its calculation can be achieved via solving the time-independent Schrödinger equation.

First, the most general solution to the Schrödinger equation in the left lead is:

$$\psi_j = \frac{A}{\sqrt{v_l}} e^{ik_l j} + \frac{B}{\sqrt{v_l}} e^{-ik_l j} \tag{3.1}$$

The constants A and B refer to the amplitudes of two waves travelling to the right and left, respectively, here v_l is the group velocity of the plane waves on the left.

The current in the left lead is:

$$I_{left} = |A^2| - |B^2| \tag{3.2}$$

Secondly, from the most general wave function in the right lead is:

$$\emptyset_j = \frac{C}{\sqrt{v_r}} e^{ik_r j} + \frac{D}{\sqrt{v_r}} e^{-ik_r j} \qquad (3.3)$$

$$I_{right} = |C^2| - |D^2| \qquad (3.4)$$

Here, C and D represent the amplitudes of two waves travelling to the right and left, respectively.

Since the current satisfies the relation $(I_{left} = I_{right})$, hence:

$$|A^2| - |B^2| = |C^2| - |D^2| \qquad (3.5)$$

$$|A^2| + |D^2| = |B^2| + |C^2| \qquad (3.6)$$

This expression states that the incoming current is equal to the outgoing current. The left term $(|A^2| + |D^2|)$ refers to the incoming current from both electrodes, and the right term $(|B^2| + |C^2|)$ indicates the outgoing current into both electrodes.

Relating outgoing amplitudes to incoming amplitudes requires constructing the scattering matrix, which is often called the 's-matrix':

$$\underbrace{\begin{bmatrix} B \\ C \end{bmatrix}}_{|out\rangle} = \underbrace{\begin{bmatrix} S_{11} & S_{12} \\ S_{21} & S_{22} \end{bmatrix}}_{S} \underbrace{\begin{bmatrix} A \\ D \end{bmatrix}}_{|in\rangle} \qquad (3.7)$$

$$B = S_{11}A + S_{12}D \qquad (3.8)$$

$$C = S_{21}A + S_{22}D \qquad (3.9)$$

Consider the case where a unit current plane wave arrives only from the left, so that $A = 1$ and $D = 0$, then $B = r$ and $C = t$, where r is the amplitude of the reflected wave on the left, and t is the amplitude of the transmitted wave on the right. With this choice of A and D, this yields:

$$\begin{bmatrix} B \\ C \end{bmatrix} = \begin{bmatrix} S_{11} \\ S_{21} \end{bmatrix} = \begin{bmatrix} r \\ t \end{bmatrix} \tag{3.10}$$

The physical meaning of S_{11} is the reflection amplitude (r) as a result of a wave coming in from the left, and S_{21} is the transmission amplitude (t).

Now, consider the case where a unit current plane wave comes only from the right, so that $D = 1$ and $A = 0$, then $B = t'$ and $C = r'$.

$$\begin{bmatrix} B \\ C \end{bmatrix} = \begin{bmatrix} S_{12} \\ S_{22} \end{bmatrix} = \begin{bmatrix} t' \\ r' \end{bmatrix} \tag{3.11}$$

Hence $S_{12} = t'$ and $S_{22} = r'$

This shows that the physical meaning of the s-matrix elements are as follows:

$$S = \begin{pmatrix} S_{11} & S_{12} \\ S_{21} & S_{22} \end{pmatrix} = \begin{pmatrix} r & t' \\ t & r' \end{pmatrix} \tag{3.12}$$

Taking the Hermitian conjugate of the scattering matrix equation (3.7) results in:

$$(A^* \quad D^*)S^\dagger S \begin{pmatrix} A \\ D \end{pmatrix} = (B^* \quad C^*)\begin{pmatrix} B \\ C \end{pmatrix} \tag{3.13}$$

Where $S^\dagger S$ is the unitary matrix [2], so that $S^\dagger S = I$

$$\begin{pmatrix} r^* & t^* \\ t^* & r^* \end{pmatrix}\begin{pmatrix} r & t' \\ t & r' \end{pmatrix} = \begin{pmatrix} 1 & 0 \\ 0 & 1 \end{pmatrix} \tag{3.14}$$

In terms of scattering theory:

$$|r^2| + |t^2| = 1 \implies R + T = 1 \tag{3.15}$$

$$|r'^2| + |t'^2| = 1 \implies R' + T' = 1 \tag{3.16}$$

where the transmission and reflection denoted by $T = |t|^2$ and $R = |r|^2$.

Knowledge of the scattering matrix opens the door to predict the electrical conductance of a scatterer joined to semi-infinite electrodes via the Landauer formula.

3.3. The Landauer Formula

Figure (3.2): A mesoscopic quantum mechanical scatterer in contact with macroscopic electrodes from both sides, where these electrodes are linked to left and right reservoirs with chemical potentials μ_L and μ_R. By applying a small voltage, $e\delta V = (\mu_L - \mu_R)$, some of the incident wave packet (I) which hits the scatterer from the left will be reflected (r) and others will be transmitted to the right side (t).

The Landauer formula [3]–[6] is a standard theoretical model to describe the transport phenomena within ballistic mesoscopic systems. It is an expression for the electric conductance [7], [8], and it can be used if the scattering is only elastic, where the energy of the electron passing through the molecule does not change. To derive this formula, consider a 1-dimensional system consisting of a scattering region attached from both sides to two electrodes, which are considered to be ballistic conductors, meaning they have no scattering, hence the transmission probability is one. These electrodes are connected to external reservoirs, which feed electrons of energy E into the system (Fig. 3.2). When the chemical potentials of both

reservoirs are identical, then the current $I = 0$, thus they should be differed slightly by applying small voltage, $\mu_L > \mu_R \Rightarrow (\mu_L - \mu_R) = \delta E > 0$, to allow the flow of electrons from the left to the right side via the scattering region (the molecule).

To compute the current in such a system, the first step is to analyse the incident electric current (δI) that provided by the chemical potential difference.

$$\delta I = ev_g \frac{\partial n}{\partial E} \delta E = ev_g \frac{\partial n}{\partial E} (\mu_L - \mu_R) \tag{3.17}$$

where, the electron charge and the group velocity represented by (e and v_g), respectively. ($\partial n / \partial E$) is the density of state, which is the number of states (∂n) per unit energy (∂E) and can be expressed by using the chain rule for differentiation as:

$$\frac{\partial n}{\partial E} = \left(\frac{\partial n}{\partial k}\frac{\partial k}{\partial E}\right) = \frac{\partial n}{\partial k}\frac{1}{v_g \hbar} \tag{3.18}$$

where $\frac{\partial n}{\partial k} = \frac{1}{\pi}$, the group velocity $v_g = \frac{1}{\hbar}\frac{dE}{dK}$, and $\hbar = \frac{h}{2\pi}$. This simplifies equation (3.18) to:

$$\frac{\partial n}{\partial E} = \frac{2}{v_g h} \tag{3.19}$$

$$\delta I = \frac{2e}{h}(\mu_L - \mu_R) = \frac{2e^2}{h}\delta V \tag{3.20}$$

where $(\mu_L - \mu_R) = e\delta V$ is the voltage in the reservoirs produced by the difference in the potentials, and h is Planck's constant.

From (3.20) we can consider two situations: Firstly, if the system has no scattering region, the conductance would be:

$$G = \frac{\delta I}{\delta V} = \frac{2e^2}{h} \tag{3.21}$$

For an open channel, this corresponds to the conductance of a quantum wire G_0, where:

36

$$G_0 = \frac{2e^2}{h} \approx 77.48 \, \mu s$$

Secondly, in the presence of the scattering region, if there is a unit incident current from the left electrode (i.e., $A = 1, D = 0$ in equation (3.7)), the current in the right electrode is given by:

$$\delta I = \frac{2e^2}{h} T(E) \, \delta V \tag{3.22}$$

Consequently, the electrical conductance in this case can be written as:

$$G = \frac{\delta I}{\delta V} = \frac{2e^2}{h} T(E) \tag{3.23}$$

$$G = G_0 T(E) \tag{3.24}$$

This equation (3.24) is known as the Landauer formula for a 1-dimensional system in the limit of zero voltage and zero temperature, where $T(E)$ is the transmission coefficient (electron transmission probability) through the molecule [9].

At finite temperature and zero voltage the electrical conductance can be written as:

$$G = \frac{I}{V} = G_0 \int_{-\infty}^{+\infty} dE \, T(E) \left(-\frac{df(E)}{dE} \right) \tag{2.25}$$

As $-\frac{df(E)}{dE}$ represents a normalised probability distribution with a width of the order $k_B T$, the above integral refers to a thermal average of $T(E)$ over an energy range of order $k_B T$, where k_B is Boltzmann constant, and T is absolute temperature.

At finite voltage and finite temperature, the current passing from left to right lead is defined as:

$$I = \frac{2e}{h} \int_{-\infty}^{+\infty} dE \, T(E)[f_L(E) - f_R(E)] \tag{2.26}$$

$f(E)$ is the Fermi-Dirac probability distribution function of left and right electrodes:

$$f_L(E) = \frac{1}{1 + e^{(E - \mu_L / k_B T)}} \quad , \quad f_R(E) = \frac{1}{1 + e^{(E - \mu_R / k_B T)}} \tag{3.27}$$

If $f_L(E) = f_R(E)$, then the chemical potentials of left and right reservoirs are equal ($\mu_L = \mu_R$), and thus the current passing through the system is equal to zero.

At zero temperature and finite voltage (applied voltage) where $\mu_L = E_F + \frac{ev_b}{2}$ and $\mu_R = E_F + \frac{ev_b}{2}$, this yields the current:

$$I = \frac{2e}{h} \int\limits_{E_F - \frac{ev_b}{2}}^{E_F + \frac{ev_b}{2}} dE \, T(E) \tag{3.28}$$

The transmission coefficient $T(E)$ is a property of the whole system, which includes the leads, the molecule and the contact between the leads and the molecule. Following section will illustrate the mathematical process to derive this important quantity.

3.4. A general scatterer connected to semi-infinite leads

The structure below shows a combination of a scattering region containing N atoms with site energy ε_0 labelled $j = 1, 2, \dots N$, where this scatterer linked to left and right electrodes by couplings $-\alpha$ and $-\beta$, respectively.
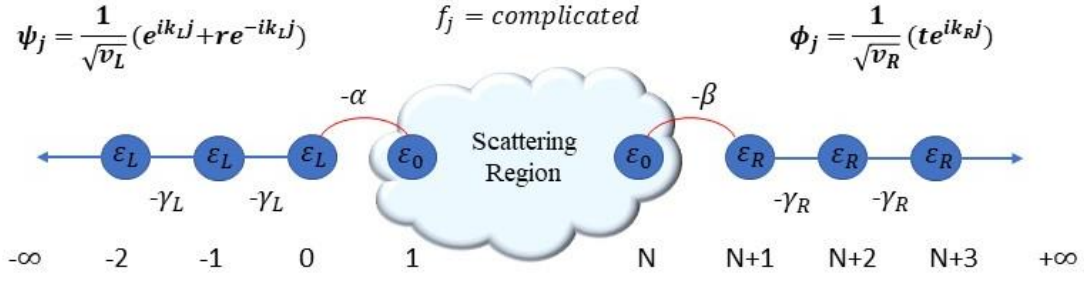
Figure (3.3): A scattering region of N sites in contact by the hopping elements $-\alpha$ and $-\beta$ to left and right semi-infinite linear leads of site energyies ε_L and ε_R with couplings $-\gamma_L$ and $-\gamma_R$. The wave function ψ_j is chosen to corresponds to a unit incident current from the left.

The aim is to solve the time-independent Schrödinger equation of such a system.

$$H|\psi\rangle = E|\psi\rangle$$

Or, in another form

$$\sum_{l=-\infty}^{\infty} H_{jl}\,\psi_l = E\psi_j \tag{3.29}$$

The solution to the left and right electrodes will be denoted by ψ_j and ϕ_j, respectively. However, f_j refers to the solution of the scattering region.

With these symbols, the Schrödinger equations for the system are written as:

$$\varepsilon_L\psi_j - \gamma_L\psi_{j-1} - \gamma_L\psi_{j+1} = E\psi_j \qquad \text{for } j = -1, -2, \dots -\infty \tag{3.30}$$

$$\varepsilon_L\psi_0 - \gamma_L\psi_{-1} - \alpha f_1 = E\psi_0 \qquad \text{for } j = 0 \tag{3.31}$$

$$\sum_{l=1}^{N} H_{jl}\, f_l = E f_j \qquad \text{for } j = 2, \dots .. N \tag{3.33}$$

$$\sum_{l=1}^{N} H_{Nl}\, f_l - \beta\phi_{N+1} = E f_N \qquad \text{for } j = N \tag{3.34}$$

$$\varepsilon_R\phi_{N+1} - \beta f_N - \gamma_R\phi_{N+2} = E\phi_{N+1} \qquad \text{for } j = N+1 \tag{3.35}$$

$$\varepsilon_R\phi_j - \gamma_R\phi_{j-1} - \gamma_R\phi_{j+1} = E\phi_j \qquad \text{for } j = N+2, N+3, \dots \infty \tag{3.36}$$

To the left of the scattering region, the general solution is:

$$\psi_j = \frac{1}{\sqrt{v_L}}\left\{e^{ik_L\,j} + re^{-ik_L\,j}\right\} \tag{3.37}$$

However, the general solution to the right of the scattering region is:

$$\phi_j = \frac{1}{\sqrt{v_R}}\left\{te^{ik_R\,j}\right\} \tag{3.38}$$

where r and t are the reflection and transmission amplitudes. The v_L and v_R are the group velocity of the left and right leads, respectively.

Substituting (3.37) into (3.30), and (3.37) into (3.31) yields:

$$E = \varepsilon_L - 2\gamma_L \cos k_L \tag{3.39}$$

$$\gamma_L\psi_1 = \alpha f_1 \tag{3.40}$$

Similarly, substituting (3.36) into (3.33) and (3.34) results in:

$$E = \varepsilon_R - 2\gamma_R \cos k_R \tag{3.41}$$

$$\gamma_R\phi_N = \beta f_N \tag{3.42}$$

It can be seen from equations (3.39) and (3.41) that the wave vector k in the left lead is unequal to that in the right lead (i.e., non-symmetric junction). Furthermore, equations (3.40) and (3.42) describe that the wave function on the inside of the scatterer (i.e., f_1 and f_N) is related to the wave function on the outside (i.e., ψ_1 and ϕ_N).

Note that equations (3.32) and (3.34) can be written in a matrix form as:

$$\begin{bmatrix} f_1 \\ \vdots \\ f_j \\ \vdots \\ f_N \end{bmatrix} = \begin{bmatrix} G_{11} & G_{12} & .. & .. & G_{1N} \\ G_{21} & G_{22} & .. & .. & G_{2N} \\ \vdots & & & & \vdots \\ \vdots & & & & \vdots \\ G_{N1} & G_{N2} & .. & .. & G_{NN} \end{bmatrix} \begin{bmatrix} -\alpha\psi_0 \\ 0 \\ \vdots \\ 0 \\ -\beta\phi_{N+1} \end{bmatrix}$$

40

By selecting the top and bottom rows of the matrix above, this yields:

$$\begin{bmatrix} f_1 \\ f_N \end{bmatrix} = \begin{bmatrix} G_{11} & G_{1N} \\ G_{N1} & G_{NN} \end{bmatrix} \begin{bmatrix} -\alpha\psi_0 \\ -\beta\phi_{N+1} \end{bmatrix} \tag{3.43}$$

$G_{11}, G_{1N}, G_{N1}, G_{NN}$ are the elements of the sub-matrix of the green's function of the isolated region G_{ij}. Solving equation (3.43) will results in the transmission coefficient equation [3]:

$$T(E) = 4 \left[\frac{\alpha^2 \sin k_L}{\gamma_L} \right] \left[\frac{\beta^2 \sin k_R}{\gamma_R} \right] \left| \frac{G_{N1}}{\Delta} \right|^2 = 4\Gamma_L\Gamma_R \left| \frac{G_{N1}}{\Delta} \right|^2 \tag{3.44}$$

- $\left[\frac{\alpha^2 \sin k_L}{\gamma_L} \right] = \Gamma_L$ is a property of the left lead.

- $\left[\frac{\beta^2 \sin k_R}{\gamma_R} \right] = \Gamma_R$ is a property of the right lead.

- G_{N1} is the green's function of the scatterer $\Rightarrow$ $G_{ij} = (EI - H)^{-1}$, where H is the Hamiltonian of the isolated region, and it is a finite matrix.

- $\Delta = 1 + X$

where, $X = -\left(\frac{-\alpha^2}{\gamma_L} e^{ik_L} G_{11} \right) - \left(\frac{-\beta^2}{\gamma_R} e^{ik_R} G_{NN} \right) + \left(\frac{\alpha^2}{\gamma_L} \frac{\beta^2}{\gamma_R} e^{i(k_L+k_R)} \right) (G_{11}G_{NN} - G_{1N}G_{N1})$

Notice that X depends on the self energies (Σ_L and Σ_R) due to left and right leads which are defined as:

$$\Sigma_L = \frac{-\alpha^2}{\gamma_L} e^{ik_L} \qquad , \qquad \Sigma_R = \frac{-\beta^2}{\gamma_R} e^{ik_R}$$

The wave vectors of the left and right leads are:

$$k_L(E) = cos^{-1}\left(\frac{\varepsilon_L - E}{2\,\gamma_L} \right) \qquad \text{and} \qquad k_R(E) = cos^{-1}\left(\frac{\varepsilon_R - E}{2\,\gamma_R} \right)$$

Equation (3.44) is the most general formula to calculate the transmission probability of any scattering region connected to left and right electrodes.

3.5. Generic features of the Transmission curve

Quantum interference [9] is the primary characteristic of electron transport via single molecules. Numerous studies on the quantum interference phenomenon and its impact on transport and thermoelectric properties have been motivated by interest in molecular-scale transport. The transmission function $T(E)$ can exhibit on-resonance (Breit-Wigner resonance) or anti-resonance (decreased transmission) as a result of quantum interference in multi-branched structures. Breit-Wigner resonance and anti-resonance [10]–[12] are manifestations of QI effects in transport curves of single molecules. For a thorough comprehension of these crucial features, this part will involve a brief discussion regarding the properties of these different kinds of resonances.

3.5.1. Breit-Wigner resonance
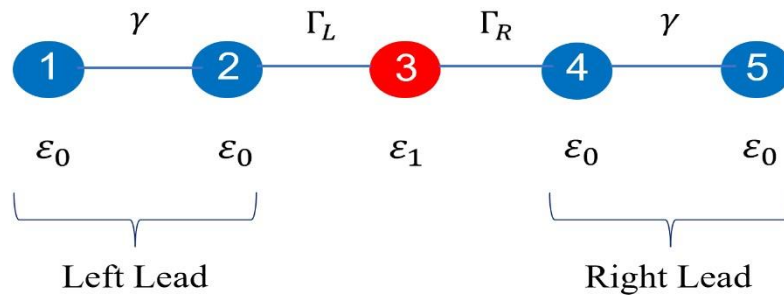
Figure (3.4): A 1-dimensioal system consists of a scattering region of a single atom with a site energy ε_1 in contact by the couplings Γ_L and Γ_R with left and right leads ε_0 linked by the hopping element γ.

The structure above shows a finite linear chain of five atoms, in which each atom occupies a single atomic orbital as expressed in figure (3.4). The one-site energy of the leads (1,2 and 4,5) is equal to $\varepsilon_0 = 0$, and their nearest neighbour coupling is $\gamma = -1$, whereas the single impurity in site (3) has an energy level that sets to $\varepsilon_1 = -0.5$, and it is linked to the left and right leads with couplings $\Gamma_L = \Gamma_R = -0.3$.

Calculating the transmissions coefficient for such a system yields the graph below, which illustrates a Lorentzian shape (Bright-Wigner resonance). This resonance happens when the energy E of the incident electron resonates with an energy level E_n of the isolated region, and the simplest description of this is provided by the Breit-Wigner formula [9]–[11]:

$$T(E) = \frac{4\Gamma_L \Gamma_R}{(E - \tilde{E}_n)^2 + (\Gamma_L + \Gamma_R)^2} \tag{3.45}$$

- Γ_L and Γ_R represent the coupling strength, which link the scattering region to left and right leads, respectively. The width of the resonance is controlled by the coupling Γ. If Γ is strongly coupled to the scattering region, the width of the resonance will be broad, and if it is weakly coupled, then the resonance will be narrow.

- E is the energy of an electron passing through the system.

- $\tilde{E}_n = E_n - (\Sigma_L - \Sigma_R)$ where E_n refers to the eigenenergy of the molecular orbital shifted slightly by an amount of the self-energies $(\Sigma_L - \Sigma_R)$ due to the coupling to the electrodes.

Features of the Breit-Wigner formula:

- If $\Gamma_L = \Gamma_R$ (symmetric junction), and the energy of the electron passing through the system equals to the eigenenergy of the molecule $(i.e.\, E = E_n)$, then the transmission can reach its maximum $T_{max}(E) = 1$, as shown in figure 3.5.

- If $\Gamma_L \ll \Gamma_R$ (non-symmetric junction), the maximum value of the transmission would be less than unity, $T_{max} = (4\,\Gamma_R/\Gamma_L) < 1$ (Figure 3.6).
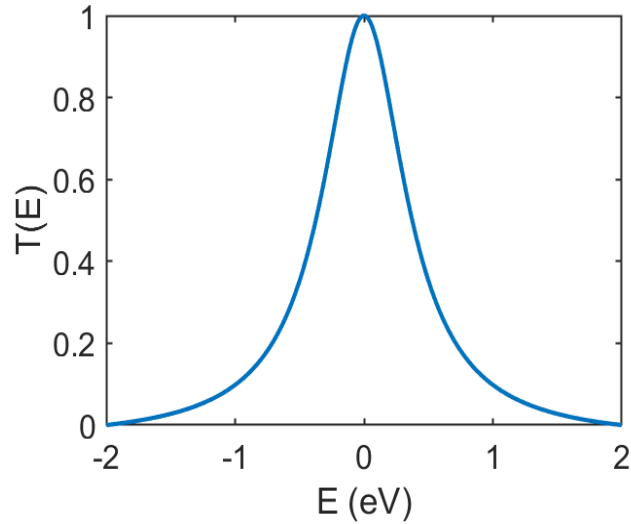
Figure (3.5): A plot of the Breit-Wigner resonance for the system shown in figure 3.4, where $T_{max}(E) = 1$ when $(\Gamma_L = \Gamma_R \; and \; E = E_n)$.
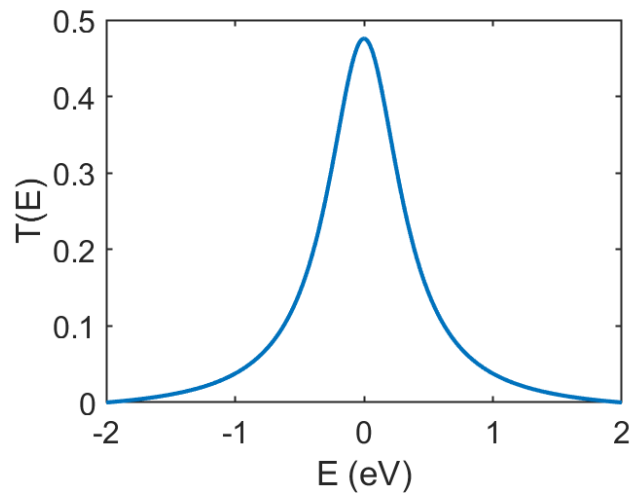
Figure (3.6): A plot of T(E) versus E shows that the height of the resonance is less than unity when $\Gamma_L \ll \Gamma_R$.
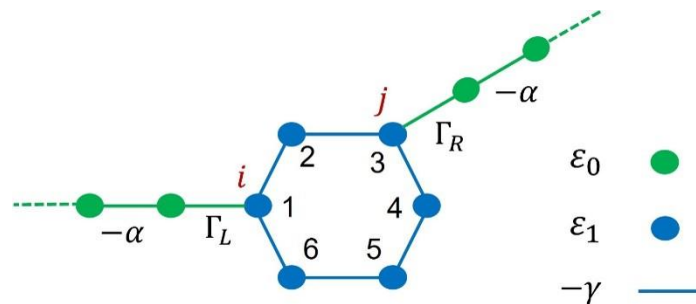
3.5.2. Anti-resonance

Figure (3.7): A tight-binding ring with 6 atomic orbitals ε_1 in contact with semi-infinite leads ε_0 to the positions i and j by the couplings Γ_L and Γ_R from left and right sides. This odd-odd connection (1 and 3) is known as meta connectivity.

Consider a two semi-infinite leads where one is attached to the position $i = 1$, and the other is attached to a different atom j (i and j label atomic orbitals at specific locations within a ring of 6 atoms), figure (3.7).

Imagine a standing wave of an electron of energy E propagates the upper and lower branches of the ring, starting from the point i. If the second lead is located at a node (i.e. $j = 3 \: or \: 5$), then the two paths have different lengths, and the propagated waves will superimpose and coincide at the nodal point (out of the phase) resulting in an anti-resonance feature where the transmission coefficient $T(E)$ vanishes, as shown below.

The Bright-Wigner formula can also provide an information about this important feature. The molecule-electrode coupling strength Γ_L and Γ_R are proportional to $(\varphi_i^n)^2$, $(\varphi_j^n)^2$, respectively, where φ_i^n and φ_j^n represent the amplitudes of the nth molecular orbital on atoms i and j and evaluated at the contacts. Thus, the Green's function $G(j,i) = \varphi_i^n \varphi_j^n / (E - \tilde{E}_n)$ is the

amplitude of a de Broglie wave at j, due to a source at i, and it clearly vanishes when φ_i^n or φ_j^n coincide with nodes [9].
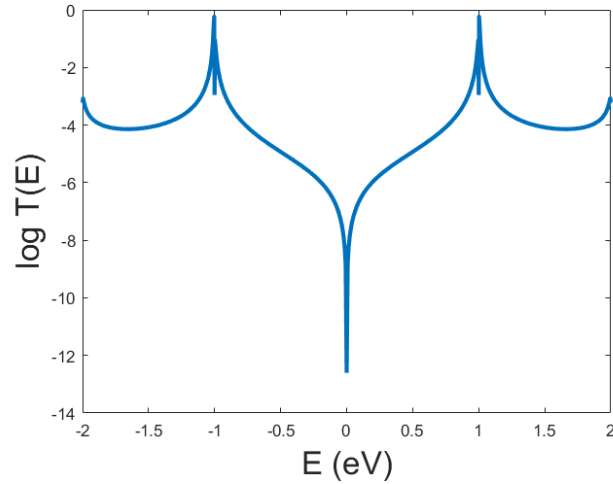
Figure (3.8): The anti-resonance feature where the transmission curve drops to the zero as a result of the destructive quantum interference.

3.6. Green's functions

Previously when we solved the time-independent Schrödinger equation for a system that consists of a scatterer connected to semi-infinite leads, the Green's function arose naturally and took the form:

$$G_{ij} = (EI - H)^{-1}$$

This is satisfied when the Hamiltonian H is a finite matrix corresponding to a closed system such as the scattering region. However, when H is an infinite matrix (i.e. for an open system), this form cannot be used, because it cannot be contained within any available computer memory. Consequently, it is necessary to obtain expressions for the Green's function of an infinite and a semi-infinite system, without explicitly performing the inversion of a matrix. The

benefit of computing the Green's functions [1], [13], [14] is an efficient method for solving scattering problems without explicitly solving the Schrödinger equation. This section will introduce the Green's function method to solve different transport systems.

3.6.1. Green's functions of a doubly infinite linear chain

Consider an open linear chain of sites (atoms) labelled j, in which each site has a single atomic orbital of energy ε_0, with nearest neighbour coupling $-\gamma$, as shown above in figure (3.9).
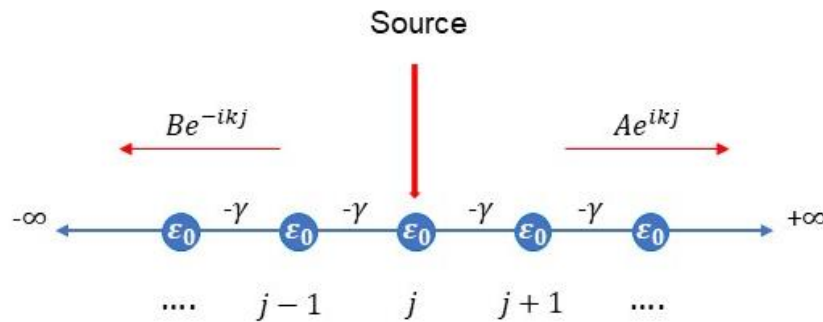
Figure (3.9): A tight binding model of infinite 1-D linear crystalline chain of atoms labelled j with site energy ε_0 connected to each other by the coupling $-\gamma$.

The time-independent Schrödinger equation is:

$$H|\psi\rangle \ = \ E \ |\psi\rangle$$

$$(E - H)|\psi\rangle = 0 \qquad (3.46)$$

The equation for a Green's function of a system described by a Hamiltoinan H is defined as:

$$(E - H)g_{jl} = \delta_{jl} \qquad (3.47)$$

Hence, the equation for a Green's function for an infinite linear chain becomes:

$$\varepsilon_0 g_{jl} - \gamma g_{j-1,l} - \gamma g_{j+1,l} = E g_{jl} - \delta_{jl} \tag{3.48}$$

where δ is kronecker delta $\Rightarrow \delta_{jl} = \begin{cases} 1 & if \quad j = l \\ & or \\ 0 & if \quad j \neq l \end{cases} \tag{3.49}$

The Green's function is a wavefunction due to a source, so introducing a source at site j gives the solutions:

$$g_{jl} = \begin{cases} Ae^{ikj} & for \quad j \geq l \\ Be^{-ikj} & for \quad j \leq l \end{cases} \tag{3.50}$$

where A and B are the amplitudes of two outgoing waves due to an excitation (a source) at point j.

Since the Green's function must be continuous at $j = l$, we can rewrite the solutions as:

$$g_{jl}|_{j=l} = \begin{cases} Ae^{ikl} & where \quad A = D\,e^{-ikl} \\ Be^{-ikl} & where \quad B = D\,e^{ikl} \end{cases} \tag{3.51}$$

Thus, $g_{ll} = D$. Substituting these into (Eq. 3.48) yields.

$$D\left(\underbrace{\varepsilon_0 - 2\gamma cosk}_{E} - 2\gamma isink - E \right) = -1 \tag{3.52}$$

Here, $(E(k) = \varepsilon_0 - 2\gamma \cos(k))$ called the 'dispersion relation' which is useful to obtain the eigenvalues of such a system.

$$D(E - 2\gamma isink - E) = -1$$

$$D = \frac{1}{2\gamma i\,sink} = \frac{1}{i\hbar v(E)} \tag{3.53}$$

where, $v(E) = \frac{dE}{dK} = \left(\frac{2\gamma sink}{\hbar} \right)$ is the group velocity.

Now, substituting the result of D into one of the guess solutions to obtain the Green's function of a doubly infinite linear chain:

$$G_{jl}(E) = \frac{e^{ik(E)|j-l|}}{i\hbar v(E)} \tag{3.54}$$

where, $k(E) = \cos^{-1}\left(\frac{\varepsilon_0 - E}{2\gamma}\right)$

It is important to note that the resulting Green's function in equation (3.54) is called a 'retarded Green's function' $G_{jl}^{(R)}(E)$, and it is not the most general solution. The most general Green's function is defined as:

$$G_{jl}(E) = \frac{e^{ik(E)|j-l|}}{i\hbar v(E)} + \psi_j \tag{3.55}$$

This means any solution of the Schrödinger equation could be added to ψ_j. For example, if one chooses $\psi_j = \frac{-[e^{ik(j-l)} + e^{-ik(j-l)}]}{i\hbar v}$, the corresponding general Green's function would be called an 'advanced Green's function' and takes the form:

$$G_{jl}^{(A)}(E) = \frac{-e^{-ik(E)|j-l|}}{i\hbar v(E)} \tag{3.56}$$

This is the one in which there are two waves coming from $\pm\infty$ and disappear down at point j, which means j is a sink not a source in this situation.

3.6.2. Green's function of a semi-infinite linear chain

$$\psi_j^m = C(e^{-ik(j-m)} + R_j)$$

$$\psi_j^m = C(e^{ik(j-m)} + R_j)$$

Figure (3.10): A tight binding model of a 1-D semi-infinite chain of atoms labelled j with a site energy ε_0 and hopping element $-\gamma$.

Consider a 1-dimentional semi-infinite as shown in figure (3.10), which terminates at site $j = l$. The aim is to obtain the Green's function for such a system. Firstly, it should be noted that the boundary condition at point $j = l$ satisfies that the Green's function must vanish on the first missing atom (i.e., at point $j = l + 1$).

$$\psi_{l+1} = 0 \tag{3.57}$$

It can be noticed that a reflected wave will be created because of an impinging plane wave on the end of the lead. This reflected wave, $R_j = Ae^{-ikj}$, can be chosen such that equation (3.57) is satisfied. One can choose:

$$e^{ik(l+1-m)} + Ae^{-ik(l+1)} = 0 \tag{3.58}$$

$$A = -e^{ik(2l+2-m)} \tag{3.59}$$

Hence,

$$R_j = -e^{-ik(j+m-2l-2)} \tag{3.60}$$

This reflected wave can be added to the retarded Green's function to obtain the Green's function of the semi-infinite chain.

$$G_{jp}(E) = \frac{e^{ik(E)|j-l|} - e^{-ik(j+m-2l-2)}}{i\hbar v(E)} \tag{3.61}$$

This satisfies the boundary condition $\psi_{l+1} = 0$ and $\psi_j^{l+1} = 0$.

Hence, the Green's function at the end of this semi-infinite lead (i.e. on the terminal site l) is:

$$G_{ll}(E) = -\frac{e^{ik}}{\gamma} \tag{3.62}$$

$G_{ll}(E)$ is called the 'surface Green's function' of a semi-infinite lead.

3.6.3. Green's function of 1-dimensional scattering problem
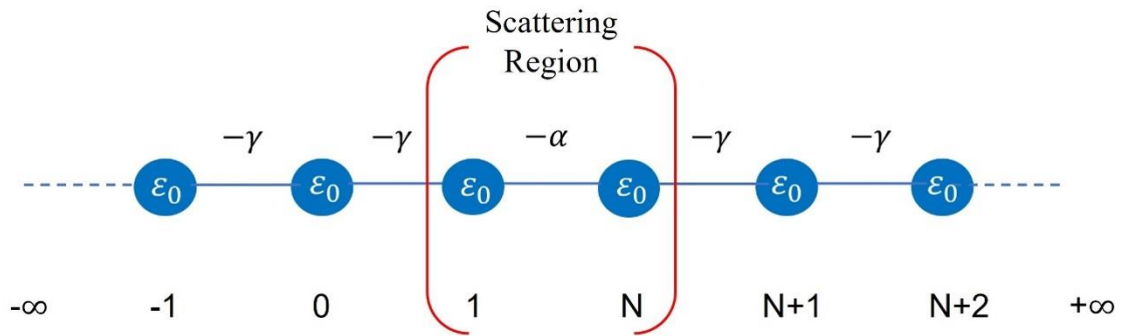
Figure (3.11): Tight binding model of a one-dimensional scattering region coupled by hopping element $-\alpha$ and attached to semi-infinite leads of atoms with a site energy ε_0 and coupling $-\gamma$.

To calculate the Green's function of a system consisting of a scattering region linked with two semi-infinite leads, we need to connect the Green's functions of each separated system of such a structure.

Consider the case where there are two semi-infinite 1-dimensional leads attached to each other by a coupling $(-\gamma)$ with site energy (ε_0) and coupled to a scattering region by hopping element $(-\alpha)$, as shown in figure (3.11).

To solve this scattering problem, let us first write its Hamiltonian form:

$$
\begin{pmatrix}
\ddots & -\gamma & 0 & 0 & 0 & 0 \\
-\gamma & \varepsilon_0 & -\gamma & 0 & 0 & 0 \\
0 & -\gamma & \varepsilon_0 & -\alpha & 0 & 0 \\
0 & 0 & -\alpha & \varepsilon_0 & -\gamma & 0 \\
0 & 0 & 0 & -\gamma & \varepsilon_0 & -\gamma \\
0 & 0 & 0 & 0 & -\gamma & \ddots
\end{pmatrix}
= \begin{pmatrix} H_L & V_c \\ V_c^\dagger & H_R \end{pmatrix}
\tag{3.63}
$$

Here, H_L and H_R represent the Hamiltonians of left and right electrodes, respectively, and the coupling element connecting these two leads is V_c.

To calculate the total Green's function of the whole system, we need to obtain the Green's function of each component of this problem. First, in the case of decoupled system (i.e., when $\alpha = 0$).

$$
g = \begin{pmatrix}
g_L & 0 & 0 \\
0 & g_S & 0 \\
0 & 0 & g_R
\end{pmatrix}
\tag{3.64}
$$

where, g_L and g_R refer to the 'surface Green's function' of left and right semi-infinite leads, and g_S is the Green's function of the scattering region, which have been defined previously as:

$$
g_L = g_R = -\frac{e^{ik}}{\gamma}
\tag{3.65}
$$

$$
g_S = (E - H_S)^{-1}
\tag{3.66}
$$

Here, H_S is the Hamiltonian of the scatterer (closed system), and it is a finite matrix.

Secondly, in the case of coupled system (i.e., when $\alpha \neq 0$), the total Green's function can be computed using Dyson's equation.

$$G = (g^{-1} - V)^{-1} \tag{3.67}$$

where the operator V describing the connection between the two leads.

$$V = \begin{pmatrix} 0 & V_c \\ V_c^\dagger & 0 \end{pmatrix} = \begin{pmatrix} 0 & -\alpha \\ -\alpha^* & 0 \end{pmatrix} \tag{3.68}$$

By solving Dyson's equation (3.67), the Green's function of the whole system will be:

$$G = \frac{1}{\gamma^2 e^{-2ik} - \alpha^2} \begin{pmatrix} \gamma e^{-ik} & -\alpha \\ -\alpha & \gamma e^{-ik} \end{pmatrix} \tag{3.69}$$

The remaining step is to find the transmission (t) and the reflection (r) amplitudes of such a scattering problem which can be calculated using the Fisher-Lee relation.

$$r = i\hbar v G_{0,0} - 1 \tag{3.70}$$

$$t = i\hbar v G_{0,N+1} \, e^{ik} \tag{3.71}$$

These amplitudes are related to travelled particles from the left lead, and similar definitions can be used for incident particles from the right lead.

Based on these amplitudes, the probability in both sides can be written as:

$$T = |t|^2 \quad , \quad T' = |t'|^2 \tag{3.72}$$

$$R = |r|^2 \quad , \quad R' = |r'|^2 \tag{3.73}$$

Eventually, this is the general 1-dimentionasiol approach which Gollum [15] generalises to expand it in 3-dimensional for any arbitrary system [16].

Bibliography:

[1]   Lambert, C.J., 2021. *Quantum transport in nanostructures and molecules*. IOP Publishing.

[2]   Wang, K., 2018. DNA-based single-molecule electronics: from concept to function. *Journal of functional biomaterials*, *9*(1), p.8.

[3]   Landauer, R., 1988. Spatial variation of currents and fields due to localized scatterers in metallic conduction. *IBM Journal of Research and Development*, *32*(3), pp.306-316.

[4]   Büttiker, M., Imry, Y., Landauer, R. and Pinhas, S., 1985. Generalized many-channel conductance formula with application to small rings. *Physical Review B*, *31*(10), p.6207.

[5]   Datta, S., 1997. *Electronic transport in mesoscopic systems*. Cambridge university press.

[6]   Landauer, R., 1987. Electrical transport in open and closed systems. *Zeitschrift für Physik B Condensed Matter*, *68*(2), pp.217-228.

[7]   Segal, D., Nitzan, A. and Hänggi, P., 2003. Thermal conductance through molecular wires. *The Journal of chemical physics*, *119*(13), pp.6840-6855.

[8]   Famili, M., 2018. *Theory of molecular scale thermoelectricity*. Lancaster University (United Kingdom).

[9]   Lambert, C.J., 2015. Basic concepts of quantum interference and electron transport in single-molecule electronics. *Chemical Society Reviews*, *44*(4), pp.875-888.

[10]   Wang, R.N., Dong, G.Y., Wang, S.F., Fu, G.S. and Wang, J.L., 2016. Impact of contact couplings on thermoelectric properties of anti, Fano, and Breit-Wigner resonant junctions. *Journal of Applied Physics*, *120*(18), p.184303.

[11]   García-Suárez, V.M., Ferradás, R. and Ferrer, J., 2013. Impact of Fano and Breit-Wigner resonances in the thermoelectric properties of nanoscale junctions. *Physical review b*, *88*(23), p.235417.

[12]   Claughton, N.R., Leadbeater, M. and Lambert, C.J., 1995. Theory of Andreev resonances in quantum dots. *Journal of Physics: Condensed Matter*, *7*(46), p.8757.

[13] Odashima, M.M., Prado, B.G. and Vernek, E., 2016. Pedagogical introduction to equilibrium Green's functions: condensed-matter examples with numerical implementations. *Revista Brasileira de Ensino de Física*, *39*.

[14] Economou, E.N., 2006. *Green's functions in quantum physics* (Vol. 7). Springer Science & Business Media.

[15] Ferrer, J., Lambert, C.J., García-Suárez, V.M., Manrique, D.Z., Visontai, D., Oroszlany, L., Rodríguez-Ferradás, R., Grace, I., Bailey, S.W.D., Gillemot, K. and Sadeghi, H., 2014. GOLLUM: a next-generation simulation tool for electron, thermal and spin transport. *New Journal of Physics*, *16*(9), p.093029.

[16] Sanvito, S., Lambert, C.J., Jefferson, J.H. and Bratkovsky, A.M., 1999. General Green's-function formalism for transport calculations with spd Hamiltonians and giant magnetoresistance in Co-and Ni-based magnetic multilayers. *Physical review B*, *59*(18), p.11936.

Chapter 4

The role of anchor groups in controlling the transport of single molecule junctions

4.1. Introduction

One of the main challenges in molecular electronic research is understanding the fundamental behaviour of electronic transport through single-molecule junctions [1], [2]. To enhance this knowledge, various experimental approaches for contacting single molecules have been developed [3], [4]. In recent years, it has been obvious that the electronic properties of a molecular junction are treated as a result of the entire (metal–molecule–metal) system, which has to be considered in order to comprehend the variables that influence charge transfer [5]. A single-molecule junction consists of three components: the molecular bridge, the electrode and the anchor (part of the molecule which binds to the electrode). The electronic coupling between each component has a significant impact on the fundamental charge-transport properties of the junction [6]. This begs the question: what happens when an isolated molecule and metal electrodes (such as gold) are brought into contact?

The isolated molecule has a discrete set of energy levels called frontier orbitals (HOMOs and LUMOs), whereas the metal electrodes have a band structure consisting of a continuum of states with a well-defined Fermi energy. Bringing these two components close together causes an interaction between them, leading to different physical effects, for example, the charge transfers between the two systems, and hence electron donating to or withdrawing from the

molecule affects the energy levels of both the molecule and the contact. Due to this transfer of the charge, the HOMO (highest occupied molecular orbital) and LUMO (lowest unoccupied molecular orbital) could be shifted up or down, resulting in a larger or smaller slope in the transmission function at the Fermi level [7]. The position of molecular orbitals relative to the Fermi level of the electrodes are therefore influenced by the type of the chemical bonds in the anchor group, which bind the molecules chemically to the electrodes.

The aim of this chapter is to investigate the reason behind the pinning of the DFT-predicted Fermi energy (0 eV) to the resonances. In particular, I shall determine anchor groups tune the position of the electrode Fermi level relative to the molecular resonances such as thiol (-SH), methyl sulfide (-SMe), and pyridyl (Py), which couple different molecules to Au electrodes.

4.2. Molecular Structures

Herein, the model systems consist of three different molecules with symmetric couplings at each end, where the DFT Fermi energy can pin to one of the resonances as in the case of a) Octane-dithiol (ODT), b) OPE-dithiol and c) 4,4`-Bipyridine. For asymmetric linkers, anthracene-based molecule has been studied theoretically and experimentally with both symmetric and asymmetric anchors [8]–[10]. Therefore, in this study I chose anthracene to be terminated by different anchors: d) Anthracene (Py-SMe) and e) Anthracene (Py-thiol), as illustrated in figure (4.1).
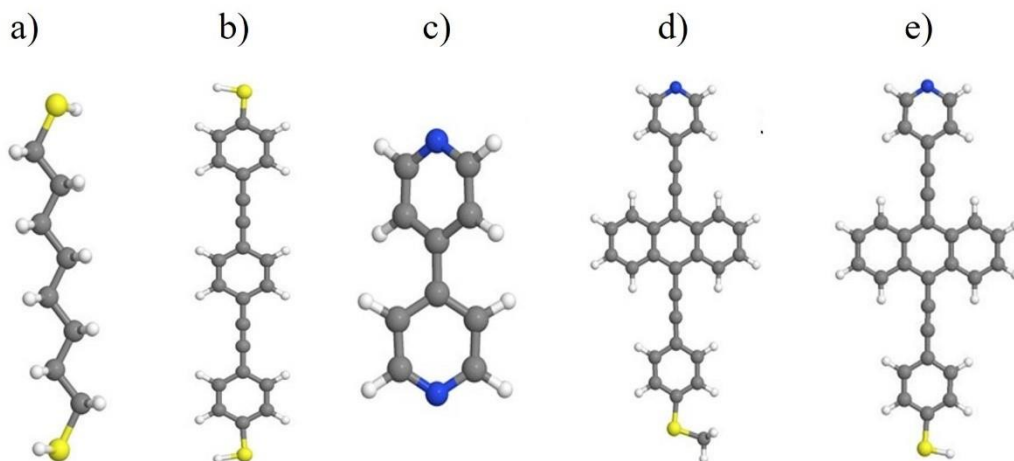
Figure (4.1): Atomic structures of: a) Octane-dithiol, b) OPE-dithiol, c) 4,4`-Bipyridine,

d) and e) Anthracene core with (Py-SMe) and (Py-thiol) anchors, respectively.

4.3. Theoretical Method

To obtain the optimum geometry of these molecules, DFT calculations with the GGA-PBE exchange correlation functional [11] were performed with a plane wave cut-off of 150 Rydbergs as implemented in the SIESTA package [12], [13]. A double-zeta polarized atomic-orbital basis set (DZP) was applied for all atoms except the gold atom where it has a double-zeta basis set (DZ). For each structure, the geometry optimization is performed to a force tolerance of $0.01\ eV/Å$. It is important to find the optimum dihedral angle between the two pyridyl rings of the 4,4`-bipyridine molecule, and this is done by calculating the total energy for different rotated angles starting from 0° to 360°. The optimum angle is found to be around 30° (figure 4.2). Furthermore, the counterpoise [14], [15] method (CP) in chapter 2 (section 2.6.2) is utilized to compute the binding energy (B.E) or the optimum bond length between the anchor groups and the gold atom of the tip lead. In my DFT calculations, the optimum

separation distances between N-Au, S-Au and SMe-Au bonds are determined to equal 2.3Å, 2.4Å and 2.6Å, at -0.39eV, -1.30eV and -0.5eV, respectively (figures 4.3, 4.4, 4.5).

After all the geometries were relaxed and the binding geometry calculated, I connected each side of the molecules with a gold pyramid tip linked with five layers of Au (111), where each layer has 5×5 Au atoms. Then, the transport properties of the molecular junctions were calculated using the Green's function formalism as implemented in the transport Gollum package [16].
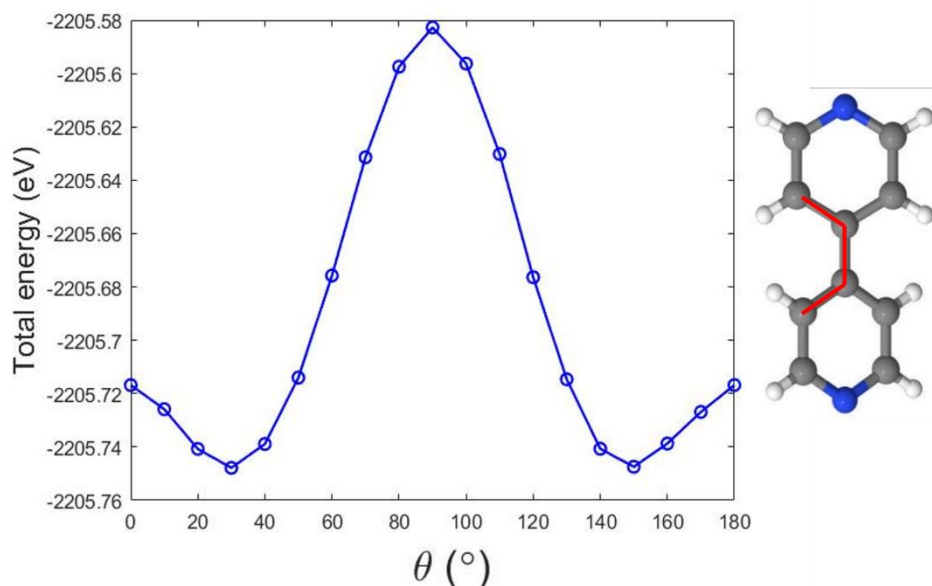
Figure (4.2): The curve illustrates the evaluated total energy at each torsion angle θ from 0° to 180°, where the optimum angle is determined to be at 30°. Right panel shows the dihedral angle between the two pyridyl rings (red line).
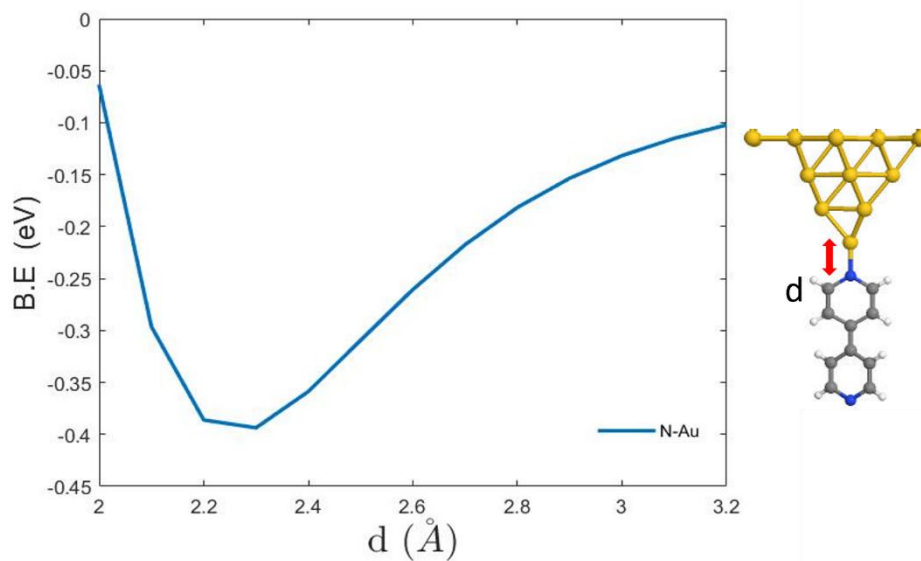
Figure (4.3): Binding energy versus distance between the N-Au, where the optimum ground

state energy is determined at distance $d = 2.3$Å.
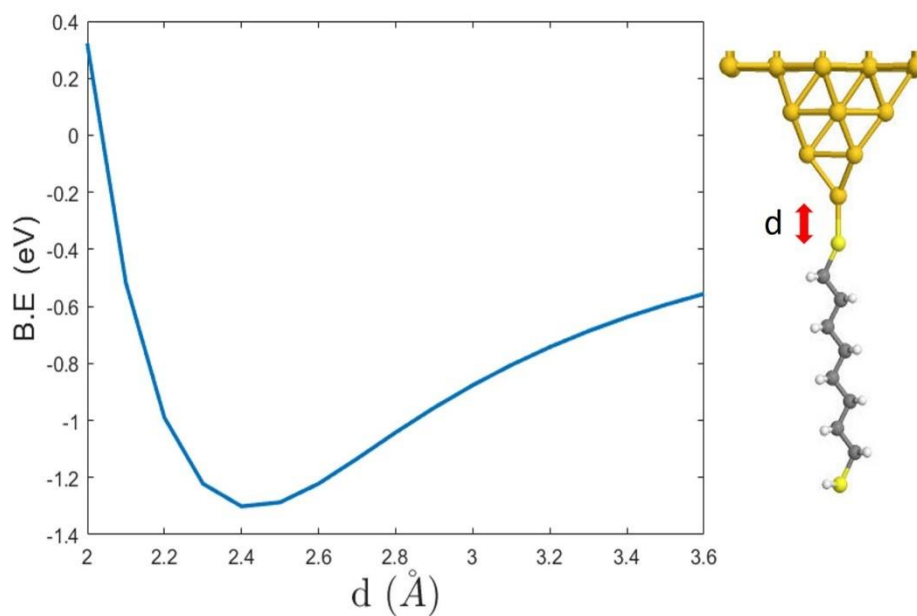
Figure (4.4): Binding energy versus distance plot between the S-Au, where the optimum

ground state energy is determined at distance $d = 2.4$Å
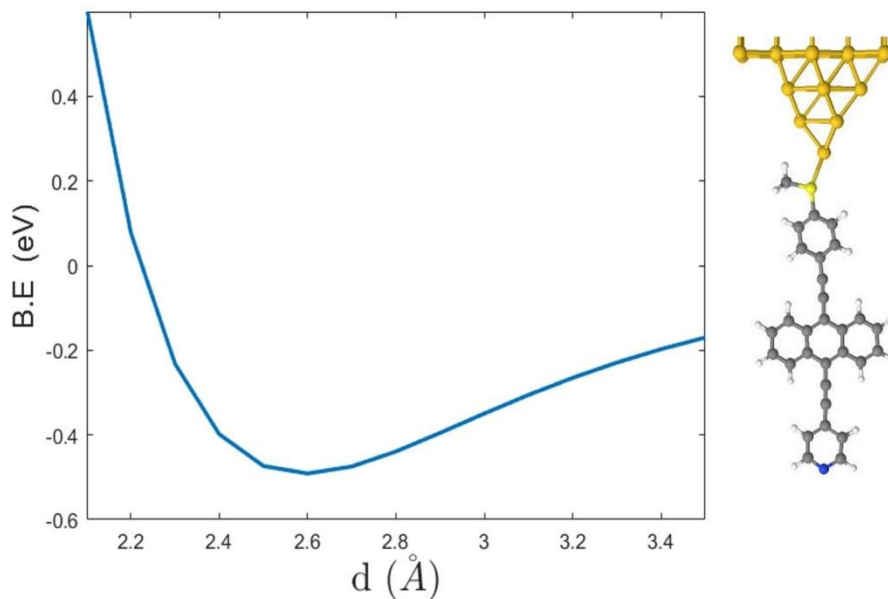
Figure (4.5): Binding energy versus distance between the SMe-Au, where the optimum ground state energy is determined at distance = 2.6Å, and the angle between C-S-Au=150°.

4.4. Results and discussion

4.4.1. The effect of anchors on the electrode Fermi level (E_F)

Based on density functional theory (DFT), varying the anchor groups of single molecules to external electrodes can be used to control their electrical conductance [17], [18]. The relative position of the metal Fermi level (E_F) in the transmission function, when the molecules are coupled to electrodes, is usually dependant on the anchor groups attached to the ends of that molecule. For example, molecules with thiol (-SH) anchor group, such as OPE-dithiol and octane-dithiol, result in HOMO dominated transport, meaning that E_F is located close to the HOMO resonances (figure 4.6 and 4.7). In contrast, bipyridine with pyridyl anchors attached to Au leads yields LUMO dominated transport (figure 4.8), and so the transmission

significantly relies on the position of the lowest unoccupied molecular orbital (LUMO). On the other hand, in the case of different anchor groups connected to a molecule such as anthracene with Py-SMe, the Fermi energy of the gold electrode is found to be located near the LUMO resonance, resulting in LUMO dominated transport (figure 4.9), whereas in anthracene with (Py-thiol) linkers the position of the Fermi level sits in the middle of the HOMO-LUMO gap (figure 4.10). All these results show that the coupling to the leads can have a profound effect on the level alignment (i.e. the molecular orbitals), causing a shift in the resonances with respect to E_F of the electrode.
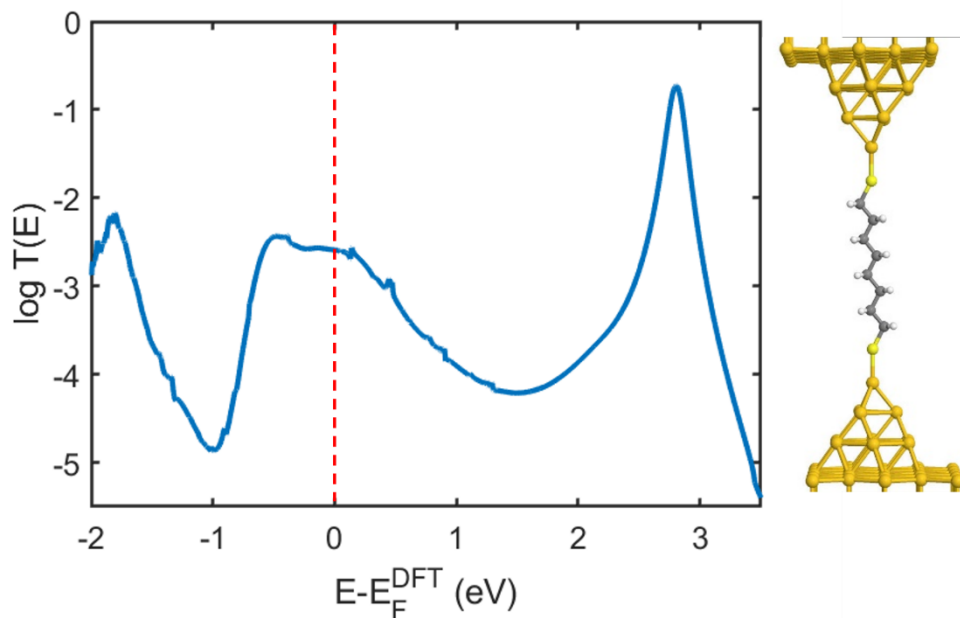
Figure (4.6): The transmission curve of octane-dithiol, and the transport is HOMO dominated since the tail of the HOMO peak is closer to the electrode Fermi energy $(E_F = 0eV)$.
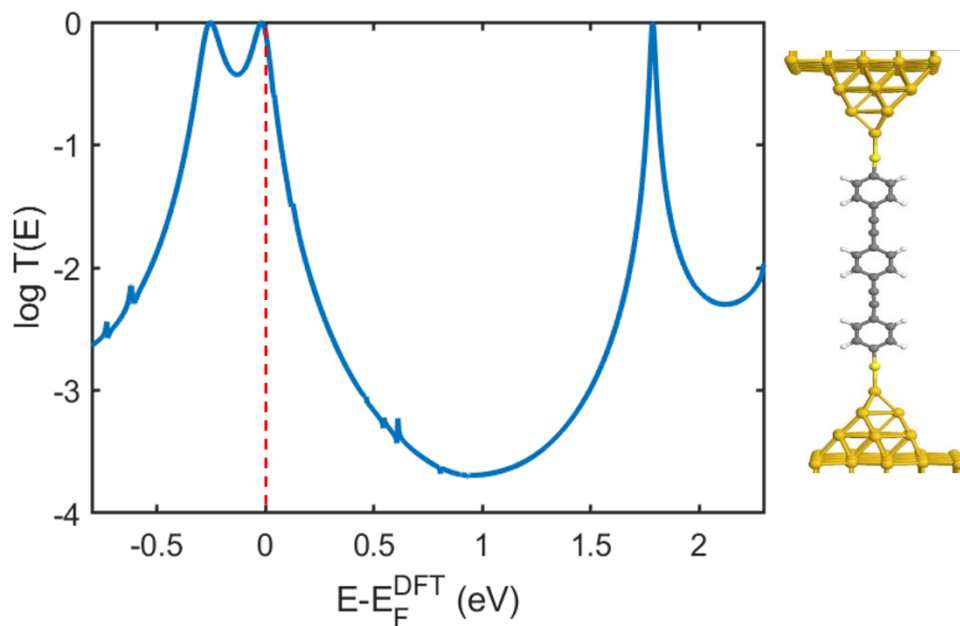
Figure (4.7): The transmission curve of OPE-dithiol, and the transport is HOMO dominated since the HOMO resonance is closer to the electrode Fermi energy $(E_F = 0eV)$.
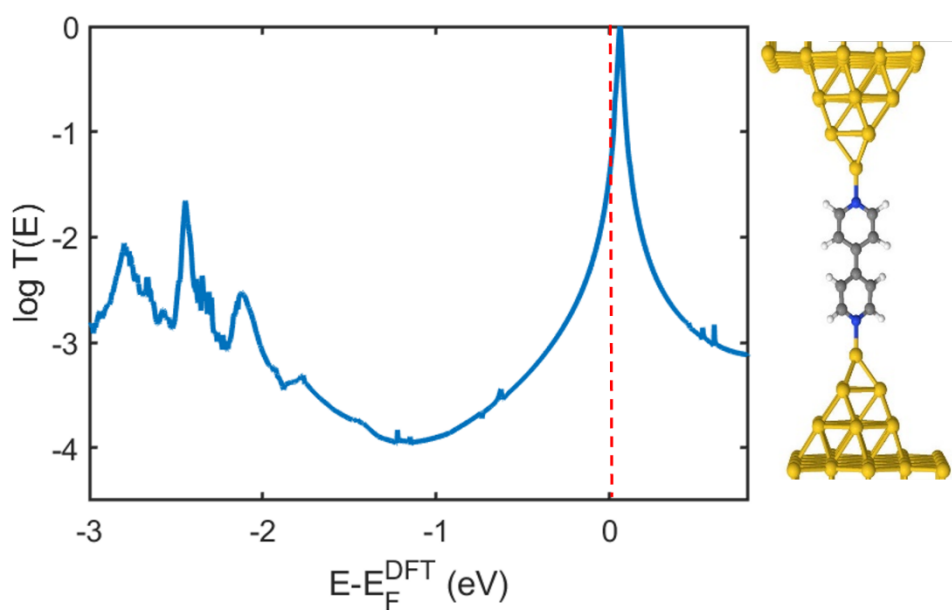
Figure (4.8): The transmission curve of bipyridine, and the transport is LUMO dominated since the LUMO resonance is closer to the electrode Fermi energy $(E_F = 0eV)$.
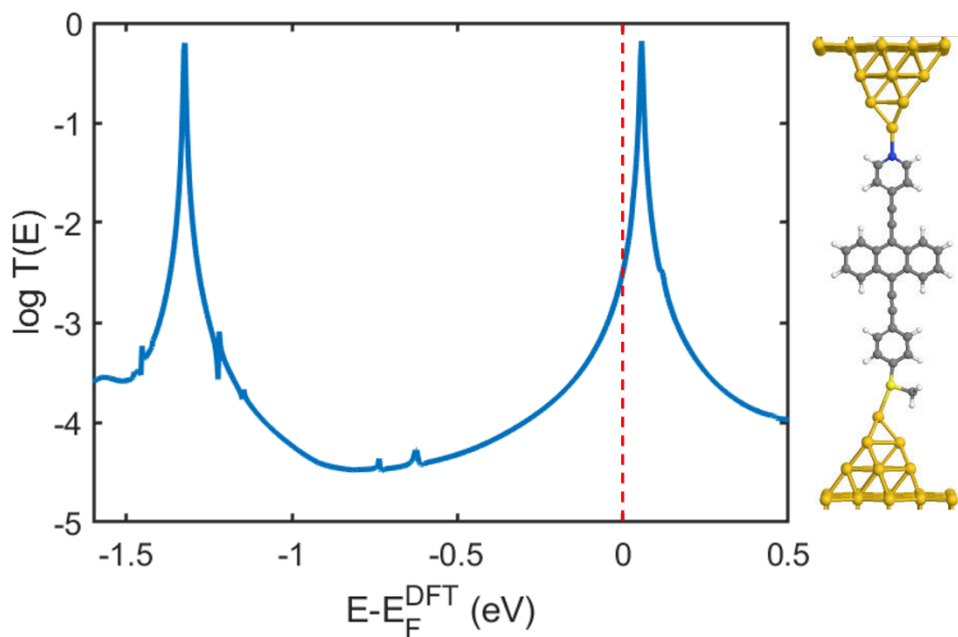
Figure (4.9): The transmission curve of anthracene Py-SMe, and the transport is LUMO dominated since the LUMO resonance is closer to the electrode Fermi energy $(E_F = 0 eV)$.
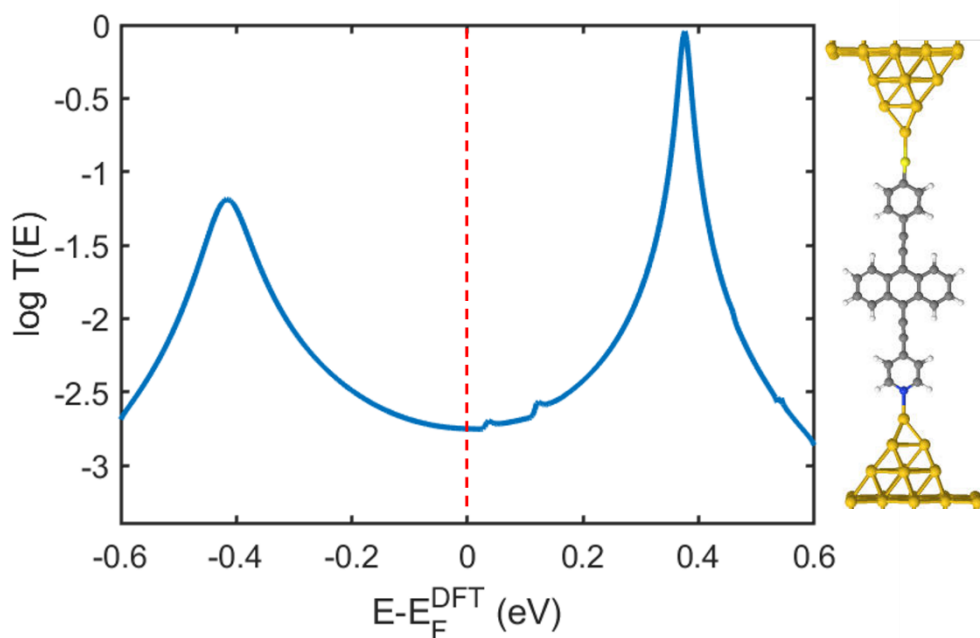
Figure (4.10): The transmission curve of anthracene Py-thiol with the position of the Fermi level of the electrode in the middel of the HOMO-LUMO gap.

4.4.2. Transmission behaviour

To understand the transmission behaviour of these different molecules, I plotted their frontier orbitals with their energy levels in the gas phase, as shown in figure (4.11). It can be noticed that in the case of alkane, OPE and bipyridine the eigenvalues of the HOMO and HOMO-1 are not well separated because of the degeneracy, and therefore the HOMO resonances in the transmission curves do not possess a single Lorentzian shape. To have normal bright-Wigner resonances, the separation of the eigenvalues should be greater than the coupling between them. Thus, if the energy levels are closed together, they mix and result in a resonance that can have any shape, which means the bright-Wigner Formula is not valid in this situation.

For the anthracene transmission, the HOMO resonance with (Py-thiol) coupling does not reach the unity compared to anthracene (Py-SMe). This can be explained through the feature of the Breit-Wigner formula in chapter 3 (section 3.5.1). If $\Gamma_L \gg \Gamma_R$, the peak of the molecular resonance would be less than unity, $T_{max} = (4\,\Gamma_R/\Gamma_L) < 1$. The idea is that if there are asymmetric anchor groups, the coupling between them would be similar or different depending on their behaviour. Pyridyl and thiol have large difference in their behaviours, where one acts as a donor while the other behaves as an acceptor, and this might the reason for why the HOMO is less than unity. However, when the couplings are asymmetric, but they behave similarly, then this will not have a large effect in the Breit-Wigner formula. For this reason, in the case of (Py-SMe), the couplings are similar in their behaviours where both tend to act as donors (as shown in section 4.4.5), and therefore the resonances tend to reach the unity.
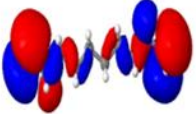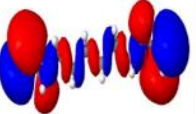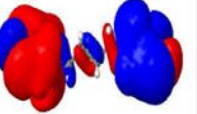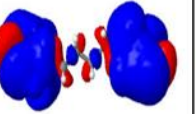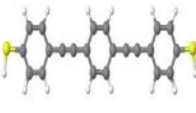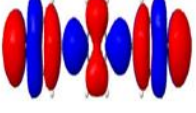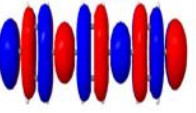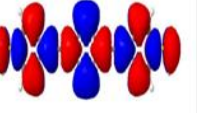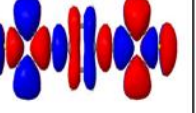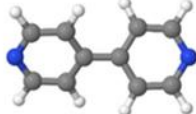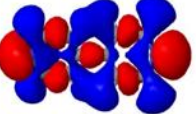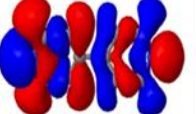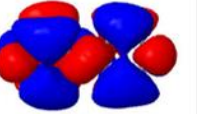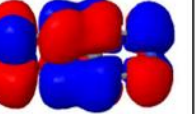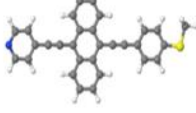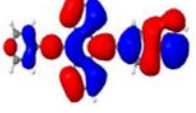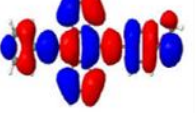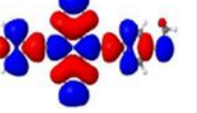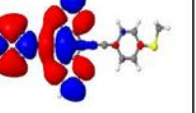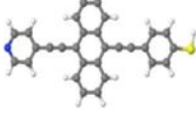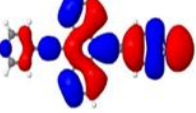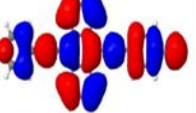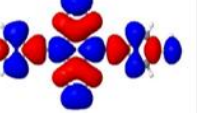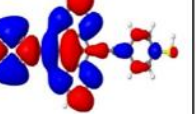
Structure	HOMO-1	HOMO	LUMO	LUMO+1
$E_F = -2.85$ eV	-4.64 eV	-4.61 eV	0.75 eV	0.78 eV
$E_F = -3.17$ eV	-4.67 eV	-4.17 eV	-1.98 eV	-1.05 eV
$E_F = -4.48$ eV	-5.25 eV	-5.23 eV	-1.91 eV	-1.03 eV
$E_F = -3.35$ eV	-4.79 eV	-4.09 eV	-2.65 eV	-1.39 eV
$E_F = -3.41$ eV	-4.97 eV	-4.17 eV	-2.69 eV	-1.43 eV

Figure (4.11): Frontier molecular orbitals of the studied five molecules in the gas phase with their eigenvalues obtained from DFT, where red corresponds to positive and blue to negative regions of the wave functions. HOMO and HOMO-1 in alkane, OPE and bipyridine are not separated well where the Their eigenvalues are very close to each other.

4.4.3. Seebeck behaviour

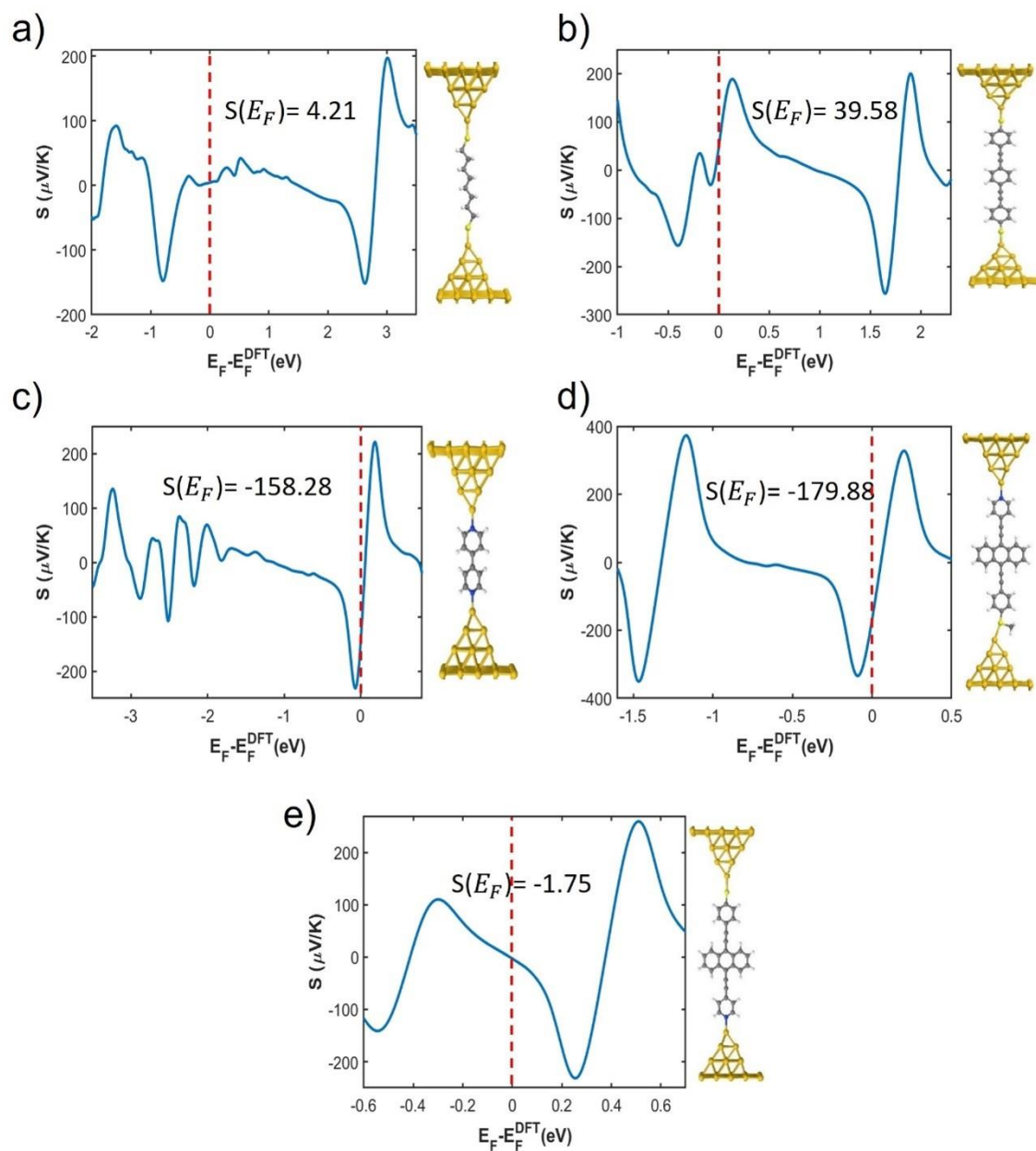**Figure (4.12):** The Seebeck behaviour of the studied molecule, a) Octane-dithiol, b) OPE-dithiol, c) 4,4`-Bipyridine, d) and e) Anthracene core with (Py-SMe) and (Py-thiol) anchors, showing its sign and magnitdue depending on the position of the DFT electrode Fermi energy (0eV).

The transmission coefficient $T(E)$ of a molecular junction can provide information regarding the Seebeck coefficient (S) via the Mott formula [19]:

$$S = -\frac{\pi^2 k_B^2 T}{3|e|}\left(\frac{\partial \ln(T(E))}{\partial E}\right)_{E=E_F}$$

where k_B is the Boltzmann constant, T is an absolute temperature, and e is the electron charge. From this equation, S has a negative sign and is proportional to the slope of $T(E)$ at E_F. This means that when the HOMO peak is nearest to the Fermi energy E_F, $T(E)$ has negative slope at E_F and S is then positive, whilst when the LUMO resonance is closest to E_F, $T(E)$ has positive slope at E_F and S is therefore negative. In figure (4.12), the Seebeck coefficient has been evaluated at the electrode's Fermi level ($E_F = 0eV$) to obtain its sign and magnitude for each molecule. Looking at the Seebeck coefficient of a system can give an insight of how to control the position of the Fermi energy in order to design a good thermoelectric material. It can be seen that the symmetric coupling to the leads has a pinning behaviour, where the position of E_F indicates HOMO dominated transport (positive sign of S) such as OPE-dithiol and octane-dithiol or LUMO dominated transport (negative sign of S) as shown in bipyridine and anthracene (Py-SMe), and these are in a good agreement with the obtained sign of the Seebeck in the experimental studies [9], [20]. Due to the pinning, any external effect would be added to the backbone of these molecules would not shift the E_F to a different position. In contrast, the position of the E_F in the presence of asymmetric coupling, e.g. anthracene with Py-thiol, is located in the middle of the gap and does not seem to pin to the HOMO or LUMO resonance. This might give a scope to modify the Seebeck if we add some external potential to the asymmetric molecule [21], which could shift the resonances in some way with respect to the Fermi energy, leading to a change in the sign of the Seebeck coefficient. The idea of this asymmetric coupling could be exploited in order to produce a large effect in the Seebeck coefficient with a combination of the quantum interference effect.

4.4.4. Energy shifting
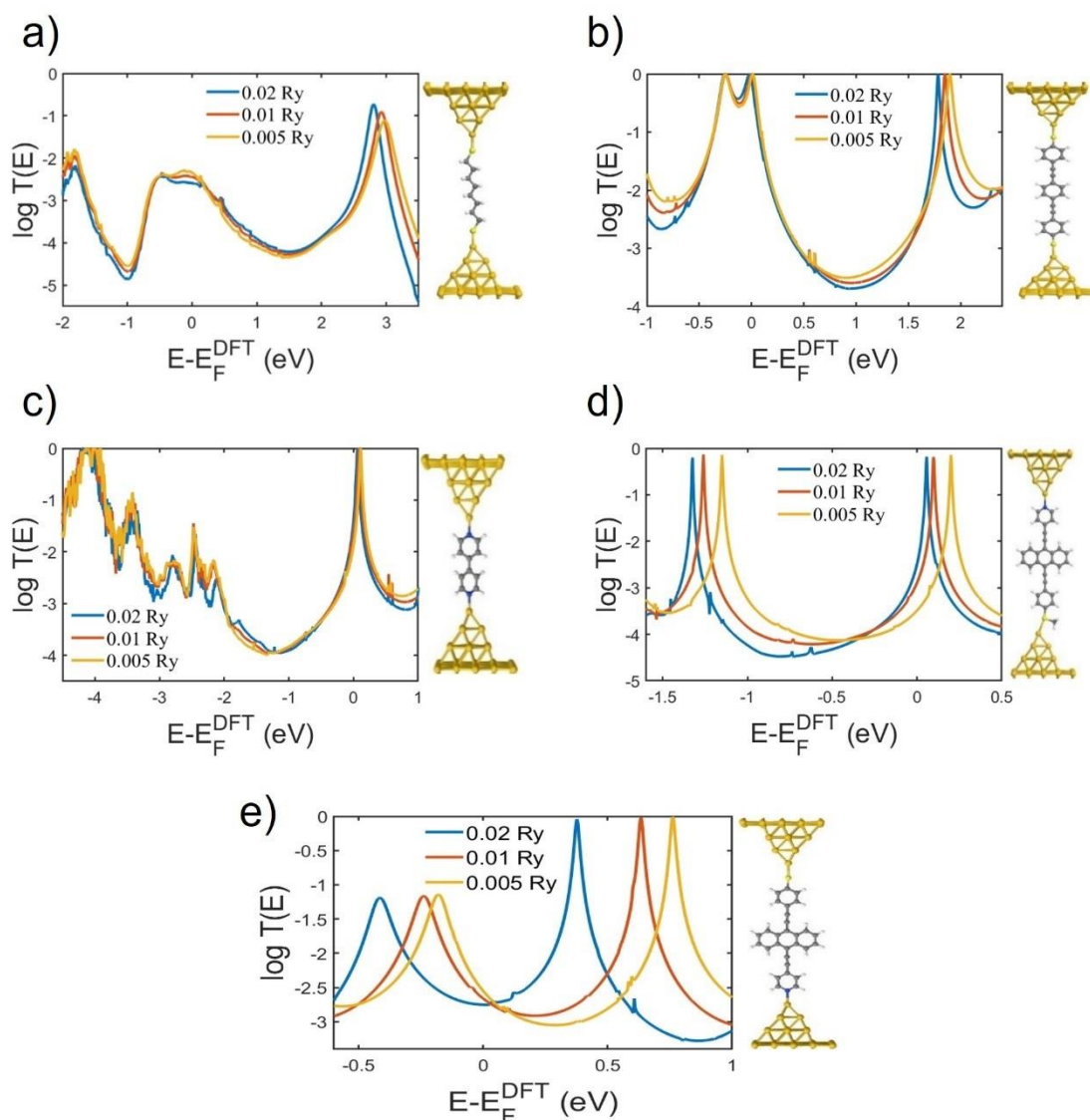
Figure (4.13): The resonances of molecules a, b and c with symmetric anchors are pinned to the $E_F = 0eV$, whereas d and e with Py-SMe and Py-thiol (asymmetric anchors) the transmission are shifted up and down with changing the basis sets from 0.02 to 0.005 Ry.

To further understand why the Fermi energy behaves as it does in terms of the DFT calculation, I have investigated the transport properties of these molecules for different parameterizations of the calculates. The first is the nature of the basis set used in the calculation. The energy shift

parameter in SIESTA determines the spatial confinement of the numerical atomic orbitals, giving us an option to change the cut-off radius of all the atoms in a fixed manner. To examine this effect, I increased the length of the confinement to see how it changes the behaviour of the calculation. A short confinement basis set corresponds to an energy shift of 0.02 Rydbergs, and a large confinement basis set to an energy shift of 0.005 Ry.

In the case of the anthracene molecule with different anchor groups, the transmission curves with different confinements have the same shape, and as the basis set is changed, the transmission resonances are shifted up in energy and the Fermi energy is shifted away from the LUMO resonance (figure 4.13). The position of the electrode Fermi energy here is dependent on the parametrization of the basis set. The interesting thing then when the same range of basis sets are used to calculate octane-dithiol, OPE-dithiol and bipyridine, the results show that the position of the Fermi energy is not dependent on the basis set (i.e. E_F is always fixed to that position). Therefore, it is inferred that with symmetric anchor groups at both ends of a molecule, changing the basis set does not have an effect on the Fermi energy location, and the pinning to the resonances whether HOMO or LUMO dominates. On the other hand, the energy levels are shifted by varying the basis set when the anchor groups are asymmetric, resulting in different Fermi energy positions like in anthracene case. It seems that adding SMe or thiol to the other side of the anthracene breaks the pinning behaviour caused by Py linker (figure 4.13).

If I relate the transmission behaviour of bipyridine and anthracene (Py-SMe) to their energy levels in the gas phase (table 4.14), I find similar trend in the energy shifting of both cases (i.e., the energy shifting of bipyridine in the gas phase follows the same behaviour as in anthracene (Py-SMe). In terms of the transmission behaviour, we expect in both molecules a relative shift in the position of the HOMO and LUMO with respect to the Fermi energy for different basis sets. It should mean that the position of the Fermi energy is dependent on the basis sets in both

molecules. However, the transmission of bipyridine does not show that; the transmission curves look the same, and the electrode Fermi energy sits on the same location (figure 4.13 b).

Bipyridine	HOMO	LUMO
0.02 Ry	-5.23	-1.91
0.01 Ry	-5.72	-2.38
0.005 Ry	-5.97	-2.62

Anthracene Py-SMe	HOMO	LUMO
0.02 Ry	-4.09	-2.65
0.01 Ry	-4.51	-3.06
0.005 Ry	-4.73	-3.29

Table (4.14): The table shows the energy levels of bipyridine (top one) and anthracene (Py-SMe) (bottom one) in the gas phase with different basis sets.

To investigate why this pinning behaviour occurs, I looked at how the charge on molecules changes when they are connected to the gold electrodes, and how this is affected by varying the basis set in the calculation. This can be studied within the density functional theory (DFT), which provides information through population analysis (a tool for counting electrons in the system).

4.4.5. Population analysis

There are different methods for counting electrons in a DFT calculation: Mulliken population analysis [22], Hirshfeld population analysis [23] and Voronoi population analysis [24]. Hirshfeld and Voronoi are considered to be more accurate methods for computing the charge transfer, where they are based on partitioning the space into regions for each atom to calculate electron density. In contrast, the Mulliken approach is based on the linear combination of atomic orbitals (LCAO), and it is less accurate compared to the other two.

Table (4.15) shows the behaviour of charge distribution in Mulliken, Hirshfeld and Voronoi for octane-dithiol with different basis sets. The total number of electrons for the isolated A gas-phase octane-dithiol has 60 electrons, and therefore the extra electrons are gained from the gold leads. It can be seen, as we increase the confinement of the basis set from 0.02 to 0.005 Ry, the Mulliken population shows similar behaviour, where octane-dithiol always gains electrons from the gold. The Hirshfeld and Voronoi both have a negative charge in all the three basis sets, meaning that the electrons transfer from the gold to the molecule. This is a good example of a robust conclusion regarding the populations of this molecule. Similar behaviour occurs with OPE-dithiol (table 4.15), which is straightforward to interpret in terms of thiol anchor group. In the gas phase, thiol has one electron from the connected hydrogen atom, but it is assumed to lose that electron due to the cleaved hydrogens, forming an efficient electronic coupling with the gold electrodes [25]. This means that sulfur atoms here behave as an acceptor (i.e., charge is transferred from the gold to the molecule), and the pinning of the E_F to the HOMO is due to strong S-Au covalent bonding.

Octane-dithiol	Mulliken	Hirshfeld	Voronoi
0.02 Ry	60.692	-0.615	-0.637
0.01 Ry	60.541	-0.454	-0.483
0.005 Ry	60.493	-0.388	-0.421
OPE-dithiol	Mulliken	Hirshfeld	Voronoi
0.02 Ry	112.875	-0.806	-0.837
0.01 Ry	112.661	-0.592	-0.62
0.005 Ry	112.566	-0.474	-0.514

Table (4.15): The charge distribution for octane-dithiol (tope one) and OPE-dithiol (bottom table) at different basis sets using Mulliken, Hirshfeld and Voronoi methods.

In the bipyridine case, Hirshfeld and Voronoi populations show identical trends in all the basis sets (table 4.16), where the charges transfer from the molecule onto the gold (positive sign). The bipyridine has a lone pair at the ends of the HOMO orbital with two extra electrons (figure 4.11), and these extra electrons will be donated once the gold leads attached to the molecule. However, the Mulliken population here behaves differently upon changing the basis sets. The total number of electrons for the isolated molecule (i.e., bipyridine) is 58 electrons, so with a short basis set (0.02 Ry) this total has increased by almost 0.017 electrons, meaning that the gold donated some electrons to the molecule, whereas with longer basis sets (0.01 & 0.005 Ry)

the electrons transferred from the molecule to the gold, as shown in the table (4.16). This means that Mulliken population is less accurate, because the electron transfer should not be positive and negative in the same basis set.

Bipyridine N-Au= (2.3Å)	Mulliken	Hirshfeld	Voronoi
0.02 Ry	58.017	0.045	0.012
0.01 Ry	57.911	0.186	0.18
0.005 Ry	57.842	0.26	0.276

Table (4.16): The charge distribution for bipyridine (strongly coupled) at different basis sets using Mulliken, Hirshfeld and Voronoi methods.

Anthracene Py-thiol	Mulliken	Hirshfeld	Voronoi
0.02 Ry	143.483	-0.422	-0.453
0.01 Ry	143.36	-0.273	-0.297
0.005 Ry	143.289	-0.195	-0.207

Table (4.17): The charge distribution for anthracene (Py-thiol) at different basis sets using Mulliken, Hirshfeld and Voronoi methods.

In the case of asymmetric anchor groups, e.g. anthracene (Py-thiol), the charge transfers from the gold electrodes (negative sign) to the molecule in all the basis set (table 4.17). This means that the effect of thiol anchor is stronger than Py.

In anthracene (Py-SMe), table (4.18) shows different direction of the charge transfer when changing from 0.02 to 0.01 Ry, wherein the molecule gained electrons (negative sign) with short basis set (0.02 Ry), whilst with the other basis sets (0.01 & 0.005 Ry) it had positive charge (donating electrons).

Anthracene Py-SMe	Mulliken	Hirshfeld	Voronoi
0.02 Ry	150.131	-0.087	-0.125
0.01 Ry	149.929	0.126	0.123
0.005 Ry	149.833	0.213	0.226

Table (4.18): The charge distribution for anthracene core with (Py-SMe) anchors at different basis sets using Mulliken, Hirshfeld and Voronoi methods.

The interesting thing here is the change in the sign of the charge distribution. It is expected that the general trend would be the same whether gaining or losing electrons, but here in the case of (Py-SMe), there is different direction of the charge transfer between 0.02 Ry and the other two.

Anthracene has different anchor groups, so how do different anchor groups behave in a single molecule? We have shown that pyridyl (Py) acts as a donor anchor and thiol behaves as an acceptor, but SMe needs to be tested. A methyl sulfide (-SMe) linker consists of a sulfur atom

attached to a methyl group (one carbon atom bonded to three hydrogen atoms $-CH_3$). Due to that, SMe is weakly coupled to the gold electrode compared to thiol. To understand the effect of SMe anchor on the charge distribution, I linked OPE molecule to SMe from both sides and calculated Mulliken, Hirshfeld and Voronoi populations for the same chosen basis sets (see table 4.19). In OPE-SMe, the charge transfers from the gold to the molecules (negative sign) with both 0.02 Ry and 0.01 Ry basis sets similarly to the behaviour of the thiol anchor. However for the long basis set (0.005 Ry), the charge transfers to the gold (positive charge). Here, SMe anchor behaves as an acceptor or a donor depending on the basis set. For this reason, SMe in anthracene molecule tends to act as an acceptor (negative charge) with short basis set (0.02 Ry), but as the basis set is increased, pyridyl and SMe both behave as a donor. It seems that the donating effect from the Py anchor maybe stronger than the accepting effect from the SMe, resulting in LUMO dominated transport.

Bipyridine and anthracene (Py-SMe) behave similarly in terms of the charge transfer (i.e. both donating electrons to the electrodes with long basis sets), and also, I show similar behaviour of their energy shifting in the gas phase. The only difference between the two is that the former shows pinning although with increasing the basis sets, while the latter does not show this pinning behaviour. Due to that, I need to explore the reason behind the pinning in the bipyridine transmission.

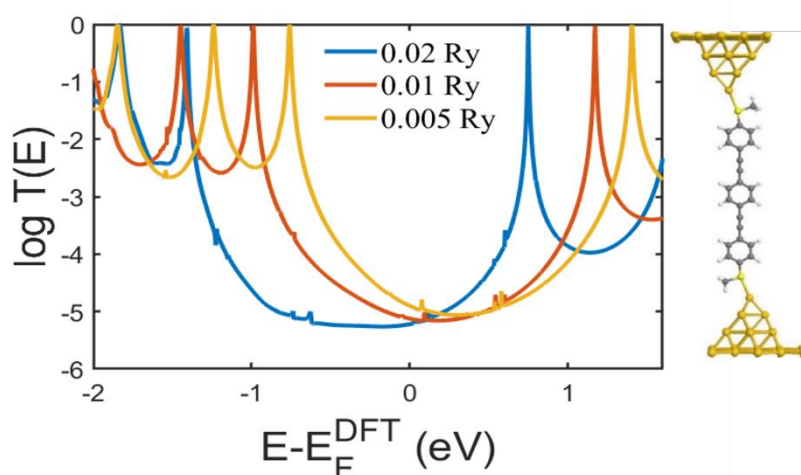| OPE-SMe	Mulliken	Hirshfeld	Voronoi
0.02 Ry	126.1	-0.085	-0.102
0.01 Ry	126.011	-0.009	-0.008
0.005 Ry	125.966	0.033	0.036

Figure (4.19): The top panel illustrates the charge distribution of OPE-SMe anchors at both sides, and the bottom panel shows its transmission behaviour with different basis sets.

4.4.6. The pinning in bipyridine molecule

For the further analysis of the bipyridine junction, we want to understand the cause of the Fermi energy pinning to the LUMO by comparing the transmission behaviour and the charge distribution between strong and weak coupling to the electrodes.

Figure (4.20) show the transmission behaviour of bipyridine with weak coupling (3Å) at the basis sets 0.02, 0.01 and 0.005 Ry. In comparison to the transmission curves in strong coupling (2.3Å) (see figure 4.13 b), we can see that the basis set behaviour becomes dependant on the

contact distance. Due to the pinning, the increase in the basis set does not have an effect on the transmission behaviour in the strong coupling case, whereas in the weak contact the resonances are shifted with having long basis sets.
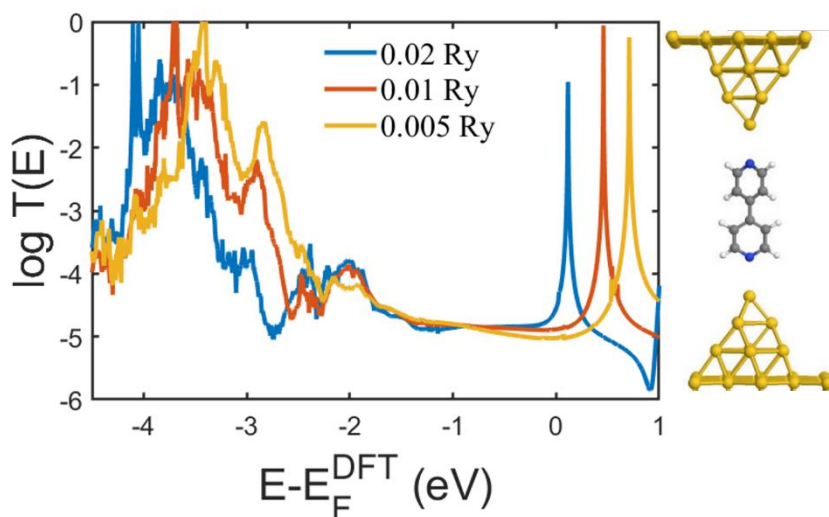

Figure (4.20): The behaviour of the transmission curves For bipyridine at different basis sets with weak contact to the electrodes (3Å). Increasing the binding distance between the gold leads and the anchor removes the pinning behaviour.

Furthermore, the behaviour of the charge distribution persists at weak coupling (table 4.21). The Hirshfeld and Voronoi populations in both coupling (strong and weak) present that the charge transfers out from the molecule into the gold (positive sign). In the weak contact, we can see that Mulliken population agrees with Hirshfeld and Voronoi and shows the same trend (donating electrons) with changing the basis sets.

Bipyridine (N-Au=3Å)	Mulliken	Hirshfeld	Voronoi
0.02 Ry	57.902	0.082	0.054
0.01 Ry	57.849	0.138	0.121
0.005 Ry	57.833	0.15	0.148

Table (4.21): The charge distribution for bipyridine (weakly coupled) at different basis sets using Mulliken, Hirshfeld and Voronoi methods.

The interesting thing between both coupling is the pinning of the E_F to the LUMO, which only occurs in strong contact between Au-N, and that might be the clue to explain the cause of the pinning in DFT. The DFT calculation always predicts this pinning of the bipyridine to the LUMO resonance, which results in a high conductance. However, based on the experimental measurements the fully-extended bipyridine molecule between the two electrodes indicates low conductance value, and the high conductance is just a result of the bipyridine binding to the electrodes with tilt angle (the pyridyl ring is lying co-facially on the gold contact) [26]–[28]. This means that in the case where Au-N bond is perpendicular to the conducting pi-system, the DFT electrode Fermi energy should be located in the middle of the HOMO-LUMO gap near the LUMO resonance to have a good agreement with the experimental result.

4.4.7. Self-Assembled Monolayers (SAMs)

In this section, I am going to use periodic gold electrodes with bipyridine and anthracene in order to test if the periodicity causes pinning to the resonance or not. There are two types of systems in SIESTA to simulate molecular electronics. The first type is called a supercell approach or non-periodic system, where we define a molecule suspended between two electrodes in a 1-dimentional unit cell. This unit cell has to be large enough, so there is no interaction to the neighbouring unit cell. This approach is what I have used so far to generate the transmission coefficient. The second type is called a self-assembled monolayers (SAMs). It assumes that the molecules are isolated on their own unit cell and repeated in 2-dimensional layer. On other words, the unit cells of the extended molecule should be calculated in 2D space. This means that the leads have to be periodic in X and Y directions, while the transport axis (Z direction) is not periodic.

Figure (4.22) illustrates the transmission curves of bipyridine using periodic and non-periodic flat leads. It can be seen, the E_F does not pin to the LUMO resonance in both cases. The shift is due to the difference of the LUMO level relative to the Fermi energy of the periodic and non-periodic gold. In contrast, the pinning behaviour occurs for both periodic and non-periodic system only in the case of adding an extra gold atom as a tip to the same leads structure (figure 4.23). The properties of the tip or under coordinated gold atom is different from the gold atom in the bulk. The under coordinated atom has a weaker bond with the neighbouring gold atom and may cause charge transfer to the molecule, leading to a shift of the LUMO in the opposite direction close to the E_F. This may not happen in the electrode flat surface, because it does not have the same ability to share electrons. The bulk surface of the gold is usually neutral, then we would expect a small charge on the N to cause a weak (or an electrostatic) interaction between the two objects (the molecule and the lead). However, the bipyridine molecule does

80

not bind to a flat surface, so the under coordinated gold atom (or the tip) is important here since it makes the molecule bind.

In terms of the anthracene on the other hand, the gold Fermi energy does not pin to the LUMO in both geometries either periodic or non-periodic. The SMe anchor here has no option to contact directly to the flat surface because of the methyl group which would hit the surface (figure 4.24).
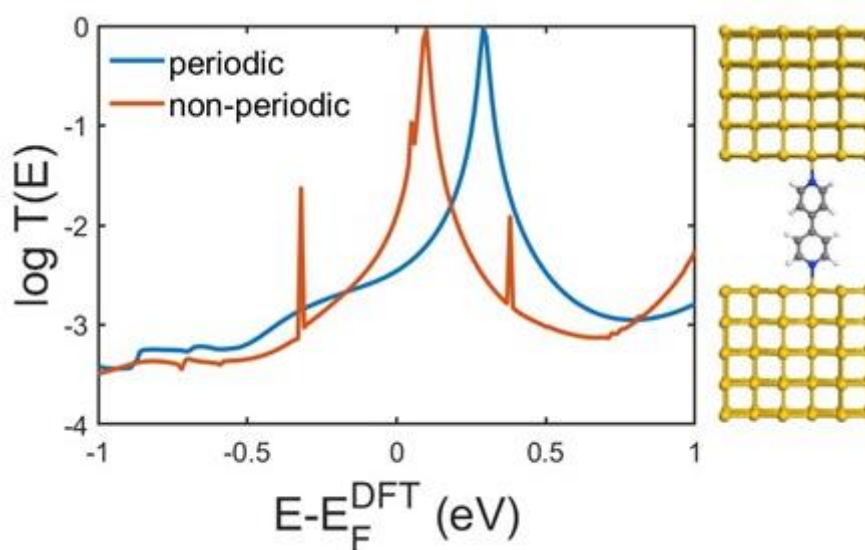

Figure (4.22): The comparison between the transmission curves of bipyridine in periodic and non-periodic system. The electrode Fermi energy (0 eV) does not pin to the LUMO resonance in both cases: periodic and non-periodic system, which may be due to the absence of the tip gold.
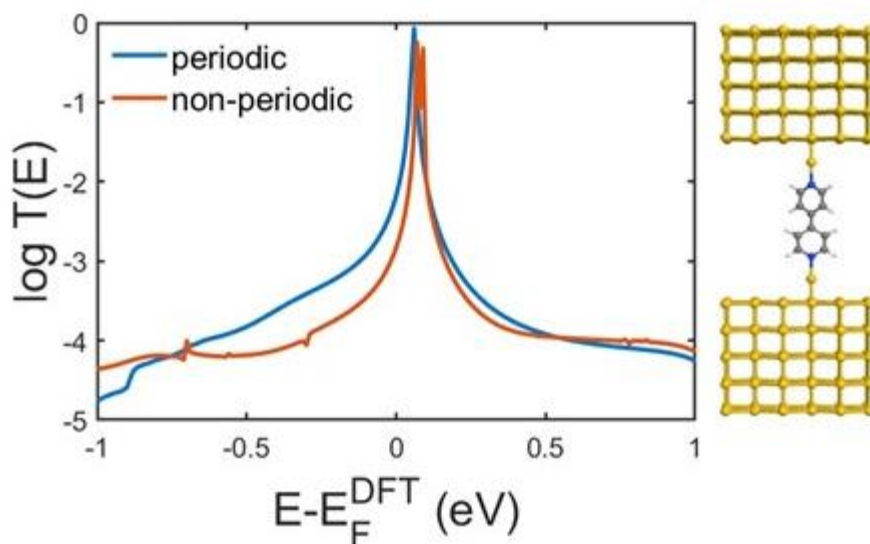
Figure (4.23): The comparison between the transmission curves of bipyridine in periodic and non-periodic system with adding a tip. It seems that the Fermi energy 0 eV does pin to the resonance in the presence of the under coordinated gold atom.
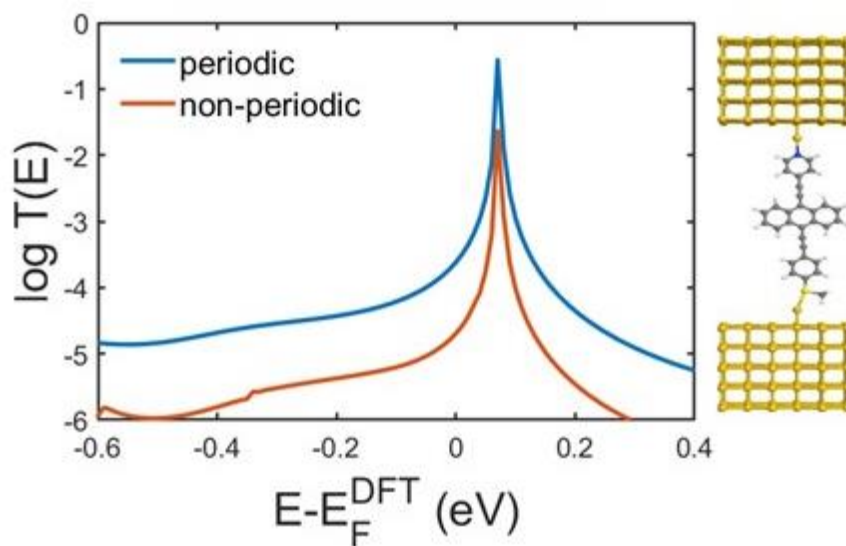

Figure (4.24): The transmission curves of anthracene in periodic and non-periodic system with adding a gold tip. SMe anchor seems to break the pinning behaviour despite the existence of the under coordinated gold atom.

4.5. Conclusion

In conclusion, this chapter has studied the impact of different anchor groups, thiol (-SH), methyl sulfide (-SMe), pyridyl (Py), (Py-SMe) and (Py-thiol), in controlling the location of the electrode Fermi energy (E_F) with respect to the relative energy levels. The results showed that molecules with thiol anchor group yields HOMO dominated transport, whilst pyridyl anchor group results in LUMO dominated transport, and the E_F in both cases sits exactly on the resonances, which does not agree with the experimental studies in the literatures. It is known that Kohn-Sham DFT eigenvalues underestimates the HOMO-LUMO gap and therefore the position of the E_F predicted by DFT is not reliable. However, the pinning behaviour is not due to DFT inherent error. In the case of thiol, the pinning of E_F to the HOMO resonance is due to the cleaved hydrogen atoms which forming a strong S-Au covalent bond. In contrast, the pinning caused by the pyridyl anchor is likely due to the presence of the tip gold. The nature of the modelling of the junction is important and plays a role for controlling the relative position of the electrode Fermi level. For example, self-assemble monolayers approach with an extra under-coordinated gold atom have indicated the pinning behaviour of the Fermi level in both periodic and non-periodic systems. In contrast, this behaviour does not occur in the absence of this add atom. I think that the under coordinated atom, which has a weaker link with the neighbouring gold atom, might produce an opposite charge transfer for the molecule, causing the LUMO to move towards the E_F. On the other hand, it is obvious that adding SMe or thiol anchors on one side of the anthracene molecule leading to remove the pinning behaviour caused by Py anchor.

Bibliography:

[1] Tour, J.M., 2003. *Molecular electronics: commercial insights, chemistry, devices, architecture and programming*. World Scientific.

[2] Ratner, M.A., 2002. Introducing molecular electronics. *Materials today*, *5*(2), pp.20-27.

[3] Tans, S.J., Devoret, M.H., Dai, H., Thess, A., Smalley, R.E., Geerligs, L.J. and Dekker, C., 1997. Individual single-wall carbon nanotubes as quantum wires. *Nature*, *386*(6624), pp.474-477.

[4] Xiao, X., Xu, B. and Tao, N.J., 2004. Measurement of single molecule conductance: Benzenedithiol and benzenedimethanethiol. *Nano letters*, *4*(2), pp.267-271.

[5] McCreery, R.L., Yan, H. and Bergren, A.J., 2013. A critical perspective on molecular electronic junctions: there is plenty of room in the middle. *Physical Chemistry Chemical Physics*, *15*(4), pp.1065-1081.

[6] Su, T.A., Neupane, M., Steigerwald, M.L., Venkataraman, L. and Nuckolls, C., 2016. Chemical principles of single-molecule electronics. *Nature Reviews Materials*, *1*(3), pp.1-15.

[7] Cui, L., Miao, R., Jiang, C., Meyhofer, E. and Reddy, P., 2017. Perspective: Thermal and thermoelectric transport in molecular junctions. *The Journal of Chemical Physics*, *146*(9), p.092201.

[8] Wang, X., Bennett, T.L., Ismael, A., Wilkinson, L.A., Hamill, J., White, A.J., Grace, I.M., Kolosov, O.V., Albrecht, T., Robinson, B.J. and Long, N.J., 2020. Scale-up of room-temperature constructive quantum interference from single molecules to self-assembled molecular-electronic films. *Journal of the American Chemical Society*, *142*(19), pp.8555-8560.

[9] Ismael, A., Wang, X., Bennett, T.L., Wilkinson, L.A., Robinson, B.J., Long, N.J., Cohen, L.F. and Lambert, C.J., 2020. Tuning the thermoelectrical properties of anthracene-based self-assembled monolayers. *Chemical science*, *11*(26), pp.6836-6841.

[10] Alshammari, M., Al-Jobory, A.A., Alotaibi, T., Lambert, C.J. and Ismael, A., 2022. Orientational control of molecular scale thermoelectricity. *Nanoscale Advances*, *4*(21), pp.4635-4638.

[11]   Perdew, J.P., Burke, K. and Ernzerhof, M., 1996. Generalized gradient approximation made simple. *Physical review letters*, *77*(18), p.3865.

[12]   Soler, J.M., Artacho, E., Gale, J.D., García, A., Junquera, J., Ordejón, P. and Sánchez-Portal, D., 2002. The SIESTA method for ab initio order-N materials simulation. *Journal of Physics: Condensed Matter*, *14*(11), p.2745.

[13]   Troullier, N. and Martins, J.L., 1991. Efficient pseudopotentials for plane-wave calculations. *Physical review B*, *43*(3), p.1993.

[14]   Boese, A.D., Jansen, G., Torheyden, M., Höfener, S. and Klopper, W., 2011. Effects of counterpoise correction and basis set extrapolation on the MP2 geometries of hydrogen bonded dimers of ammonia, water, and hydrogen fluoride. *Physical Chemistry Chemical Physics*, *13*(3), pp.1230-1238.

[15]   Boys, S.F. and Bernardi, F.J.M.P., 1970. The calculation of small molecular interactions by the differences of separate total energies. Some procedures with reduced errors. *Molecular Physics*, *19*(4), pp.553-566.

[16]   Ferrer, J., Lambert, C.J., García-Suárez, V.M., Manrique, D.Z., Visontai, D., Oroszlany, L., Rodríguez-Ferradás, R., Grace, I., Bailey, S.W.D., Gillemot, K. and Sadeghi, H., 2014. GOLLUM: a next-generation simulation tool for electron, thermal and spin transport. *New Journal of Physics*, *16*(9), p.093029.

[17]   Ismael, A.K. and Lambert, C.J., 2019. Single-molecule conductance oscillations in alkane rings. *Journal of Materials Chemistry C*, *7*(22), pp.6578-6581.

[18]   Alshehab, A. and Ismael, A.K., 2023. Impact of the terminal end-group on the electrical conductance in alkane linear chains. *RSC advances*, *13*(9), pp.5869-5873.

[19]   Ismael, A., Al-Jobory, A., Wang, X., Alshehab, A., Almutlg, A., Alshammari, M., Grace, I., Benett, T.L., Wilkinson, L.A., Robinson, B.J. and Long, N.J., 2020. Molecular-scale thermoelectricity: as simple as 'ABC'. *Nanoscale Advances*, *2*(11), pp.5329-5334.

[20]   Cui, L., Miao, R., Jiang, C., Meyhofer, E. and Reddy, P., 2017. Perspective: Thermal and thermoelectric transport in molecular junctions. *The Journal of Chemical Physics*, *146*(9), p.092201.

[21]   Ismael, A.K. and Lambert, C.J., 2020. Molecular-scale thermoelectricity: a worst-case scenario. *Nanoscale Horizons*, *5*(7), pp.1073-1080.

[22]   Mulliken, R.S., 1955. Electronic population analysis on LCAO–MO molecular wave functions. I. *The Journal of Chemical Physics*, *23*(10), pp.1833-1840.

[23]   Hirshfeld, F.L., 1977. Bonded-atom fragments for describing molecular charge densities. *Theoretica chimica acta*, *44*(2), pp.129-138.

[24]   Fonseca Guerra, C., Handgraaf, J.W., Baerends, E.J. and Bickelhaupt, F.M., 2004. Voronoi deformation density (VDD) charges: Assessment of the Mulliken, Bader, Hirshfeld, Weinhold, and VDD methods for charge analysis. *Journal of computational chemistry*, *25*(2), pp.189-210.

[25]   Häkkinen, H., 2012. The gold–sulfur interface at the nanoscale. *Nature chemistry*, *4*(6), pp.443-455.

[26]   Quek, S.Y., Kamenetska, M., Steigerwald, M.L., Choi, H.J., Louie, S.G., Hybertsen, M.S., Neaton, J.B. and Venkataraman, L., 2009. Mechanically controlled binary conductance switching of a single-molecule junction. *Nature nanotechnology*, *4*(4), pp.230-234.

[27]   Refaely-Abramson, S., Liu, Z.F., Bruneval, F. and Neaton, J.B., 2019. First-principles approach to the conductance of covalently bound molecular junctions. *The Journal of Physical Chemistry C*, *123*(11), pp.6379-6387.

[28]   Vavrek, F., Butsyk, O., Kolivoška, V., Lachmanová, Š.N., Sebechlebská, T., Šebera, J., Gasior, J., Mészáros, G. and Hromadová, M., 2021. Does the Seebeck coefficient of a single-molecule junction depend on the junction configuration?. *Journal of Materials Chemistry A*, *9*(32), pp.17512-17520.

Chapter 5

The effect of vibrations on the Seebeck coefficient in molecular junctions

5.1. Introduction

Identification of techniques for controlling the thermopower (Seebeck coefficient) of single molecules is an essential step in developing extremely efficient thin-film thermoelectric materials [1]–[5]. Quantum interference (QI) phenomena is a key factor in determining electron transport across single molecules [6], [7], and it can be found in para- and meta-connected molecules, where constructive (CQI) and destructive quantum interference (DQI) occur [8]. The constructive (destructive) QI results in a low (high) thermoelectrical properties. This is attributed to the anti-resonance, a distinct feature of destructive interference, which can enhance the Seebeck coefficient [9]. Since the thermopower (S) is strongly affected by QI, the ability to control QI in single molecules is of fundamental interest in providing new techniques for improving the performance of molecular-scale devices [10], [11]. Towards this goal, previous work [1] investigated the sensitivity of quantum interference (QI) to the nature of bridged biphenyl molecules with para and meta connectivities to pyridyl anchor groups, and the experimental data within a tight-binding model has shown that QI phenomena in bridged biphenyl derivatives and associated meta molecular connectivity can be exploited to improve thermoelectric performance in molecular junctions. However, since the previous DFT based theoretical model could not explain the trends of the Seebeck coefficient in experimental measurements, this suggests that other properties not included in the model could be

87

responsible. By looking at that set of molecules [1], the only difference apart from the connectivity is the bridging atoms, some of which possess pendant groups. This has opened the door to explore the effect of pendant groups on quantum interference. The motivation in this present work is to investigate the vibrational effect of the side groups which could be playing a role in terms of QI. The idea is that the thermopower S can be controlled by the pendant groups attached to the centre core of fluorene-based molecules, and the amount they vibrate can enhance or decrease the Seebeck coefficient. Therefore, I model four molecules, the design of which were proposed by Gunnar Olsen of Durham University who synthesized the series of molecule in the previous study [1]. The backbone of these molecules is the same to that ones in the previous study [1], with connected large side groups to the bridging atom (figure 5.1), and again there is a para and meta connected for the two different pendant groups. The difference between C≡C and C≡N bonds is the dipole moment in the C≡N due to the opposite charges between carbon and nitrogen atom, which might influence the vibrations.

5.2. Molecular Structures

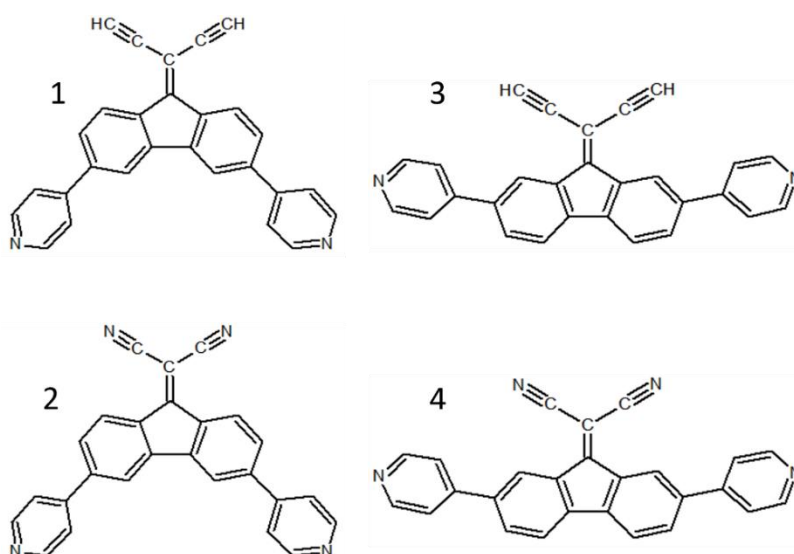**Figure (5.1):** Structures of the molecules discussed in this work, where the molecular design

consists of C≡C and C≡N side groups connected to fluorene-biphenyl unit with meta (1),

(2) and para (3), (4) connectivities to pyridyl anchor groups.

5.3. Theoretical Method

The density functional code SIESTA [12], [13] was used to compute the optimum geometry of each of the isolated molecules (figure 5.1). The process is described in chapter 4, but here I used a double-zeta (DZ) basis set for all atoms with the LDA-CA approximation [14], [15] to describe the exchange correlation functional. The dihedral angle between the two hexagonal rings is determined to be at 30°, as shown in figure (5.2), and the method to calculate this angle is mentioned in chapter 4. After completing the molecules relaxation process, the binding energy is calculated, figures (5.3 and 5.4). This calculation has been done using the counterpoise method (CP) [16], [17], which discussed in detail in chapter 2 (section 2.6.2). The optimum separation distance of the pyridyl anchor group in para connectivity is found to equal $d = 2.2\text{Å}$ with a binding energy of about $-0.86\ eV$, whereas in meta connectivity the optimum separation distance of the same anchor is determined to be $d = 2.7\text{Å}$, at approximately $-0.175\ eV$. The molecules were then placed between (111) gold electrodes which is modelled with pyramid tips linked to 5 layers each containing 25 atoms to compute the transmission coefficient $T(E)$ and the Seebeck coefficient S using the quantum transport code Gollum [18].
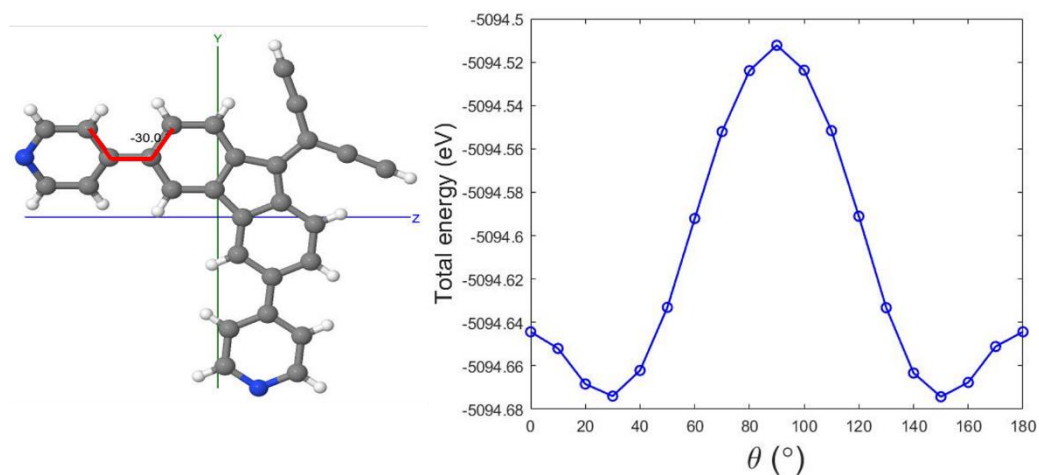
Figure (5.2): Left panel shows the torsion angle (red line) between the two hexagonal rings. Right panel illustrates the ground state energy curve for each torsion angle of the phenylpyridyl anchor group, and the optimum angle is determined to be at $30°$.
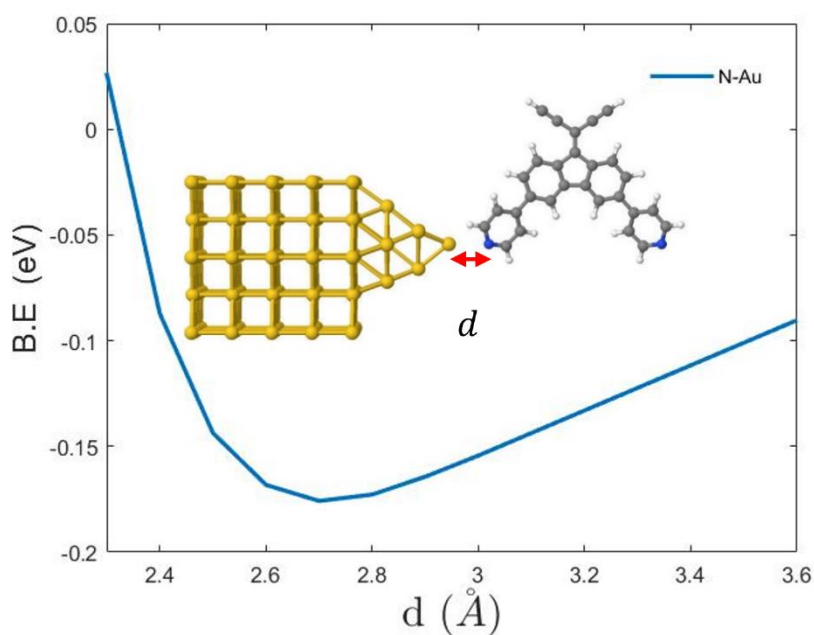

Figure (5.3): Binding energy versus distance plot of meta-connected molecule 1, where the optimum ground state energy is determined at distance $d = 2.7 Å$.
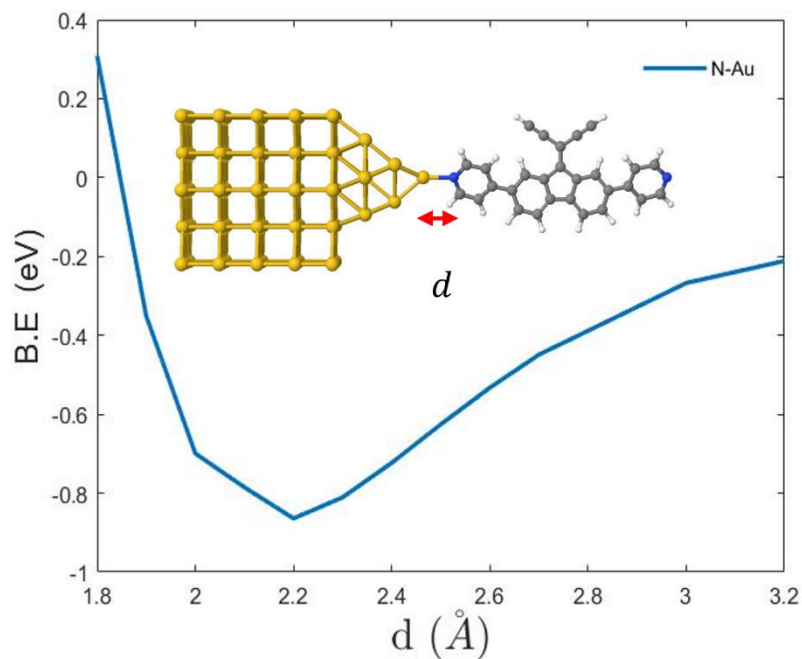
Figure (5.4): Binding energy versus distance plot of para-connected molecule 3, where the optimum ground state energy is determined at distance $d = 2.2$Å.

5.4. Results and Discussion

5.4.1. Varying the side groups

The DFT calculation of the optimum configurations (i.e. before vibrating the pendant groups) demonstrates quantum interference (QI) effects, including DQI in the meta-connected molecules (1 and 2) and CQI in the molecules of para connectivity (3 and 4) (see figures 5.5 and 5.6). This disagrees in comparison to the DFT result of the previous study [1], where none of the bridging atoms that possess pendant group such as CH_2 and CMe_2 group showed DQI features. Moreover, the tight-binding model of the meta case proved that the system with no bridging atom produces DQI, which turns to CQI when the system has a bridging atom [1].

This suggests that the introduced tight-binding model [1] is no longer valid, because it does not reproduce what is happening here for these new set of molecules.

Here, the aim again is to investigate the sensitivity of quantum interference (QI) to the vibrational effect of these new pendant groups, and then explore how these fluctuations would impact the Seebeck coefficient. The process in this present work was started by varying the bond length of the C≡C and C≡N bonds in the side groups attached to the molecules in figure (5.1), and then computing the transmission and Seebeck coefficients for each configuration. The C≡C and C≡N bonds have been compressed and stretched in a series of equal lengths starting from 0.9Å to 1.7Å, while the rest of the molecule is fixed. The results of the transport calculations in the meta case (compounds 1 and 2) show that the HOMO levels are moving upwards in energy with the anti-resonances into the gap with increasing the length of the triple bonds, while the LUMO resonances are pinned near the Fermi energy of the gold electrode due to the contact to the pyridyl anchor group, leading to a reduced HOMO-LUMO gap (figure 5.7). In the para case (compounds 3 and 4) similar behaviour is occurring; the HOMO resonances are slightly shifted with the Fano line shape, which appear clearly in the mid gap with increasing the stretch of both side groups (figure 5.8).

By looking at the Seebeck calculations (figures 5.7 and 5.8) of both meta and para connectivities, the change in the meta is shown to be much larger than in the para due to the presence of the sharp transmission dip at the centre of the HOMO-LUMO gap. To show this more clearly, I evaluated the Seebeck coefficient at the Fermi energy $E = -0.25\,eV$ as a function of the pendant groups variation (d) (figure 5.9). The bond length is varied between 0.9 and 1.9Å with size step equals to 0.1Å. As can be seen, there is a definite trend for the Seebeck in the meta-connected molecules (red line) to decrease by a significant amount compared to the Seebeck in the para-connected molecules (blue line). As long as the para case has no anti-resonance feature, the Seebeck value remains fairly constant until a resonance comes close to

the chosen Fermi energy. The Fano resonance [19], [20] is important if it happens to be close to the electrode Fermi level, which can enhance the results, but here in our case it does not play a role for enhancing the Seebeck coefficient. In summary, the Seebeck coefficient of meta-linked molecules is sensitive to the change of the bond length in the connected side groups, whereas the sensitivity in the para case is much weaker. Consequently, the vibrational effect in the meta shows more enhancement in the Seebeck in comparison to the para case (figure 5.9).
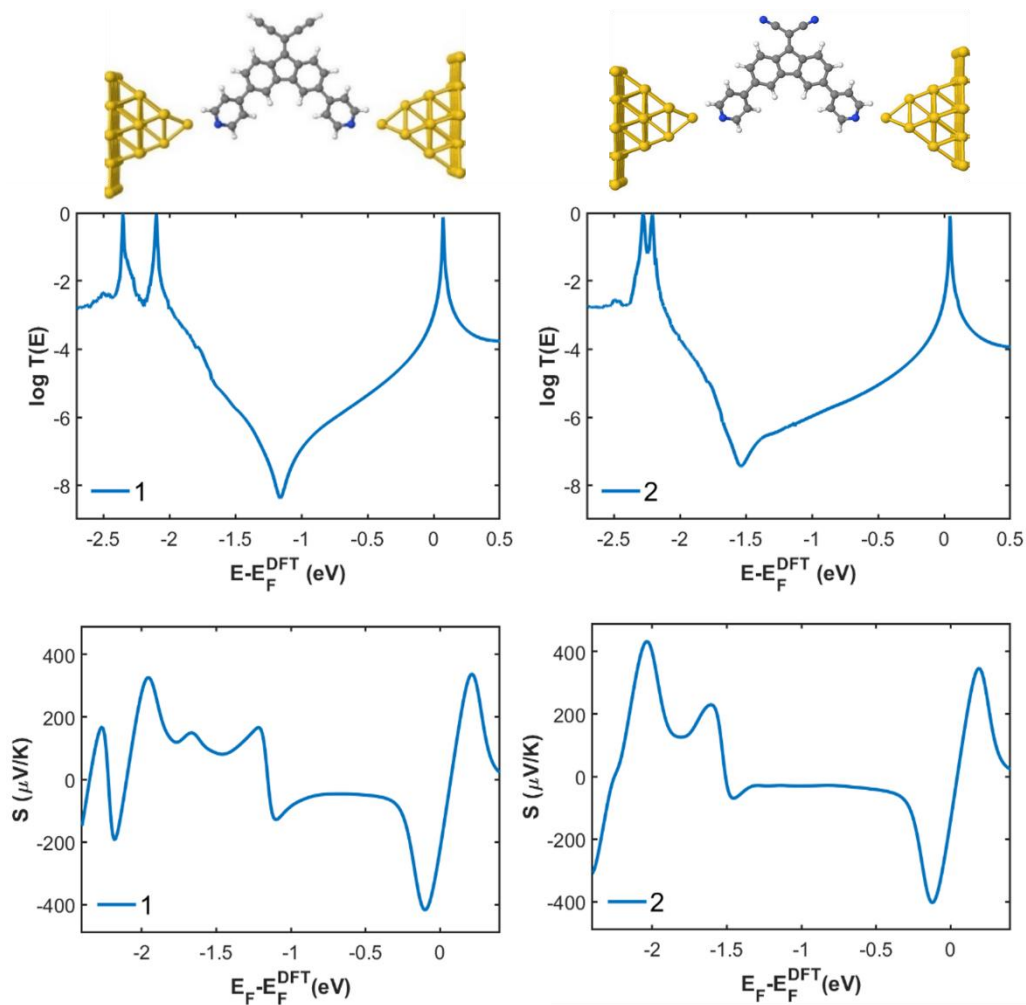
Figure (5.5): The first and second columns illustrate the transmission and Seebeck coefficients of the meta molecules (1and 2), where we have destructive quantum interference feature DQI. The position of the electrode Fermi energy $E_F = 0eV$ sits near the LUMO resonance due to the contact to the pyridyl anchor group.
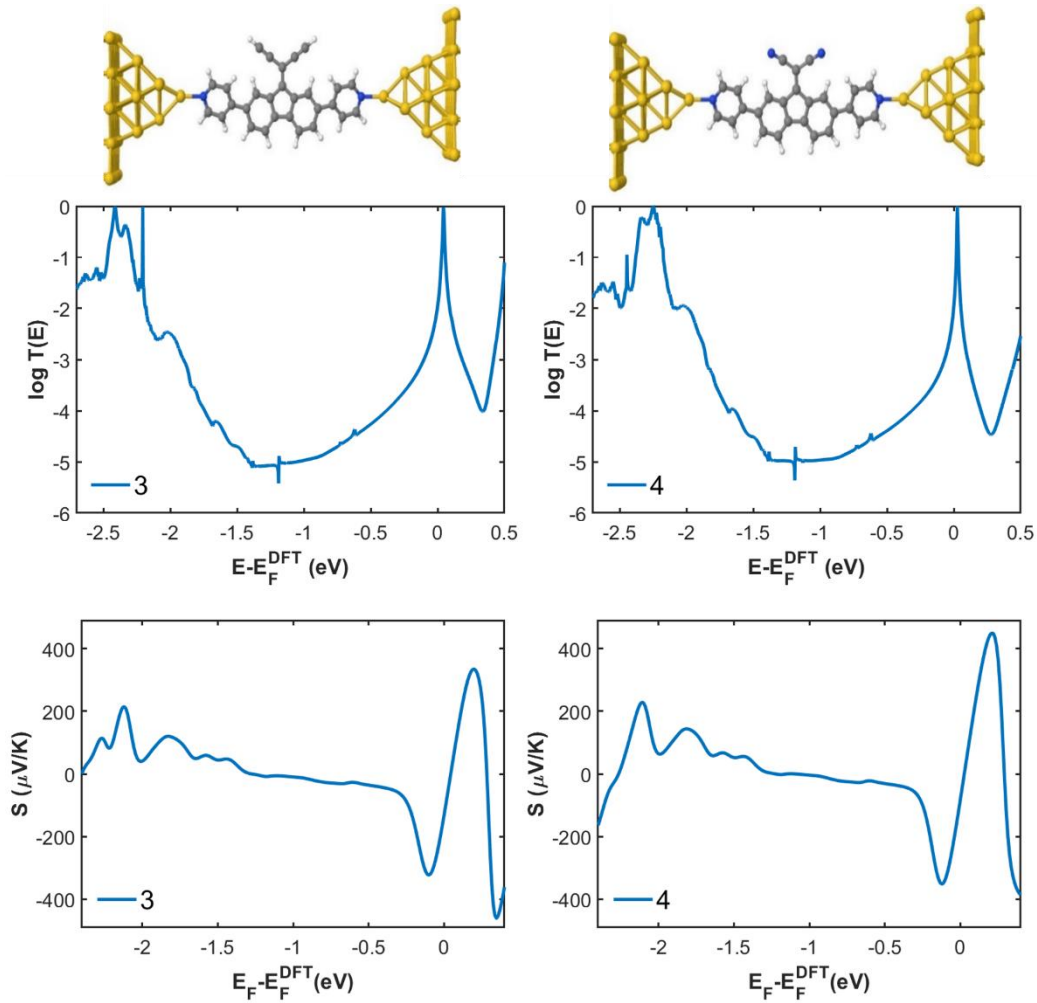
Figure (5.6): The first and second columns illustrate the transmission and the Seebeck coefficients of the para case (3 and 4) with constructive quantum interference feature CQI. The position of the electrode Fermi energy $E_F = 0eV$ locates near the LUMO resonance due to the contact to the pyridyl anchor group. The small resonance in the middle of the HOMO-LUMO gap of the transmission curves (between -1 and -1.5 eV) is the Fano resonance.
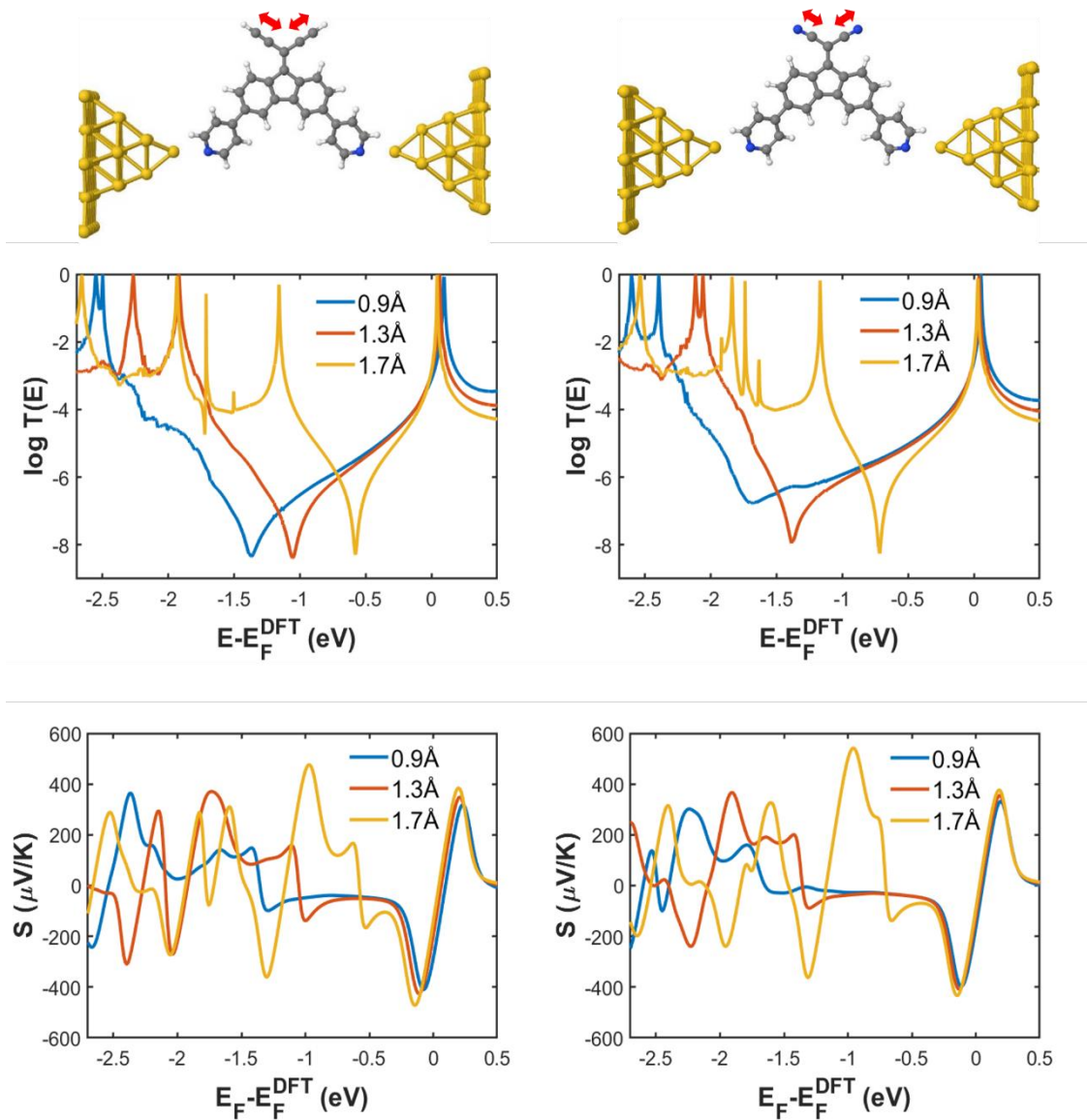
Figure (5.7): The first and second columns show the shift of the transmission and the Seebeck curves in the meta case when the C≡C and C≡N bonds of the pendant groups are varied between 0.9Å and 1.7Å. It can be seen that the shift of the HOMO resonance increases with increasing the triple bond length of the side group.
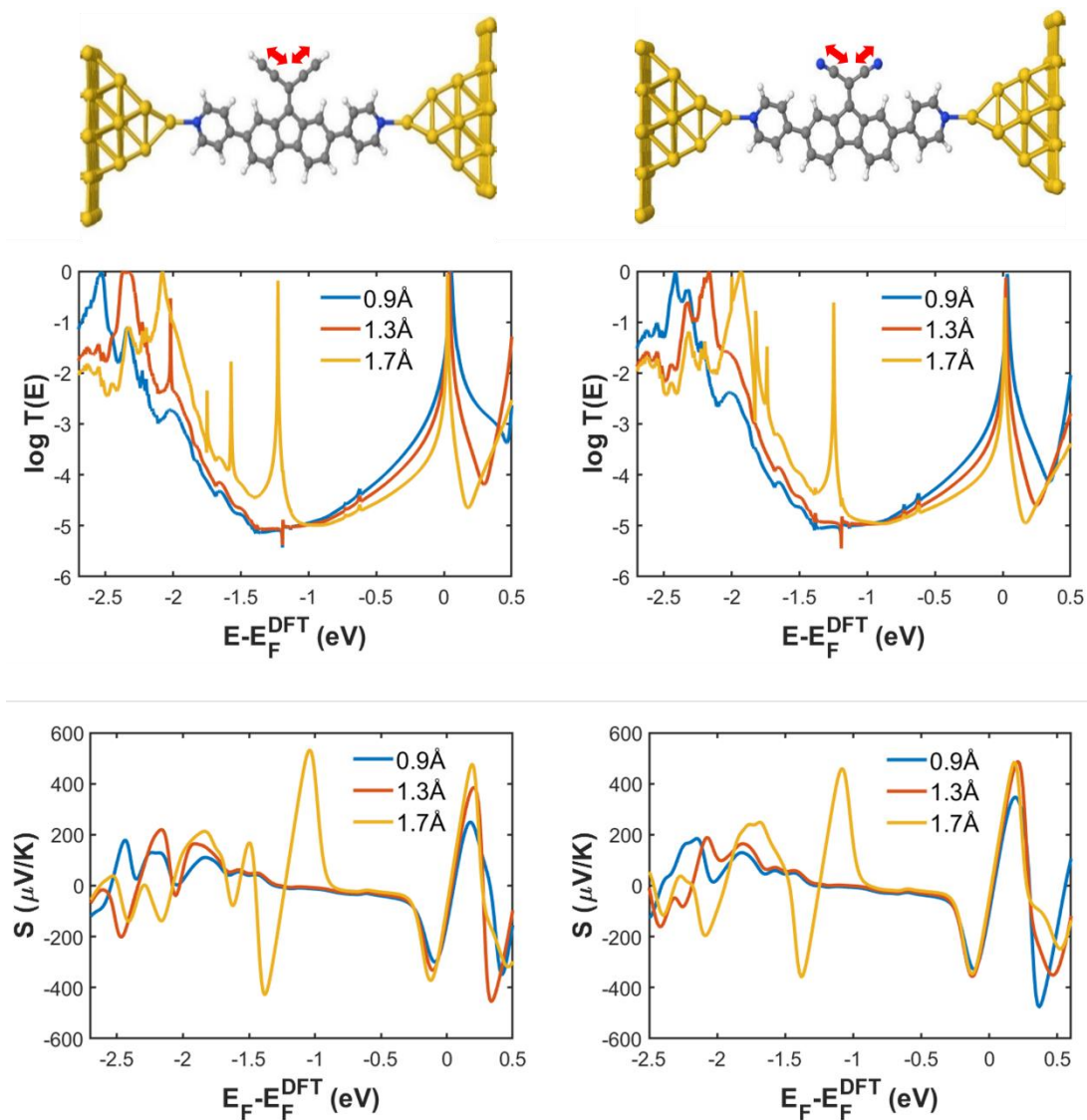
Figure (5.8): The first and second columns show the shift of the transmission and the Seebeck curves in the para case when the C≡C and C≡N bonds of the pendant groups are varied between 0.9Å and 1.7Å. It can be seen that the shift of the HOMO resonance does not increase with increasing the triple bond length of the side group compared to the meta connectivity. The Fano line shape near the HOMO resonance does not enhance the Seebeck because it happens away from the electrode Fermi energy 0eV.
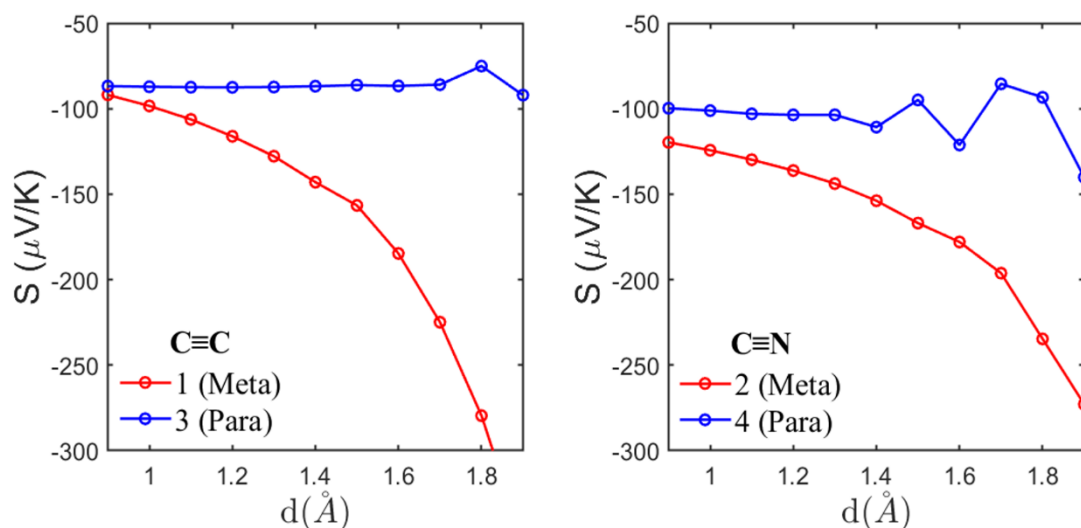
Figure (5.9): The Seebeck values at $E = -0.25 \, eV$ as a function of changing the bond length (d) of C≡C and C≡N from d= 0.9 Å to 1.9 Å in both para and meta case. The meta connectivity shows more sensitivity to the vibrations of the triple bonds compared to the para connectivity.

5.4.2. Tight-binding Model

As mentioned above, these molecules do not behave like the previous studied molecules [1], and therefore, I need to reveal the evolution of transport properties with varying the pendant groups via their tight-binding models. This process is divided into several steps. The first, is to examine the optimum configration (figure 5.10 a) and understand the effect of side groups on QI. Hence, I constructed a tight-binding representation with similar core structure, where each site has an energy $\varepsilon_0 = 0$ with coupling $\gamma = -1$. The second step is to simulate the variation of the bond length used in the DFT based calculations, and this is achieved by changing the bond α (green line) between the end atoms of the side group to three different lengths (0.9,

1.2, 1.7) (figure 5.10 b). Finally, the end atoms in the pendant group (orange colour) are set to have different energy level $\varepsilon_b = 0.7$ to mimic the C≡N bond in the DFT (figure 5.10 c).

In the case of (a), the para connectivity results in CQI with a Fano resonance in the HOMO-LUMO gap, whereas the meta connection pattern leads to DQI, which occurs at the centre of the HOMO-LUMO gap (i.e. E = 0). This means the results of (a) agree with the results from the DFT calculation shown in figures (5.7) and (5.8). It is noticeable that the Fano line shape appears in the para case, and this attributed to the interaction between the continuum state (the molecule backbone) and the discrete state (the pendant group) [11], [21]. In the DFT calculation, the Fano resonance is likely to be the small peak near the HOMO resonance, because when the length of those bonds (C≡C and C≡N) is stretched, this small resonance starts to shift into the gab and becomes more prominent (figure 5.8). Ultimately in the cases of (b and c), changing the length of the bond α (green line) leads to shift the resonances in both para and meta transmissions (figure 5.11), which agrees with the transmission behaviour in the DFT calculation (figures 5.7 and 5.8).

From the tight binding transmission curves, I can also examine the Seebeck behaviour. Since the transmission curve in the para case is almost flat across most of the HOMO-LUMO gap, and there is not a large change in the gradient with changing the coupling strength α, I would expect a low Seebeck coefficient. On the other hand, for the meta case, the anti-resonance (which has a large gradient) would produce a large Seebeck coefficient, as illustrated in figure 5.12 which shows similar trends to the DFT results in figure (5.9).
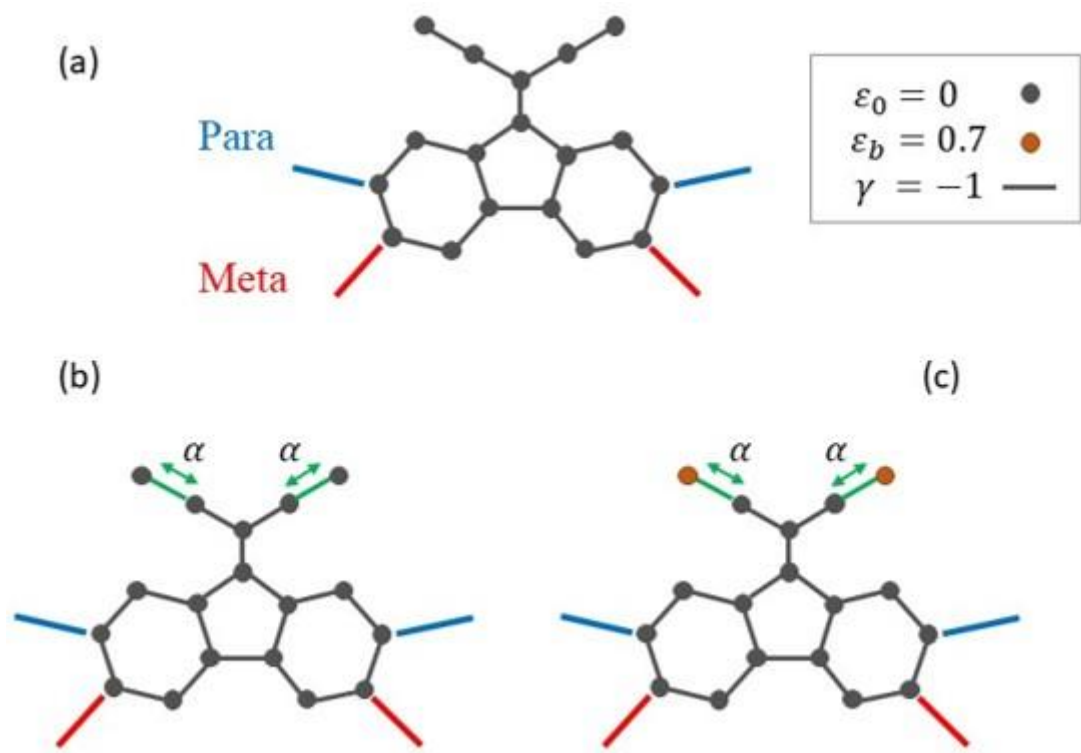
Figure (5.10): Tight binding model of a fluorene-biphenyl unit with a 1-dimensional side group. (a) All nearest neighbour bonds between atoms are equal to $\gamma = -1$, and all site energies ε_0 are zero. (b) as for (a), but the bond α is set to three different values (0.9, 1.2 and 1.7). (c) as for (b), but the orange atoms in the side group have site energy $\varepsilon_b = 0.7$.
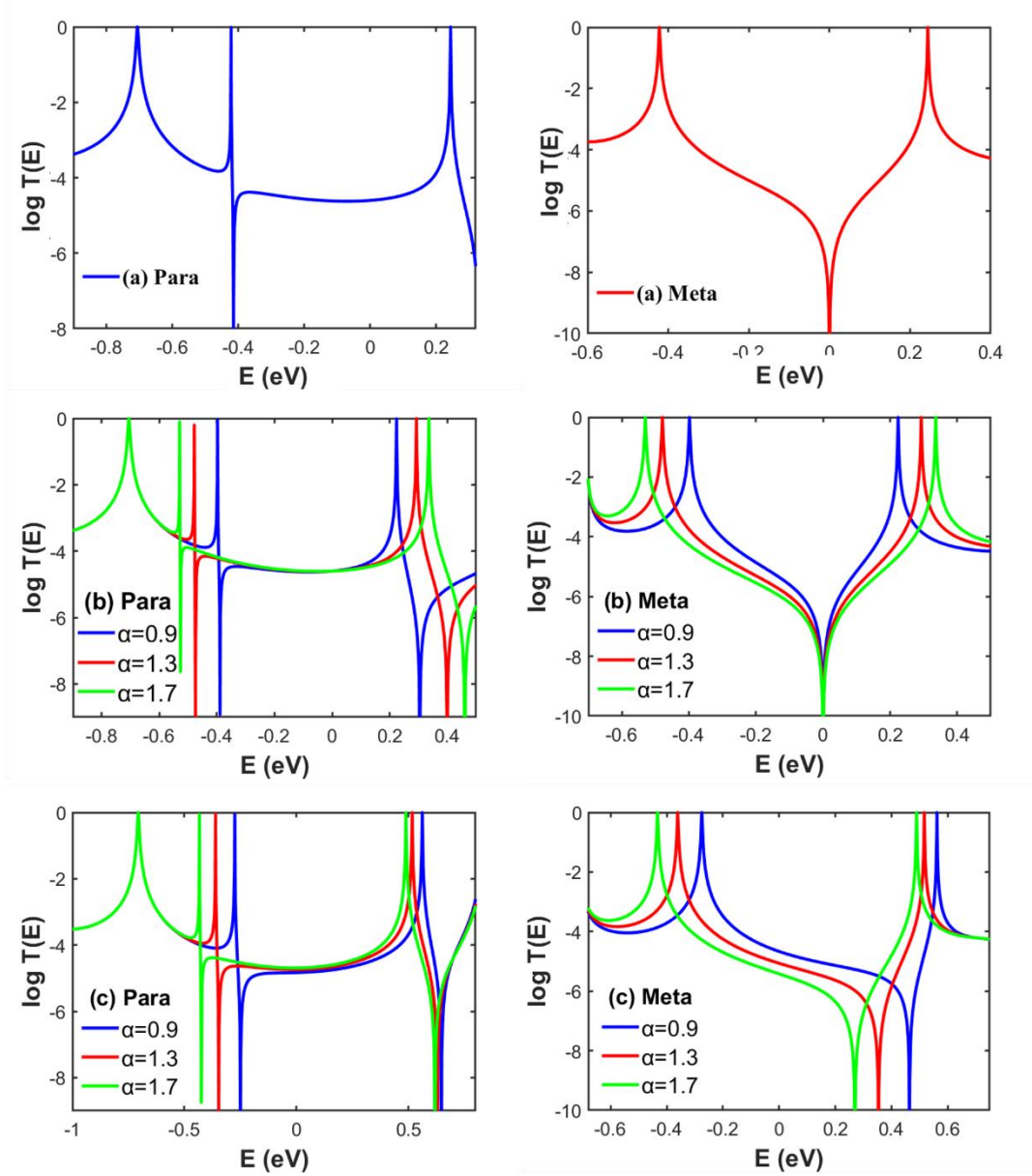
Figure (5.11): (a) Constructive and destructive QI in para and meta connection patterns, respectively, with the presence of the Fano-resonance in the para case. (b) and (c) show the shift of the resonances due to changing the bond α from 0.9 to 1.7. The difference between (b) and (c) is that in (b) all site energies ε_0 are zero, while in (c) the side group has a site energy $\varepsilon_b = 0.7$ as shown in figure (5.10), and this shifts the anti-resonance away from 0 eV.
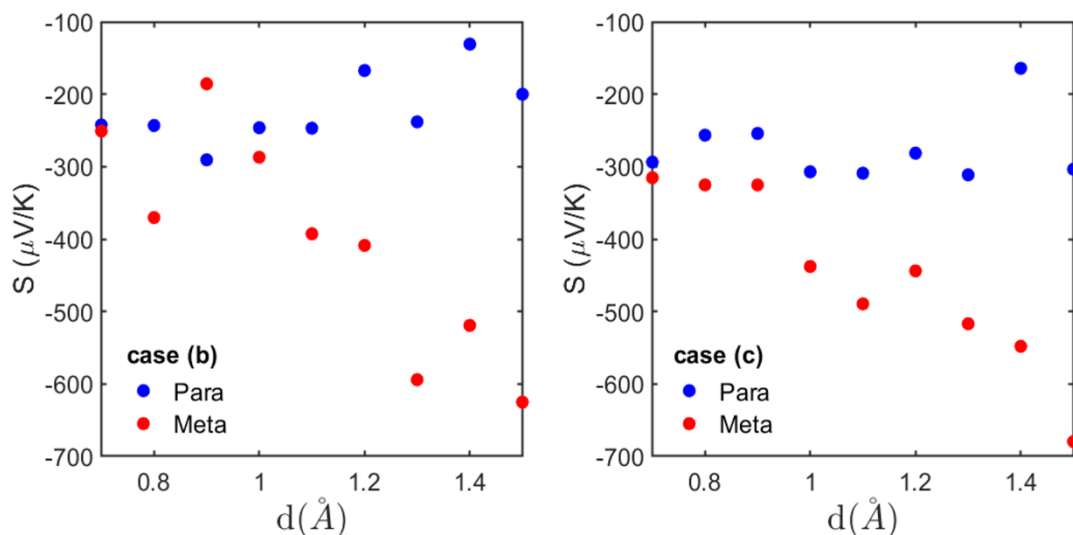
Figure (5.12): Case b and c show the evaluated Seebeck at $E = -0.25\ eV$ as a function of changing the bond length α from 0.7 to 1.5. In case (b) all site energies ε_0 are zero to mimic the C≡C, while in case (c) the side group has a site energy $\varepsilon_b = 0.7$ to mimic the C≡N. Both cases show similar trends to the DFT calculations where the Seebeck behaviour in the meta case enhances more with the vibrations of the bond α compared to the para connectivity.

5.4.3. Molecular Dynamics Simulations (MD)

The conclusion of the DFT calculations at zero temperature illustrates that the value of the Seebeck is very strongly dependant on the fluctuation of the side groups with the meta position rather than the para case. This would beg the questions: if we carry out a realistic fluctuation of those pendant groups will that produce a large effect, and to what extent the C≡C and C≡N bonds can be stretched at room temperature? To address these questions, I applied the molecular dynamics simulation [22], [23] within SIESTA for only meta-connected compounds. This simulation tool is dealing with solving Newton equations to study the physical behaviour and interactions of atoms and molecules over a set period of time, providing insight into the

101

system's dynamical evolution [24]. The type of this run in SIESTA is called nose, where I carried out 5000-time steps with an initial temperature to the system ($270\,K$), target temperature ($300\,K$), and 1.0 fs is the length of the time step. It is important to consider that adding the whole gold leads to the molecules in the MD simulation is computationally expensive, and therefore, only the fixed gold pyramid tips were attached to them. Then, the remaining layers of the electrodes were built to compute the transmission $T(E)$ and the Seebeck S coefficients using the quantum transport code Gollum [18].
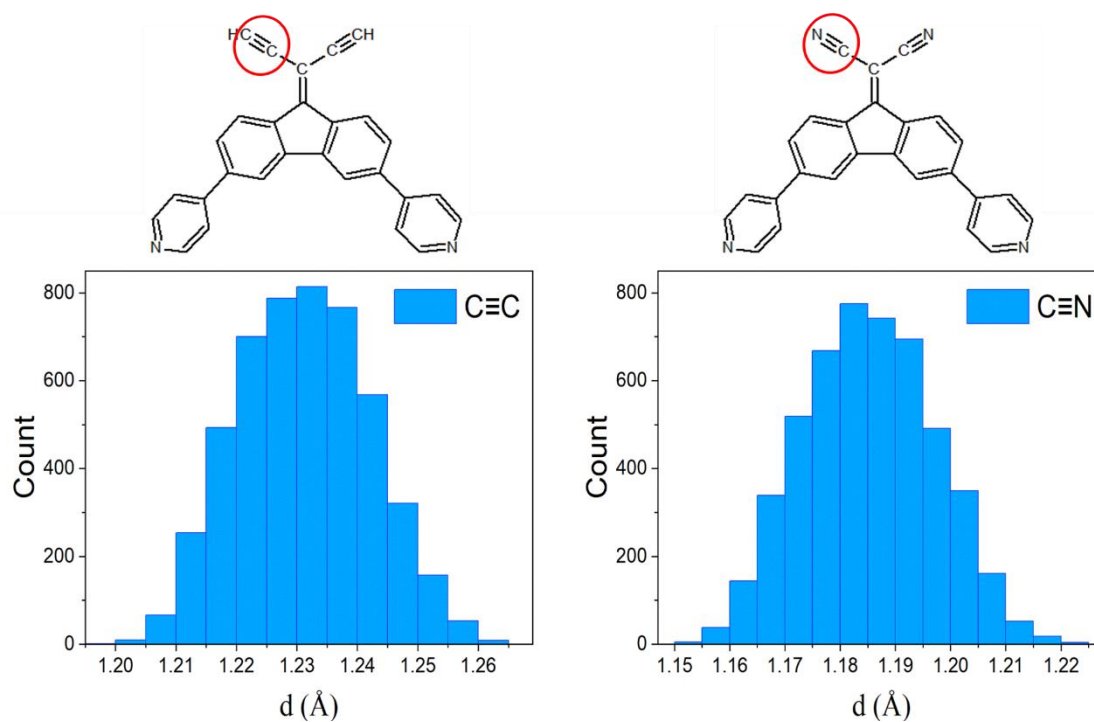

Figure (5.13): A histogram plot shows the frequencies of the C≡C bond (left histogram) and the C≡N bond (right histogram) obtained from 5000 geometries using MD simulations with 300K. The C≡C is stretched between 1.20 Å and 1.26 Å, while the C≡N vibrates between 1.15 Å and 1.22 Å.

The data of the histograms in figure (5.13) shows the frequencies of the triple bond (C≡C and C≡N) at room temperature, which are calculated from 5000 geometries of the meta compounds. The width of both histograms indicates the range of the bond stretching. For example, the C≡C is stretched between 1.20 Å and 1.26 Å, while the C≡N vibrates between 1.15 Å and 1.22 Å. The highest peak of the histograms represents the most probable value of the data set.

If I relate the information in figure 5.13, which is obtained from the MD simulations to the simple picture of the energy curve at zero Kelvin (figure 5.14), where the molecules are in their optimum configurations, and the ground state energy is calculated for different bond lengths of the triple bonds, we can find that both triple bonds behave similarly whether at 0K or 300K. The range of bond stretching accessible at room temperature agrees with that at zero temperature. Moreover, the most probable values in the histograms (the highest peaks) agree with both optimum lengths of the triple bonds at 0 eV. This correlation between optimum calculation and MD simulations proves that the behaviour of those triple bonds at room temperature follow the prediction of what we expect from the simple calculation at 0K, and this makes the calculation from the MD simulation more reliable.
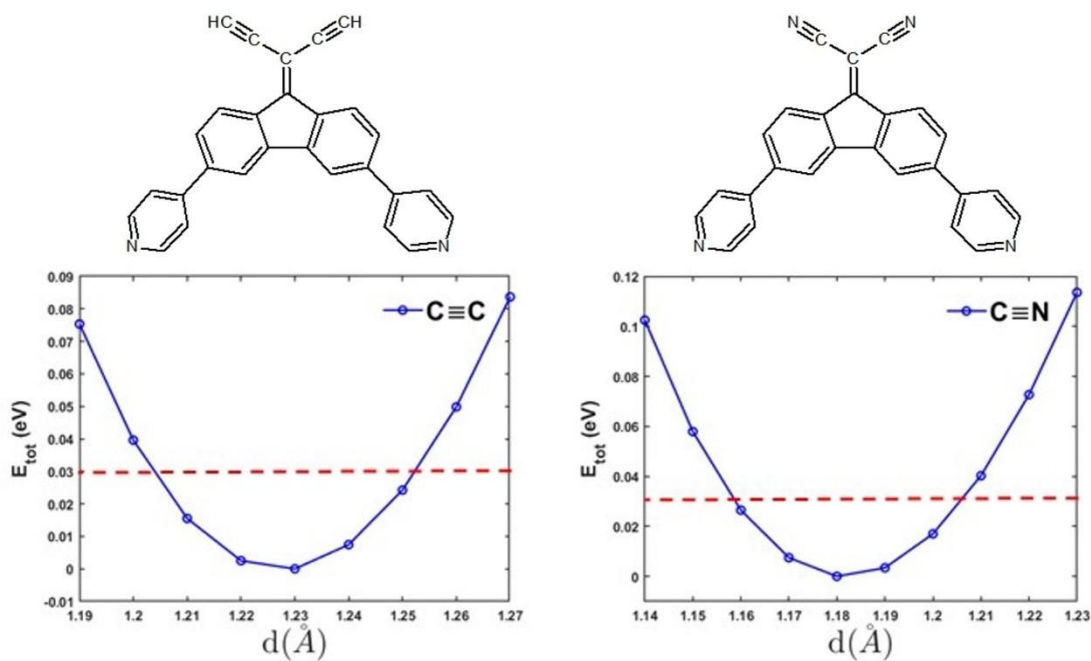
Figure (5.14): The ground state energy for the meta connected molecules as a function of the bond length d (C≡C left panel and C≡N right panel). The red dashed line is the thermal energy $k_B T$, which is the energy available for the system at room temperature. The stretching limit of the triple bonds in both calculations (0K and 300 K) agree with each other.

Bond	Min. d(Å)	Max. d(Å)	Difference
C≡C	1.20	1.26	0.06
C≡N	1.15	1.22	0.07

Table (5.15): This data is obtained from the two histograms in figure (5.12). It indicates the minimum and maximum C≡C and C≡N bonds at room temperature and the difference between them.

104

The difference between maximum and minimum lengths for these bonds at room temperature is very small around 0.01 Å, as shown in table (5.15). The fluctuation of these pendant groups is pretty much identical due to the similarity between them as both are 1-dimensional triple bonds. As a result of this, there is not a large shift in the position of their anti-resonance, and hence, there is no big change in the Seebeck curves (figure 5.16). These pendant groups were rather similar and simple, so this suggests studying a more complex side group, which could produce a greater effect. Therefore, I investigated a pendant group that has a larger charge distribution, pentafluorobenzene $C_{13}(F_5)_2$ (compound 5, figure 5.17), and compared its transport behaviour with the series of molecules. It is expected that the fluctuation of the charge of 10 fluorine atoms may produce an electrostatic effect on the energy levels of the molecule, resulting in a larger shift of the transmission curve.

The MD simulation provided a series of snapshots of the studied systems, which include bond stretching as well as twisting of the molecules. For each snapshot, I computed the transmission and the Seebeck coefficients. Figure (5.17) demonstrates a set of 213 transmission and Seebeck curves plotted from 5000 geometries in the MD simulation for molecules 1, 2 and 5 (each curve has a time step interval of 1.0fs). These transport calculations reveal that the spread of the HOMOs and their anti-resonances into the gap in Fluorobenzene case is a quite large compared to the other two pendant groups (compounds 1 and 2). By looking at the transmissions behaviour of these three molecules, the anti-resonance feature at the gap centre has been maintained in both molecules whose C≡C and Fluorobenzene side groups, whereas most of the transmission curves in the case of C≡N pendant have a parallel shape, which means the anti-resonance starts to alleviate in most of the transmission curves.
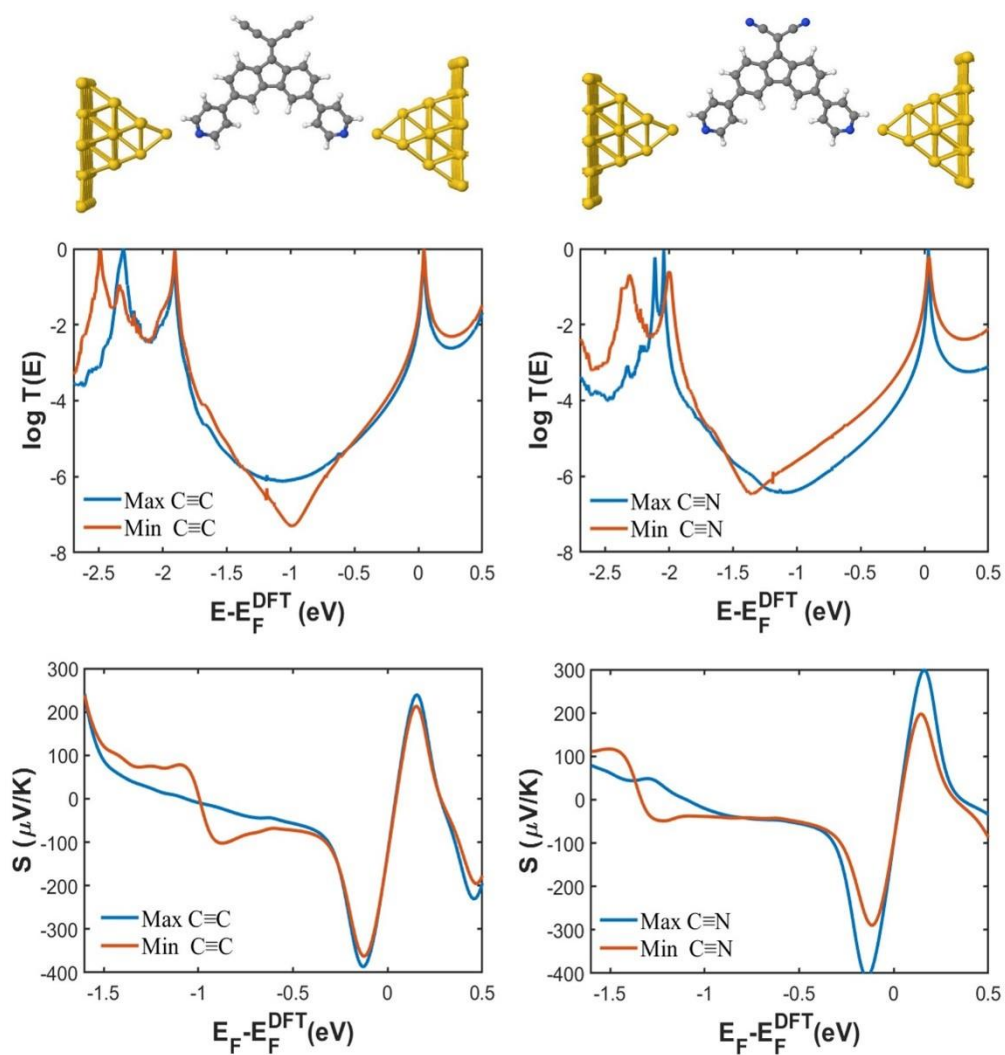
Figure (5.16): The transmission and Seebeck curves of the above configurations (left molecule 1 and right molecule 2), which include the maximum and minimum C≡C , C≡N bond lengths at room temperature. The difference between maximum and minimum lengths for these triple bonds at room temperature (300K) is very small around 0.01 Å, therefore the transmission curves do not show a large shift between them.

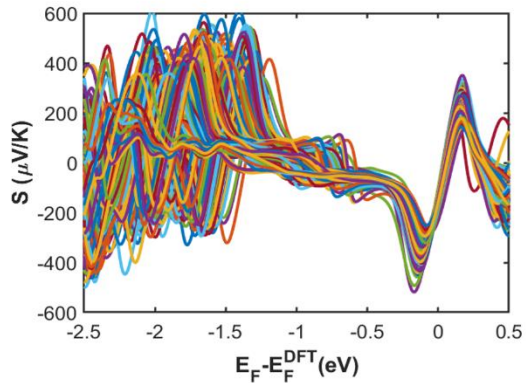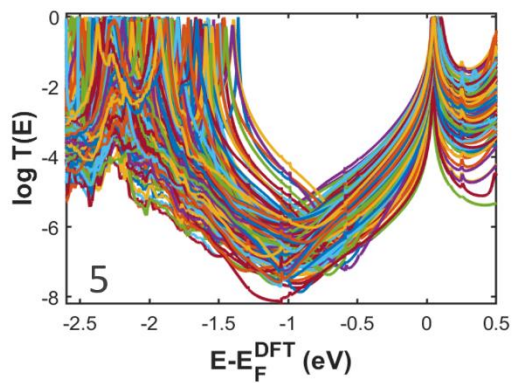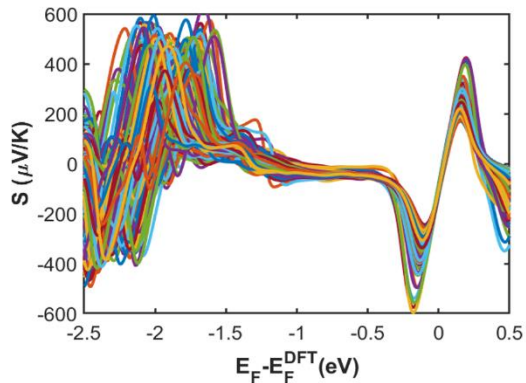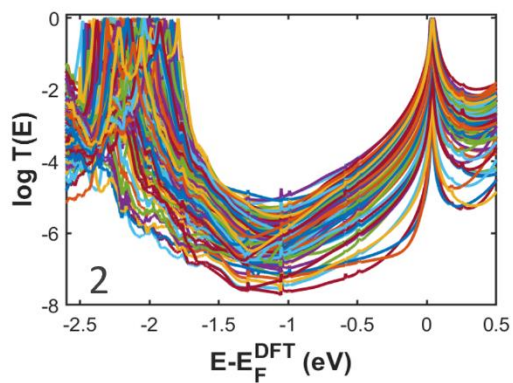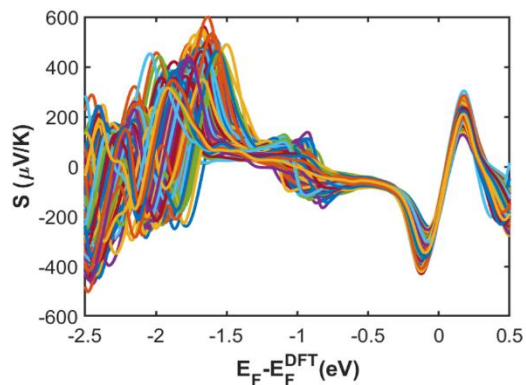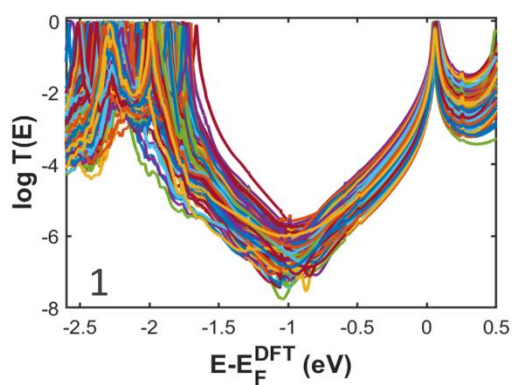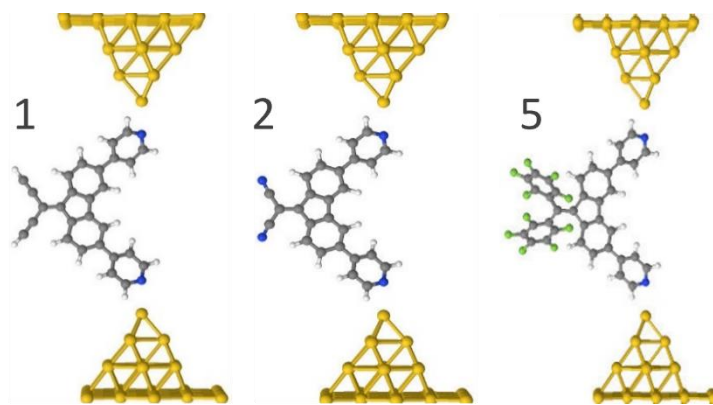**Figure (5.17):** Transmission and Seebeck through the meta compounds (1, 2 and 5) for 213 different geometries obtained from molecular dynamics calculations.

For further investigation, the conductance and Seebeck values are obtained at a Fermi energy value of $E_F = -0.25 \, eV$ and plotted as a histogram (figure 5.18). The C≡C case (i.e. compound 1) has the narrowest conductance distribution (grey bins) where the range values is between $\approx (-3.4G_0$ and $-4.7G_0)$. In contrast, the width of the C≡N histogram or compound 2 (red dashed bins) is larger from $\approx (-3G_0$ to $-5.4G_0)$, but the fluorobenzene case (yellow bins) has the largest conductance distribution between $\approx (-3G_0$ and $-6G_0)$ with the most probable value around $-4G_0$. The Seebeck histograms follow the same trend as the conductance, where the largest distribution is related to the molecule with fluorobenzene pendant group with a range from $\approx (-74.7 \, \mu V/K$ to $-260 \, \mu V/K)$.
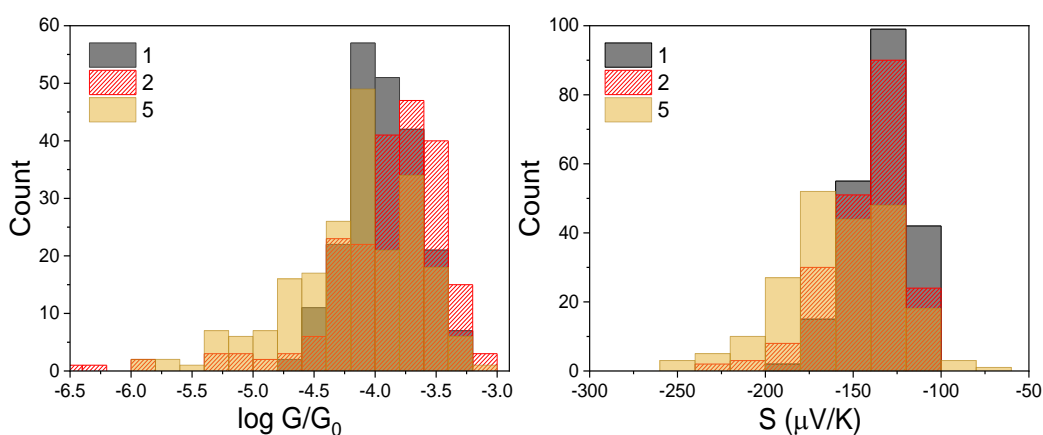
Figure (5.18): The conductance (left) and Seebeck (right) histograms evaluated at $E = -0.25 \, eV$ for the meta-connected compounds (1, 2 and 5) at room temperature.

The change in the conductance is probably related to the torsion angle dependence in the molecules. The larger the torsion angle, the lower the conductance in the molecule [25]–[27]. According to the histograms in figure (5.19), it seems that the C≡N and $(C_6F_5)_2$ side groups cause the end rings to rotate between 0° and 180°, leading to a broad conductance distribution. Conversely, having a narrow conductance distribution in the compound 1 might attributed to

the limited size of the dihedral angle (less than 110°). This may be due to the dipole moment impact between the C-N and C-F atoms, which may produce an electrostatic effect on the backbone of the molecules and force the pyridyl ring to rotate more compared to molecule 1, where the C-C has not dipole moment.
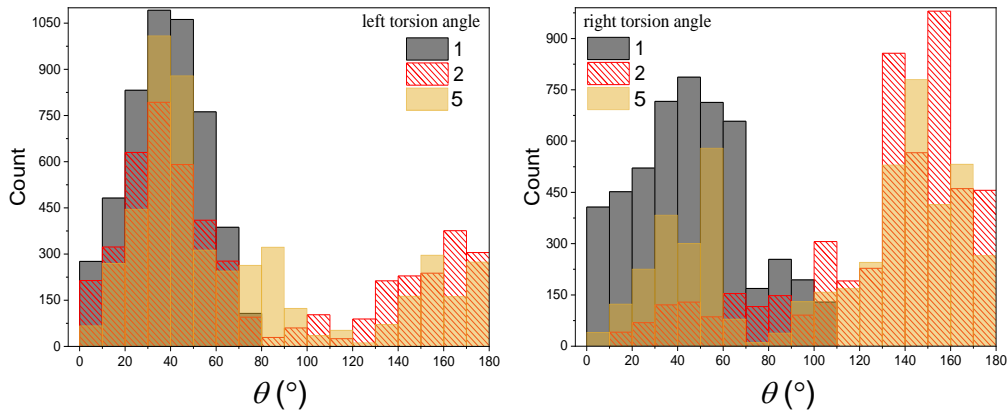
Figure (5.19): The histograms illustrate the rotation size of the torsion angle θ within the phenylpyridyl unit in both sides of the compounds (1, 2 and 5) during the vibrational effect at room temperature using MD simulations.

Table (5.20) shows the average of the conductance and Seebeck values obtained at the Fermi energy $= -0.25\ eV$ at room temperature. From the average calculation, the change in the Seebeck is quite large for different pendant groups, in contrast the change in the conductance is not so large. The Seebeck coefficient is proportional to the derivative of the logarithmic transmission function $\left(S \propto -\ \frac{\partial \ln(T(E))}{\partial E} \right)_{E=E_F}$, and thus a small change in the gradient would have a much bigger effect when we take the average, whereas the conductance (G) would not because it is just a single magnitude of the transmission probability $T(E)$, $G \propto T(E_F)$.

By comparing the conductance and the Seebeck values obtained from the optimum configuration (at 0K) with the average at room temperature (300K), I find that the average tends to enhance the conductance in the three molecules in comparison to the optimum values, and the Seebeck shows similar trends (table 5.20). However, there is a decrease in the average Seebeck of compound 5 compared to the optimum, which is due to the shift of resonances close to the HOMO rather than the LUMO. Hence, if the Fermi energy is shifted further to the middle of the gap, then I would obtain a very different behaviour in the Seebeck coefficient.

	Optimum configuration		The average	
	Log G/G_0	S $(\mu V/K)$	Log G/G_0	S $(\mu V/K)$
1	-4.55	-113.39	-3.93	-134.25
2	-4.34	-132.32	-3.92	-147.27
5	-4.50	-166.88	-4.18	-158.82

Table (5.20): (left table) The conductance and seebeck values for the compounds (1, 2 and 5) at $E = -0.25 \, eV$ in the optimum configration $(i.e. \, at \, 0K)$ compared to the average conductance and seebeck for the same compounds at $E = -0.25 \, eV$ in room temperature (right table)

5.5. Conclusion

This chapter has studied the effect of vibration of the pendant groups on the transport behaviour in five compounds. Compounds 1-4 have similar pendant groups, which contain C≡C and

C≡N bonds, whereas compound 5 is linked to pentafluorobenzene $(C_6F_5)_2$ side group. The calculations were divided into two parts: studying the vibrational effect at zero Kelvin for compounds 1-4, and then carrying out a molecular dynamic simulation for meta compounds (1 2 and 5). The results of first part show quantum interference (QI) phenomena in the presence of the side group, where destructive and constructive QI are found in the meta and para connectivities, respectively, in agreement with the tight-binding model. It is found that varying the pendant groups in molecular junction can be exploited to control the QI and enhance its thermoelectric properties. According to the DFT calculation at zero temperature, the Seebeck coefficient of the meta-connected molecules is strongly sensitive to the fluctuations of the side groups compared to the para case. The MD simulation results revealed that the vibrational effect in compound 1 and 2 is very similar in the terms of the C≡C and C≡N bond stretching vibrations. However, in terms of the transport behaviour, the conductance and Seebeck distributions in compound 2 are wider than in compound 1, and the average Seebeck has shown a large difference in favour of C≡N pendant group. However, the fluctuations in a more charged pendant group such as pentafluorobenzene resulted in a very large shift in the position of its anti-resonance, causing broader conductance and Seebeck distributions, with a higher average Seebeck compared to the other two compounds. Finally, by relating the molecular dynamics results to the zero temperature calculations, I show that they produce similar trends, and since this approach can capture some of the conformational variability inherent to the experiments as mentioned in chapter 1, it could be employed to examine the design of molecules before carrying out the experimental work in order to improve them and exploit the sensitivity of the Seebeck value in meta connected systems.

Bibliography

[1]   Grace, I.M., Olsen, G., Hurtado-Gallego, J., Rincón-García, L., Rubio-Bollinger, G., Bryce, M.R., Agraït, N. and Lambert, C.J., 2020. Connectivity dependent thermopower of bridged biphenyl molecules in single-molecule junctions. *Nanoscale*, *12*(27), pp.14682-14688.

[2]   Ismael, A.K., Grace, I. and Lambert, C.J., 2015. Increasing the thermopower of crown-ether-bridged anthraquinones. *Nanoscale*, *7*(41), pp.17338-17342.

[3]   Wang, X., Ismael, A., Almutlg, A., Alshammari, M., Al-Jobory, A., Alshehab, A., Bennett, T.L., Wilkinson, L.A., Cohen, L.F., Long, N.J. and Robinson, B.J., 2021. Optimised power harvesting by controlling the pressure applied to molecular junctions. *Chemical Science*, *12*(14), pp.5230-5235.

[4]   Ismael, A.K., Rincón-García, L., Evangeli, C., Dallas, P., Alotaibi, T., Al-Jobory, A.A., Rubio-Bollinger, G., Porfyrakis, K., Agraït, N. and Lambert, C.J., 2022. Exploring seebeck-coefficient fluctuations in endohedral-fullerene, single-molecule junctions. *Nanoscale Horizons*, *7*(6), pp.616-625.

[5]   Ye, J., Al-Jobory, A., Zhang, Q.C., Cao, W., Alshehab, A., Qu, K., Alotaibi, T., Chen, H., Liu, J., Ismael, A.K. and Chen, Z.N., 2022. Highly insulating alkane rings with destructive σ-interference. *SCIENCE CHINA-CHEMISTRY*.

[6]   Finch, C.M., Garcia-Suarez, V.M. and Lambert, C.J., 2009. Giant thermopower and figure of merit in single-molecule devices. *Physical review b*, *79*(3), p.033405.

[7]   Naghibi, S., Ismael, A.K., Vezzoli, A., Al-Khaykanee, M.K., Zheng, X., Grace, I.M., Bethell, D., Higgins, S.J., Lambert, C.J. and Nichols, R.J., 2019. Synthetic control of quantum interference by regulating charge on a single atom in heteroaromatic molecular junctions. *The journal of physical chemistry letters*, *10*(20), pp.6419-6424.

[8]   Chang, W.B., Mai, C.K., Kotiuga, M., Neaton, J.B., Bazan, G.C. and Segalman, R.A., 2014. Controlling the thermoelectric properties of thiophene-derived single-molecule junctions. *Chemistry of Materials*, *26*(24), pp.7229-7235.

[9]   Miao, R., Xu, H., Skripnik, M., Cui, L., Wang, K., Pedersen, K.G., Leijnse, M., Pauly, F., Warnmark, K., Meyhofer, E. and Reddy, P., 2018. Influence of quantum interference

on the thermoelectric properties of molecular junctions. *Nano letters*, *18*(9), pp.5666-5672.

[10] Huang, B., Liu, X., Yuan, Y., Hong, Z.W., Zheng, J.F., Pei, L.Q., Shao, Y., Li, J.F., Zhou, X.S., Chen, J.Z. and Jin, S., 2018. Controlling and observing sharp-valleyed quantum interference effect in single molecular junctions. *Journal of the American Chemical Society*, *140*(50), pp.17685-17690.

[11] Lambert, C.J., 2015. Basic concepts of quantum interference and electron transport in single-molecule electronics. *Chemical Society Reviews*, *44*(4), pp.875-888.

[12] Soler, J.M., Artacho, E., Gale, J.D., García, A., Junquera, J., Ordejón, P. and Sánchez-Portal, D., 2002. The SIESTA method for ab initio order-N materials simulation. *Journal of Physics: Condensed Matter*, *14*(11), p.2745.

[13] Troullier, N. and Martins, J.L., 1991. Efficient pseudopotentials for plane-wave calculations. *Physical review B*, *43*(3), p.1993.

[14] Langreth, D.C. and Perdew, J.P., 1977. Exchange-correlation energy of a metallic surface: Wave-vector analysis. *Physical Review B*, *15*(6), p.2884.

[15] Ceperley, D.M. and Alder, B.J., 1980. Ground state of the electron gas by a stochastic method. *Physical review letters*, *45*(7), p.566.

[16] Boys, S.F. and Bernardi, F.J.M.P., 1970. The calculation of small molecular interactions by the differences of separate total energies. Some procedures with reduced errors. *Molecular Physics*, *19*(4), pp.553-566.

[17] Boese, A.D., Jansen, G., Torheyden, M., Höfener, S. and Klopper, W., 2011. Effects of counterpoise correction and basis set extrapolation on the MP2 geometries of hydrogen bonded dimers of ammonia, water, and hydrogen fluoride. *Physical Chemistry Chemical Physics*, *13*(3), pp.1230-1238.

[18] Ferrer, J., Lambert, C.J., García-Suárez, V.M., Manrique, D.Z., Visontai, D., Oroszlany, L., Rodríguez-Ferradás, R., Grace, I., Bailey, S.W.D., Gillemot, K. and Sadeghi, H., 2014. GOLLUM: a next-generation simulation tool for electron, thermal and spin transport. *New Journal of Physics*, *16*(9), p.093029.

[19] Khanikaev, A.B., Wu, C. and Shvets, G., 2013. Fano-resonant meta materials and their applications. *Nanophotonics*, *2*(4), pp.247-264.

[20] Zheng, Y., Duan, P., Zhou, Y., Li, C., Zhou, D., Wang, Y., Chen, L.C., Zhu, Z., Li, X., Bai, J. and Qu, K., 2022. Fano Resonance in Single-Molecule Junctions. *Angewandte Chemie*, *134*(40), p.e202210097.

[21] Ismael, A.K., Grace, I. and Lambert, C.J., 2017. Connectivity dependence of Fano resonances in single molecules. *Physical Chemistry Chemical Physics*, *19*(9), pp.6416-6421.

[22] Paulsson, M., Krag, C., Frederiksen, T. and Brandbyge, M., 2009. Conductance of alkanedithiol single-molecule junctions: a molecular dynamics study. *Nano Letters*, *9*(1), pp.117-121.

[23] Li, Z. and Franco, I., 2019. Molecular electronics: Toward the atomistic modeling of conductance histograms. *The Journal of Physical Chemistry C*, *123*(15), pp.9693-9701.

[24] Frenkel, D. and Smit, B., 2001. *Understanding molecular simulation: from algorithms to applications* (Vol. 1). Elsevier.

[25] Venkataraman, L., Klare, J.E., Nuckolls, C., Hybertsen, M.S. and Steigerwald, M.L., 2006. Dependence of single-molecule junction conductance on molecular conformation. *Nature*, *442*(7105), pp.904-907.

[26] Vonlanthen, D., Mishchenko, A., Elbing, M., Neuburger, M., Wandlowski, T. and Mayor, M., 2009. Chemically controlled conductivity: torsion-angle dependence in a single-molecule biphenyldithiol junction. *Angewandte Chemie International Edition*, *48*(47), pp.8886-8890.

[27] Chen, W., Li, H., Widawsky, J.R., Appayee, C., Venkataraman, L. and Breslow, R., 2014. Aromaticity decreases single-molecule junction conductance. *Journal of the American Chemical Society*, *136*(3), pp.918-920.

Chapter 6

The conductance behaviour of pendant trans-coordinated palladium complexes

6.1. Introduction

Over the past decade, the ability to measure the conductance of individual molecules has led to a greater understanding of structure property relations, revealing the importance of how anchor groups impact quantum interference [1]–[7]. Such investigations have been dominated by pure organic conjugated molecules (e.g. OPE's) [8]–[10]. However, the inclusion of metal ions in molecular wires has often proved to be alluring due to the potential to enhance or gate conductance by external stimuli [11], [12].

The metal complexes that have been measured in a molecular junction can be separated into two groups: those where the metal ion is directly in the linear conductance path [13], [14] or the metal ion is coordinated pendant to the conductive path [15]. The former cases have shown that the inclusion of the metal could achieve conductance enhancement or redox gating [16]–[18] whilst the latter had either no impact or showed a large destructive quantum interference feature [15].

With this in mind, a series of molecules has been designed by Ross Davidson at the university of Durham to test whether the introduction of a metal atom with a d-orbital can alter the quantum transport and quantum interference of a molecule. These molecules can be seen in Figure 6.1. The ligand (L^P and L^M) provides a conjugated backbone resulting in a conductive

path that exists with or without the coordinated metal. In the case of the complexed Pd^P and Pd^M the metal ion is co-ordinated between the nitrogen atoms of the pyridine rings and the aim is to understand if this part of the molecule is directly involved or pendant to the conductive path.
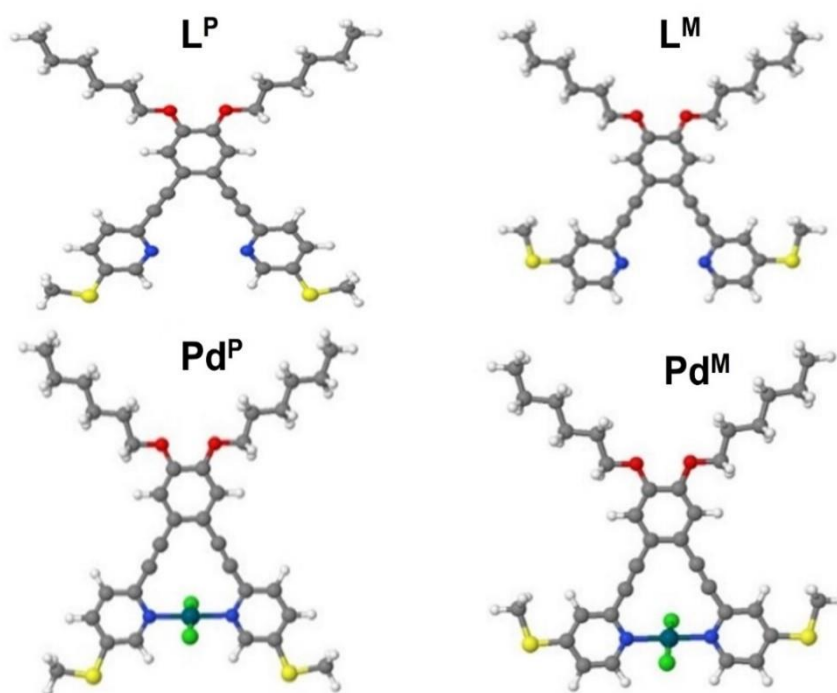

Figure (6.1): Ball and stick representation of the molecules L^P, L^M, Pd^P and Pd^M. Colour representation: hydrogen (white), carbon (grey), nitrogen (Blue), sulfur (yellow), chlorine (green) and palladium (dark grey).

6.2. Molecule Isomers

This chapter will focus on the theoretical electron transport behaviour of these four molecules with the aim of calculating both the conductance G and Seebeck coefficient S. The optimum geometry of each isomer of the molecules was calculated using the density functional code SIESTA with the same parameters as described in chapter 4 (section 4.2). In the case of the ligand molecules (L^P and L^M) the chemical structure makes it possible for the geometry to change as the nitrogen atom of the pyridine unit can either point inwards to the centre of the molecule or point outwards. This is important as pyridine can act as an anchor unit with gold attaching to the nitrogen atom. I identify three possible configurations of L^P due to the orientation of the pyridine; 1 – both pyridines pointing inwards, 2 – both pyridines pointing outwards and 3 – one pyridine pointing in and one points out. The second important orientation is that of the methyl group, which has its minimum energy when it is aligned with the plane of the pyridine ring. Therefore, for molecule L^P the methyl group can point left or right, and this leads to 3 possible orientations; A – left and right, B – right and right and C right and left. I also consider the case when the methyl groups are rotated out of the plane by 90 which is geometry D. The corresponding relaxed optimum geometry of each of the 12 isomers can be seen in figure 6.2 along with the ground state energy E_g relative to the minimum energy 0eV. In this series the geometry 3C has the lowest energy which is the case of the pyridines pointing in opposite directions and may be due to an interaction between the nitrogen and the hydrogen on the opposite ring. Note, that the energy difference to 3A and 3B is very small (0.01eV) which shows orientation of the methyl groups is less important.
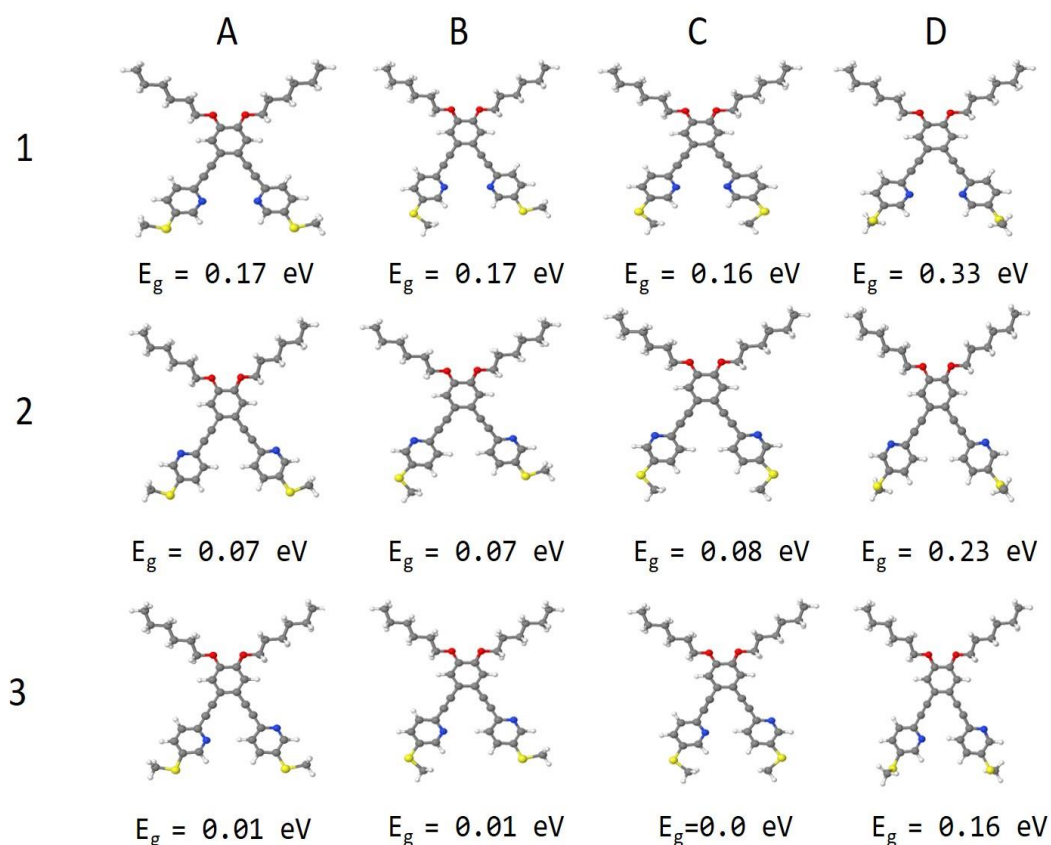
Figure (6.2): Possible isomers of the L^p molecule including their ground state energy E_g relative to the minimum 0 eV, where isomer is 3C has the lowest energy. The figure shows different position of SMe group with 1 – both pyridines pointing inwards, 2 – both pyridines pointing outwards and 3 – one pyridine pointing in and one points out.

In figure 6.3, I repeat the process for the L^M molecule. Again, there are the same three configurations of the pyridine rings (1-3), however due to symmetry there is an extra orientation D for the methyl group in the case of geometry 3. Orientation E again corresponds to the methyl groups rotated 90° out of the plane. The lowest energy isomer is 3C with the pyridine rings pointing in opposite directions.
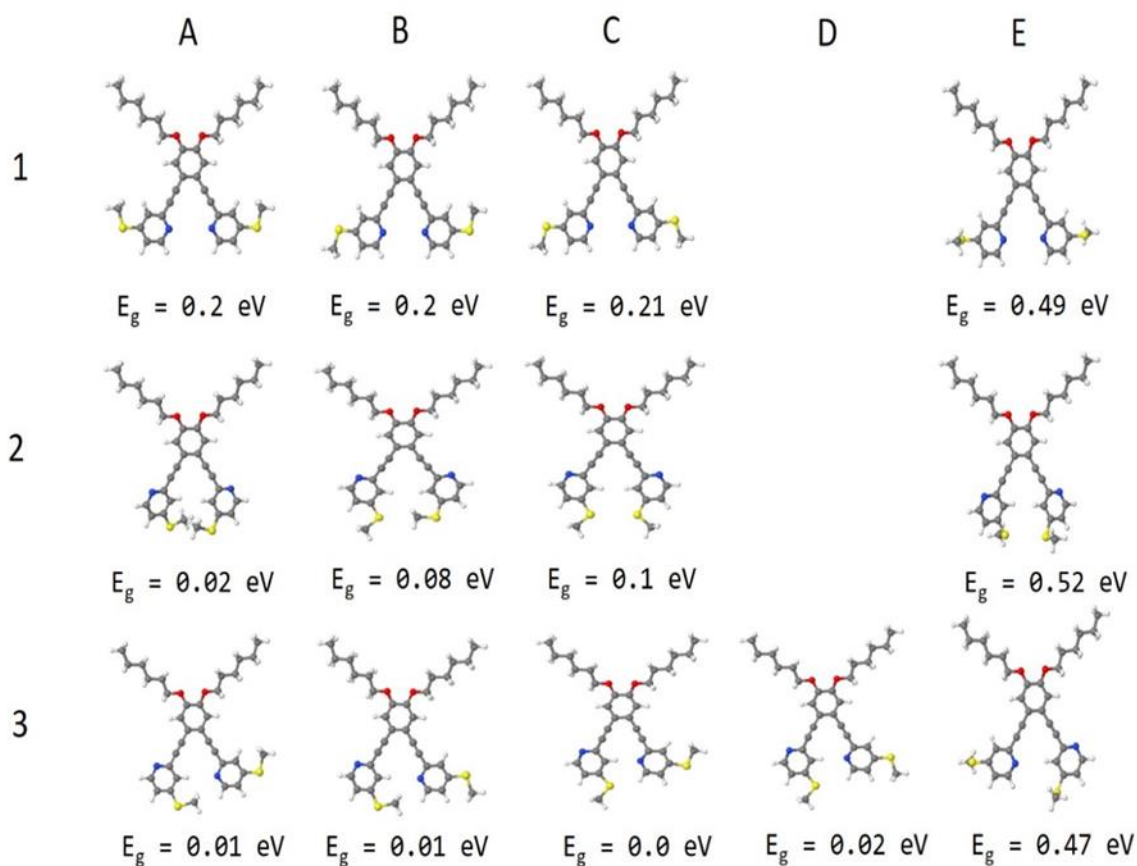
Figure (6.3): Possible isomers of the L^M molecule including their ground state energy E_g relative to the minimum 0eV, where isomer 3C has the lowest energy. In this study I applied the calculation for the geometries in the third panel, which are more likely to happen in the junction since they possess low ground state energy.

In the case of the complex molecules Pd^P and Pd^M, the orientation of the pyridine rings is fixed so only the methyl groups are free to move. As before we assume four different positions A–D, where for Pd^P A – left and right, B – left and left, C – right and left and D – methyl rotated 90° out of the plane. For Pd^M the orientations are A – up and up, B – up and down, C – down and down and D – rotated 90° to the plane. The energy difference from the minimum is small except in the case of the isomer D.
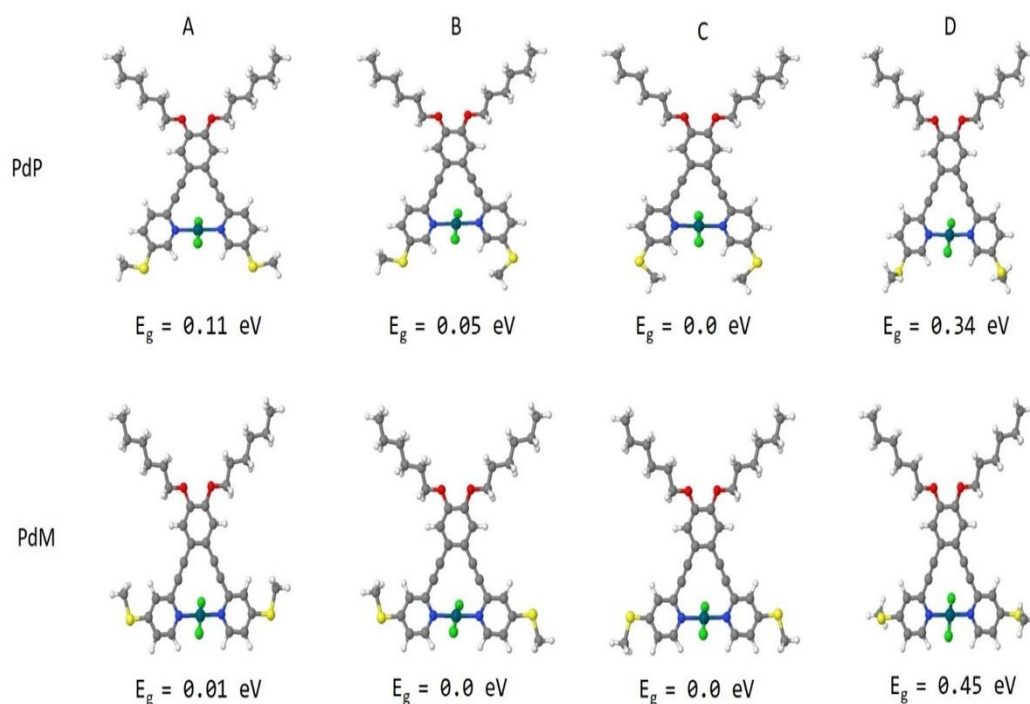
Figure (6.4): Possible isomers of the Pd^P and Pd^M molecules including their ground state energy relative to the minimum 0eV. The SMe groups are rotated to different position around the sulfur atom. The energy difference from the minimum is small except in the case of the isomer D.

6.3. Binding to gold electrodes

To model the expected behaviour in a molecular junction, the next step is to understand how the molecule can attach to the electrodes. To achieve this, the binding energy between the molecule and a gold electrode was calculated. The system was treated as a two-component object, where the gold electrode is A, and the molecule is B. Due to basis set superposition errors (BSSE), when using localized basis sets, I used a counterpoise method to evaluate the binding energy E_{Bind}. This is given by the following equation:

$$E_{Bind} = E_{AB}^{AB} - (E_A^{AB} + E_B^{AB})$$

where E_{AB}^{AB} is the ground state energy of the gold electrode (A) and molecule (B), E_A^{AB} is the energy of the gold (A) in the basis of the dimer AB and E_B^{AB} is the energy of the molecule in the basis of the dimer AB. To find the optimum binding geometry I relaxed the position of the molecule relative to a single fixed gold electrode using SIESTA, so that all forces were less than 0.01eV/Å. Here, the gold electrode consisted of 3 layers of (111) gold containing 25 atoms with a surface of pyramidal gold atoms to mimic the behaviour of an STM measurement. For the L^M and L^P ligand molecules, I identify three possible 'contact' sites for the attachment of a gold electrode and the results can be seen in figure 6.5. The first contact site is the SMe anchor group and in the case of the methyl group being aligned with the pyridine ring the binding energy is -0.23eV for L^P and -0.18eV for L^M, however in the case of the methyl group being rotated out of the plane the binding energy increases to -0.45eV for L^P and -0.34 for L^M. This result predicts that upon binding, it is more energetically favourable for the methyl group to rotate out of the plane of molecule upon binding to the tip gold atom.

The second contact site is the nitrogen atom of the pyridine ring, however the nature of the contact to the gold depends on the orientation of the pyridine ring for the given isomer. In the case when the nitrogen is pointing outwards (e.g. $L^P(2)$) the nitrogen atom is in the 'ortho' position for binding and gives a binding energy of -0.52eV for L^P and -0.58eV for L^M. When the nitrogen atom is pointing inwards (e.g. $L^P(1)$) the gold can bind to it when the plane of the molecule is parallel to the gold surface. The gold – nitrogen binding distance is 2.55Å for L^P with a binding energy of -0.3eV with similar values for L^M.
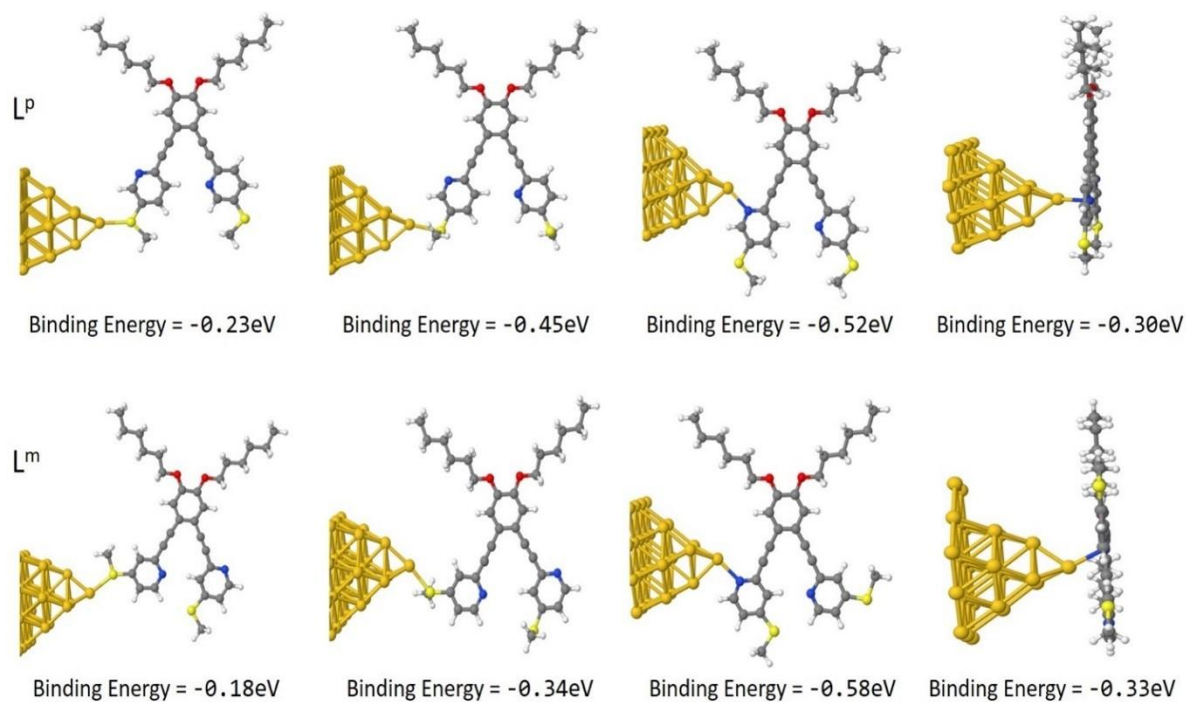
Figure (6.5): Binding energy of L^P and L^M molecule contacted to a gold electrode in four different locations. In the case of the SMe being aligned with the pyridine ring the binding energy is -0.23eV for L^P and -0.18eV for L^M, however in the case of the methyl group being rotated out of the plane the binding energy increases to -0.45eV for L^P and -0.34 for L^M.

The same procedure was applied to the complex molecules Pd^P and Pd^M. In this case there is no binding to the ortho position as the pyridine rings are fixed. This means that there are two contact locations for the complex molecules and the results can be seen in Figure 6.6. The first location is again via the SMe group and as for the ligand molecules the optimum binding energy occurs when the methyl group rotates out of the plane, with a value of -0.46eV for Pd^P and -0.21eV for Pd^M. The second location is again the middle of the molecule, however this time the binding site is the chlorine atom attached to the palladium atom and the lead is at right angles to the plane of the molecule. This gives a binding energy of -0.67 eV for both Pd^P and Pd^M.

Now, depending on where the gold lead attaches to the molecule, this means that there are multiple junction geometries that can form. For example, the Pd^P molecule, the left electrode attaches to the left SMe, and the right electrode could attach to the right SMe, this would be a para-para (p-p) connection. A second geometry forms when the left lead attaches to the left SMe group and the right lead contacts to central chlorine atom which would be a para-middle connection (p-mid) and the third geometry forms when the left lead attaches to one of the chlorine atoms and the right lead attaches to the other chlorine atom which would be a middle-middle connection (mid-mid). In this geometry the transport is through the plane of the molecule.
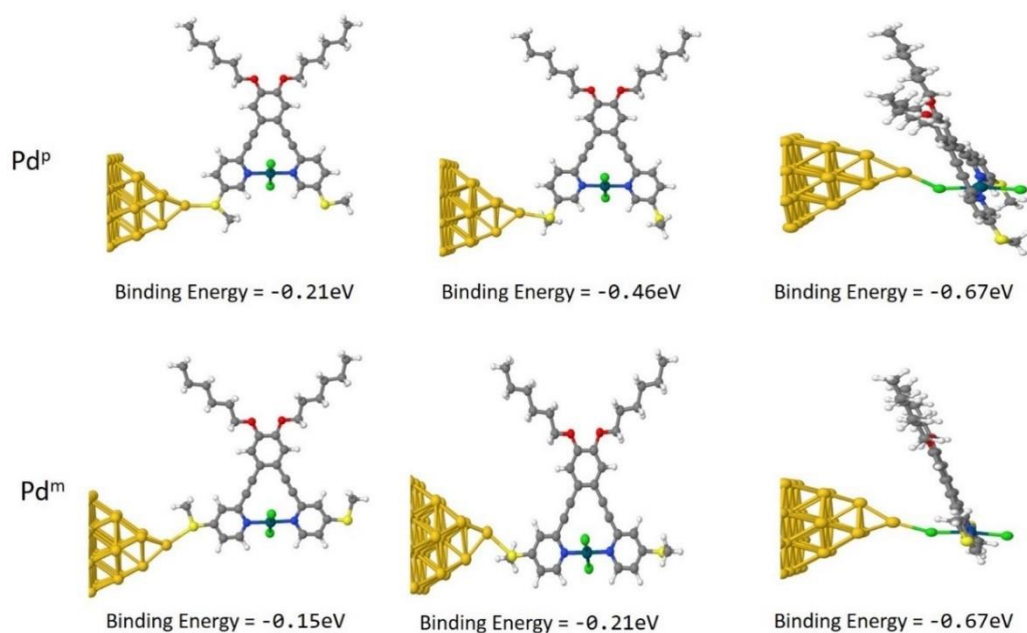

Figure (6.6): Binding energy of Pd^P and Pd^M molecule to a gold electrode. The optimum binding energy occurs when the methyl group rotates out of the plane, with a value of -0.46eV for Pd^P and -0.21eV for Pd^M. The binding energy for Au-Cl is -0.67 eV for both Pd^P and Pd^M.

6.4. Results and Discussion

6.4.1. Electron transport calculations

As a first example I compare the behaviour of the complex Pd^P (C) and Pd^M (C) with the ligands L^P (1C) and L^M (1C), the isomer label is in the bracket and corresponds to figure 6.2-4. The molecules were attached to gold electrodes via the SMe anchor groups in the optimum binding position as calculated previously with the resulting junction geometries for the para-para connectivities shown in figure 6.7a and b and the meta to meta in 6.7c and d. The transmission coefficient *T(E)* for each of these geometries was calculated using Gollum and the results can be seen in Figure (6.8). The comparison between the para connected ligand L^P (black line) and complex Pd^P (blue line), shows that in both cases the Fermi energy (E-E_F^0 = 0eV) sits in the HOMO-LUMO gap. In this case the transmission through the ligand is smaller than the complex, this is due to the HOMO LUMO gap of the complex molecule being smaller than the ligand meaning that the complex enhances the conductance.

The shape of the HOMO resonance is also different for the complex Pd^P which has a Fano line shape (E-E_F^0 = -1eV) in comparison to the Lorentzian shape of the LUMO resonance. This can be explained by the orbitals of the molecule which are shown in Figure (6.9), here the HOMO orbital is localized on the metal complex of Pd^P in comparison to the delocalized nature of the LUMO. Figure (6.8) also shows the behaviour for the meta connected molecules L^M and Pd^M, which show a similar pattern to the para molecules, that the conductance of the complex Pd^M is greater than that of the ligand L^M. The HOMO orbital is again localized for the complex and produces a Fano line shape. It should also be noted that the conductance of $L^M < L^P$ and $Pd^M <$ Pd^P.
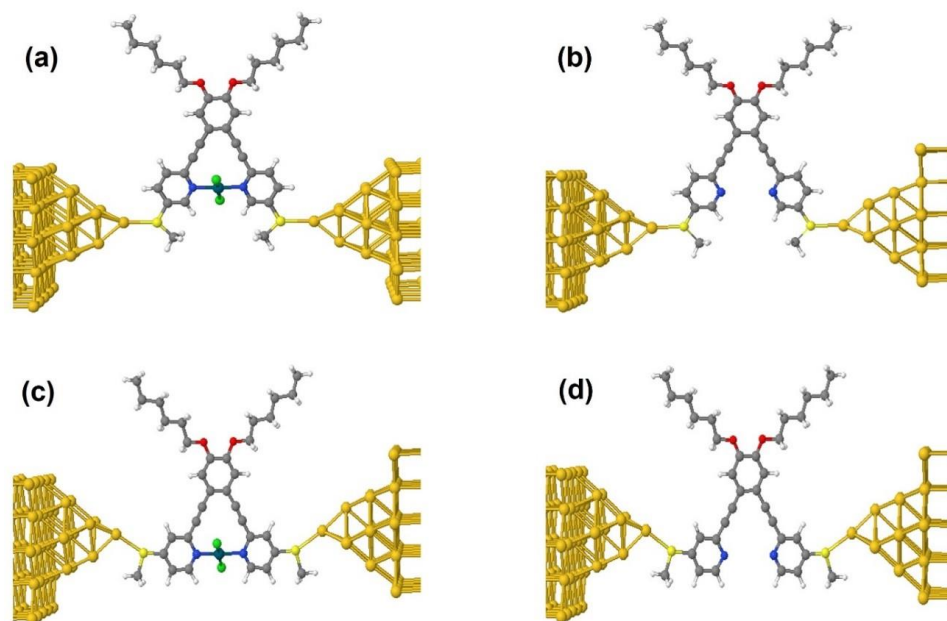
Figure (6.7): Molecule junction geometry for (a) Pd^P para-para (p-p), (b) L^P para-para (p-p), (c) Pd^M meta-meta (m-m) and (d) L^M meta-meta (m-m).
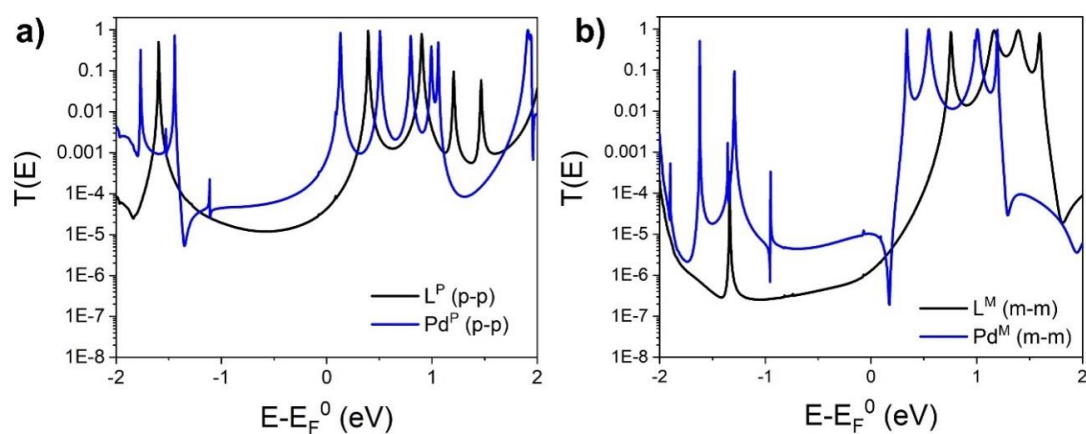
Figure (6.8): Zero bias transmission coefficient *T(E)* for molecules (a) L^P and Pd^P and (b) molecules L^M and Pd^M contacted to gold electrodes via the SMe anchor groups. The HOMO LUMO gap of the complex molecules is smaller than the ligand, meaning that the complex enhances the conductance. The shape of the HOMO resonance is also different for the complex which has a Fano line shape due to the localized orbitals in figure (6.9).

Therefore, these transmission curves show that the complex, does not alter the transport path through the molecule, and the small enhancement in conductance is due to a shifting of the molecular orbitals and the change in the HOMO-LUMO gap size.
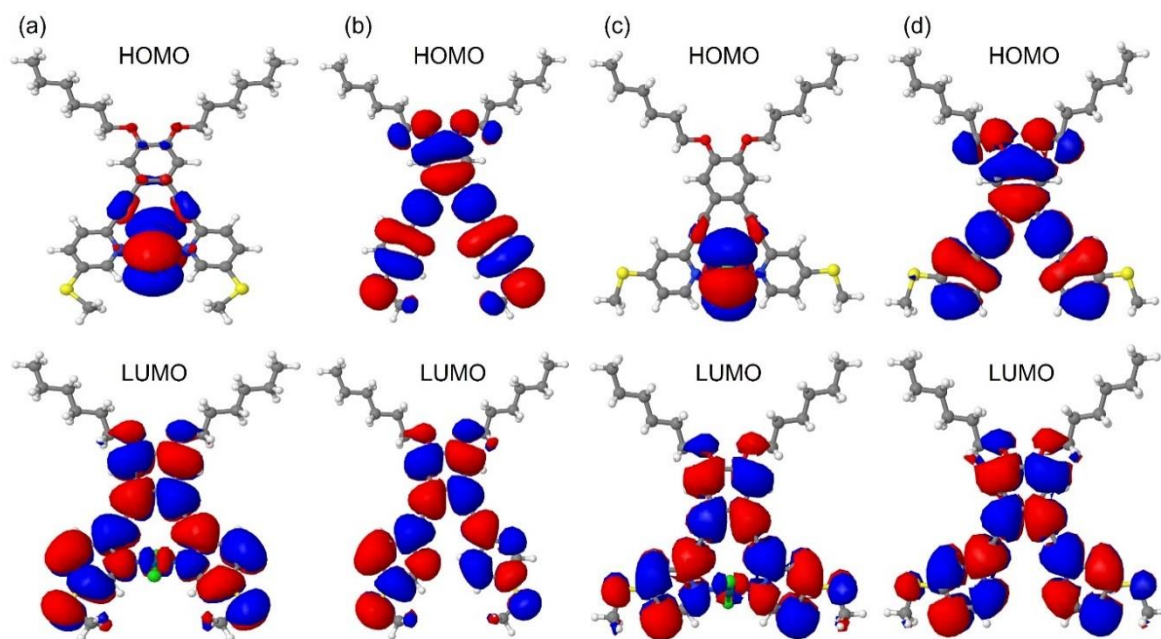
Figure (6.9): HOMO and LUMO orbitals of molecules (a) Pd^P, (b) L^P, (c) Pd^M and (d) L^M, where the results show a localization of the HOMO orbital on the metal complex of Pd^P and Pd^M, and this is producing a Fano line shape near the HOMO resonance as shown in figure (6.8).

6.4.2. Multiple Conductance Groups

Having investigated the general nature of transport through the four molecules when contacted through the SMe anchor groups, I now calculate the behaviour depending on the multiple junction configurations that can be formed. For the complex Pd^P there are three possible junction geometries, 1-the para-para (p-p) connection through the right and left SMe groups,

2- the para-middle (p-mid) connection where one lead attaches to an SMe group and the second contacts to a chlorine atom of the metal complex and 3 – the middle-middle (mid-mid) connection where the leads attach to the two chlorine atoms and the transport is through the plane of the molecule. The transmission curves for these three geometries can be seen in figure 6.10 and show the general trend $G_{mid-mid} > G_{p-mid} > G_{p-p}$. This can be explained by the shorter distance for the path of the electrons though the molecule [19].

Figure (6.10): Zero bias transmission coefficient *T(E)* against electron energy E for three different binding configurations of Pd^P, and the curves show the general trend $G_{mid-mid} > G_{p-mid} > G_{p-p}$. The para-para (p-p) connection through both SMe groups, the para-middle (p-mid) connection where one lead attaches to an SMe group and the second contacts to Cl atom, and the middle-middle (mid-mid) connection where the leads attach to the two chlorine atoms. The decrease in the distance between the left and right electrodes results in an increase in the transmission coefficient, as shown in mid-mid case where the contact via the Cl atoms.

Figure 6.11 shows the transmission behaviour for the meta-complex Pd^M, again it has three different junction geometries, 1 – contact through the meta connected SMe groups (m-m), 2 –

the meta-SMe and the chlorine atom (m-mid) and 3 – the chlorine to chlorine (mid-mid). The same pattern emerges with the mid-mid having the highest conductance. Note, that in the case of transport through the plane the conductance value is similar for both Pd^P and Pd^M as it is no longer connected through a para or meta connection.
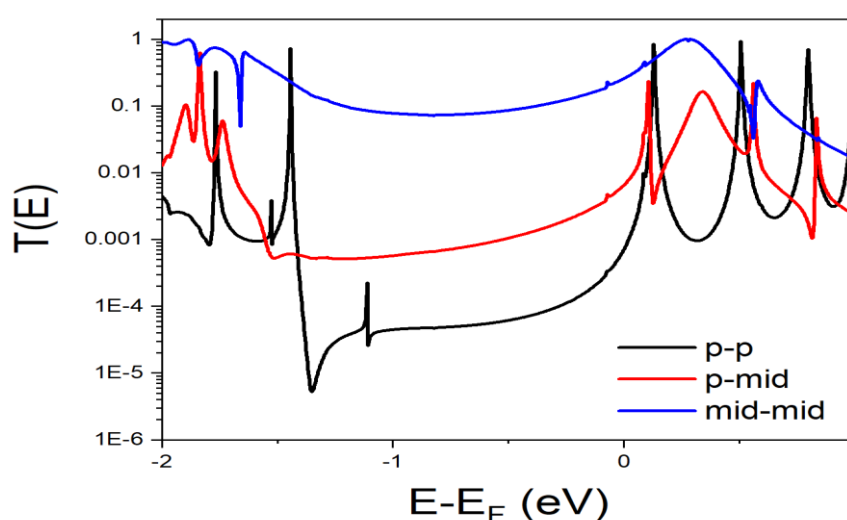

Figure (6.11): Zero bias transmission coefficient *T(E)* against electron energy E for three different binding configurations of Pd^M, and the curves show the general trend $G_{mid-mid} > G_{p-mid} > G_{p-p}$. The meta-meta (m-m) connection through both SMe groups, the meta-middle (m-mid) connection where one lead attaches to an SMe group and the second contacts to Cl atom, and the middle-middle (mid-mid) connection where the leads attach to the two Cl atoms. The decrease in the distance between the left and right electrodes leads to an increase in the transmission coefficient, as shown in mid-mid case where the contact via the Cl atoms.

Figure 6.12 shows the transmission for molecule L^P. For the lowest energy isomer, there are five possible junction geometries. 1 – left lead and right lead contact to left and right SMe groups (p-p), 2 – left lead contacts to the nitrogen atom in the ortho position and the right lead

128

to the right SMe group (o-p), 3 – left lead contacts to the left SMe group and the right lead

contacts the nitrogen atom in the middle of the molecule (p-mid) 4 – left lead connects to the

ortho nitrogen and the right lead contacts to the middle nitrogen atom (o-mid) and 5 – left and

right lead contact to the middle nitrogen atoms so that transport is through the plane of the

molecule.

The p-p connection gives similar behaviour to the o-p, which is expected, the p-mid and o-mid

also have similar conductance behaviour and finally the mid-mid gives the highest

conductance.

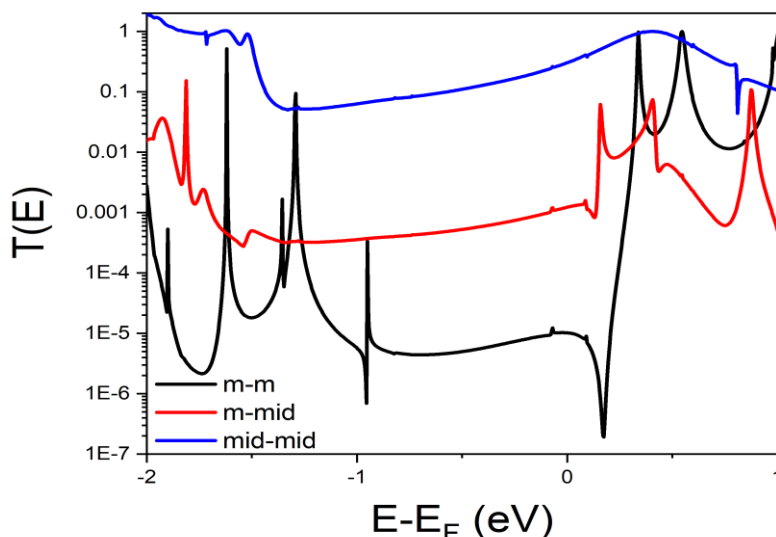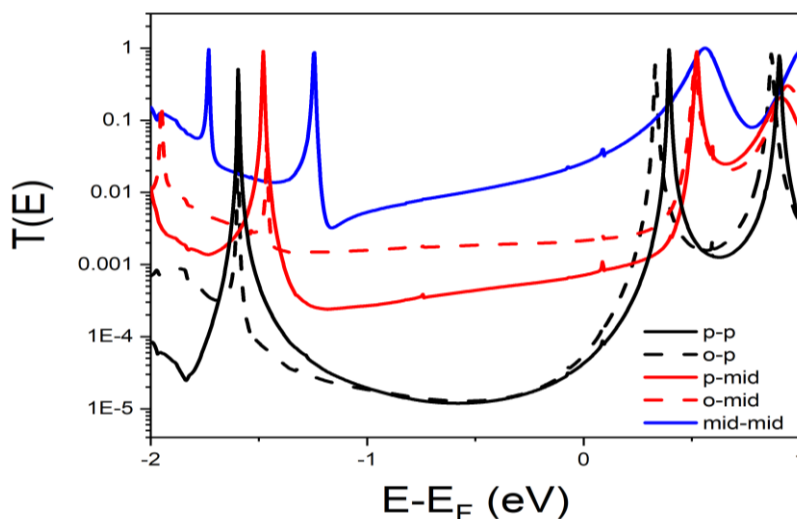**Figure (6.12):** Zero bias transmission coefficient *T(E)* against electron energy E for five

different binding configurations of L^P. The curve of mid-mid contact via the two Cl atoms

shows the highest conductance, whereas the lowest conductance is due to the p-p connection

via the SMe anchors and the o-p connection via the nitrogen atom in the ortho position and

the right SMe group.

129

The transport through the L^M molecule (figure 6.13) shows similar behaviour, although in this case the m-m gives a lower conductance than the m-o. Transport through the middle of the molecule again gives the highest conductance.
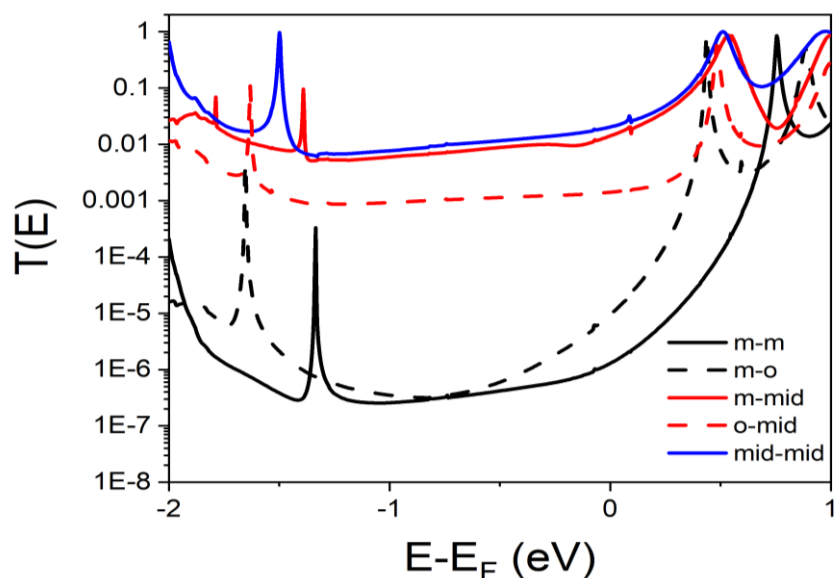
Figure (6.13): Zero bias transmission coefficient *T(E)* against electron energy E for different binding configurations of L^M. The transmission curve of mid-mid contact via the two Cl atoms shows the highest conductance due to the shorter distance for the path of the electrons though the molecule, whereas the transmission curve of m-m connection via the SMe groups gives the lowest conductance.

6.4.3. Conductance and Seebeck values

The conductance and Seebeck values are evaluated at room temperature for two different Fermi energies. the original DFT calculated Fermi energy E_F^0 and $E_F^1 = E_F^0 - 0.5eV$. Typically, DFT tends to incorrectly predict the position of the Fermi energy and therefore, I evaluate at two values with E_F^1 chosen to be close to the middle of the HOMO-LUMO gap. Typically, the

results show that in the case of the complex molecules (Table 6.1 and 6.2) there are three conductance groups as expected from the transmission curves and for the Fermi energy in the middle of the gap all the groups give a low value for the Seebeck coeffiecent ($< 20\mu V/K$) with a negative sign to demonstrate LUMO dominated transport.

Table 6.3 and 6.4 show the conductance and Seebeck values for the ligand molecules, in this case there are five geometries, but they tend to give three conductance groups with the sme-sme contact (p-p) and sme-ortho contact (p-o) giving the lowest. The mid-mid gives the highest conductance and the sme-mid (p-mid) and ortho-mid (o-mid) a value in the middle. As was the case for the complex molecules the Seebeck values in the HOMO-LUMO gap are again very small ($< 20\mu V/K$) and negative.

	$Log\ G(E_F^0)\ /G_0$	$S(E_F^0)\ /mV/K$	$Log\ G(E_F^1)\ /G_0$	$S(E_F^1)\ /mV/K$
p-p	-2.82	-337.0	-4.51	-11.0
p-mid	-2.32	-110.7	-3.27	-14.5
mid-mid	-0.87	-33.3	-1.36	-7.6

Table (6.1): Conductance and Seebeck values at the two Fermi energies $E_F^0 = 0\ eV$ and $E_F^1 = -0.5\ eV$ for the Pd^P molecule for three different contact geometries. The Fermi energy $E_F^0 = 0\ eV$ is the DFT electrode fermi energy, which is not relaible. The results show small increase in the conductance between the p-p and mid-mid connections at $E_F^1 = -0.5\ eV$. The shorter the distance for the path of the electrons though the molecule, the higher the transmission and thus the conductance.

	Log G(E_F^0) /G$_0$	S(E_F^0) /μV/K	Log G(E_F^1) /G$_0$	S(E_F^1) /μV/K
m-m	-5.26	-84.1	-5.60	-8.4
m-mid	-3.18	-38.5	-3.58	-8.4
mid-mid	-0.81	-22.0	-1.25	-10.6

Table (6.2): Conductance and Seebeck values at the two Fermi energies $E_F^0 = 0\ eV$ and $E_F^1 = -0.5\ eV$ for the Pd^M molecule for three different contact geometries. The Fermi energy $E_F^0 = 0\ eV$ is the DFT electrode fermi energy, which is not relaible. The results show small increase in the conductance between the m-m and mid-mid connections at $E_F^1 = -0.5\ eV$.

	Log G(E_F^0) /G$_0$	S(E_F^0) /μV/K	Log G(E_F^1) /G$_0$	S(E_F^1) /μV/K
p-p	-4.65	-49.9	-5.21	-3.7
p-o	-4.51	-84.4	-5.18	-2.1
p-mid	-3.44	-11.6	-3.66	-6.7
o-mid	-2.96	-5.2	-3.03	-2.0
mid-mid	-1.88	-21.3	-2.27	-9.4

Table (6.3): Conductance and Seebeck values at two Fermi energies $E_F^0 = 0\ eV$ and $E_F^1 = -0.5\ eV$ for the L^P molecule of five different contact geometries (p-p), (p-o), (p-mid), (o-mid) and (mid-mid). The p-p and p-o give the lowest conductance, the mid-mid contact gives the highest conductance, and the p-mid and o-mid have a value in the middle. The Seebeck results do not show enhancement.

	Log G($E_F{}^0$) /G_0	*S($E_F{}^0$) /μV/K*	*Log G($E_F{}^1$) /G_0*	*S($E_F{}^1$) /μV/K*
m-m	-6.17	-38.1	-6.67	-9.5
m-o	-5.29	-70.2	-6.51	-25.5
m-mid	-2.14	-23.6	-2.35	-5.8
o-mid	-3.15	-7.6	-3.24	-2.8
mid-mid	-1.98	-17.4	-2.23	-5.5

Table (6.4): Conductance and Seebeck values at two Fermi energies $E_F^0 = 0\ eV$ and $E_F^1 = -0.5\ eV$ for the L^M molecule of five different contact geometries (m-m), (m-o), (m-mid), (o-mid) and (mid-mid). The m-m and m-o give the lowest conductance, the mid-mid contact gives the highest conductance, and the m-mid and o-mid have a value in the middle. The Seebeck results do not show large enhancement (all are less than 20μV/K).

6.4.4. Pendulum behaviour of the Complex molecules

Previous work [20], [21] has shown that changing the geometry of a molecular complex with localized orbitals can shift the position of the 'Fano' resonance as the complex moves relative to the molecule. I therefore, investigate if the chlorine atoms attached to the palladium atom can modify the transport behaviour by moving them in a 'pendulum' motion. First, the energy barrier for this rotation is calculated. The chlorine atoms are rotated by an angle θ around the N-N axis of PdP and PdM, ($\theta = 0°$ is the optimum geometry). Figure 6.14 shows the Energy barrier to rotation is low in both the Pd^P and Pd^M molecules (< 0.05eV) for angles between θ=10 and -50°.
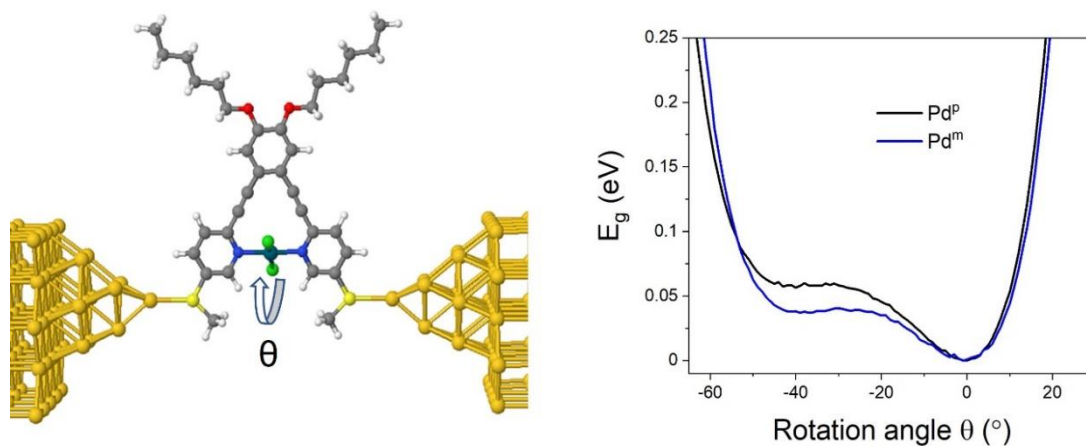
Figure (6.14): Ground state energy as a function of rotation angle θ, where the Cl atoms are rotated around the N-N bond in both Pd^P and Pd^M. For simplicity, $\theta = 0°$ is the optimum angle of $PdCl_2$ at the optimum geometry.

I then calculate the transmission coefficient $T(E)$ as a function of the rotation angle θ, and the results for the Pd^P molecule are shown in Figure 6.15. This shows that only the HOMO resonance (which has the Fano line shape) changes with the rotation angle and zooming in on this region shows that the width of this resonance changes and is also shifted by approximately 0.2eV. However, this shifting happens well away from the Fermi energy and therefore I expect that this motion does not play any role in the molecular conductance. I find similar behaviour for the equivalent calculation of the Pd^M molecule.
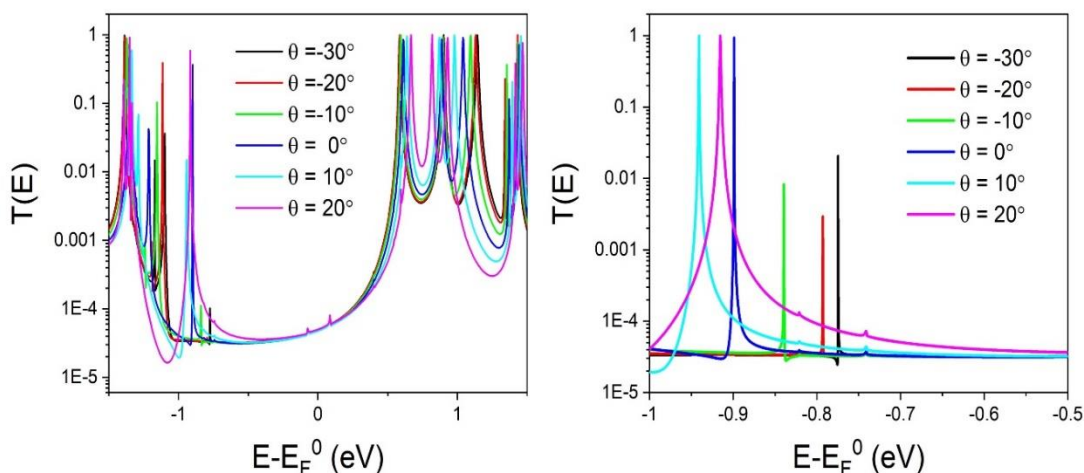
Figure (6.15): (left) T(E) against energy E for rotation angle θ about the equilibrium position 0° in molecule Pd^P. (right) Zoom in on HOMO resonance with the Fano line shape. The overall results are not affected by this shift in the Fano resonance, because it happens away from the electrode Fermi energy.

6.5. Conclusion

I have studied a series of palladium complexes to determine how the addition of the complex to the ligand can modify the electron transport behaviour in terms of quantum interference. I show that the transport behaviour for the case when the junction is formed through attachment to the SME anchor groups follows the expected behaviour in the case of the ligand molecules. The para connected L^P gives a higher conductance than the meta connected L^M, and in the case of the addition of the palladium complex the conductance is enhanced for both. The fact that the conductance of the meta-complex is lower than the para shows that the addition of the palladium atom does not disrupt the transport path, which is through the ligand part of the molecule.

The complex structure of these molecules leads to multiple binding locations for attachment to gold electrodes and therefore multiple junction configurations can be formed. Therefore, I expect the measurement of these molecules to show multiple measured conductance values. However, the fact that the Fermi energy sits in the middle of the transport gap and the complex only introduces a Fano resonance at a much lower energy, which is not greatly modified by the pendulum motion of the chlorine atoms, the Seebeck coefficient is predicted to be small for all four molecules. The different junction geometries do not enhance the Seebeck value either. Finally, the predicted pendulum motion of the chlorine atoms is shown to modify the behaviour of the HOMO resonance, but this feature happens well away from the Fermi energy, so it is expected not to play a role in the conductance or thermoelectric response of the complexed molecule.

Bibliography

[1] Lambert, C.J., 2015. Basic concepts of quantum interference and electron transport in single-molecule electronics. *Chemical Society Reviews*, *44*(4), pp.875-888.

[2] Hong, W., Manrique, D.Z., Moreno-García, P., Gulcur, M., Mishchenko, A., Lambert, C.J., Bryce, M.R. and Wandlowski, T., 2012. Single molecular conductance of tolanes: experimental and theoretical study on the junction evolution dependent on the anchoring group. *Journal of the American Chemical Society*, *134*(4), pp.2292-2304.

[3] Moreno-García, P., Gulcur, M., Manrique, D.Z., Pope, T., Hong, W., Kaliginedi, V., Huang, C., Batsanov, A.S., Bryce, M.R., Lambert, C. and Wandlowski, T., 2013. Single-molecule conductance of functionalized oligoynes: length dependence and junction evolution. *Journal of the American Chemical Society*, *135*(33), pp.12228-12240.

[4] Manrique, D.Z., Huang, C., Baghernejad, M., Zhao, X., Al-Owaedi, O.A., Sadeghi, H., Kaliginedi, V., Hong, W., Gulcur, M., Wandlowski, T. and Bryce, M.R., 2015. A quantum circuit rule for interference effects in single-molecule electrical junctions. *Nature communications*, *6*(1), pp.1-8.

[5] Herrer, I.L., Ismael, A.K., Milan, D.C., Vezzoli, A., Martín, S., Gonzalez-Orive, A., Grace, I., Lambert, C., Serrano, J.L., Nichols, R.J. and Cea, P., 2018. Unconventional single-molecule conductance behavior for a new heterocyclic anchoring group: pyrazolyl. *The journal of physical chemistry letters*, *9*(18), pp.5364-5372.

[6] Davidson, R.J., Milan, D.C., Al-Owaedi, O.A., Ismael, A.K., Nichols, R.J., Higgins, S.J., Lambert, C.J., Yufit, D.S. and Beeby, A., 2018. Conductance of 'bare-bones' tripodal molecular wires. *RSC advances*, *8*(42), pp.23585-23590.

[7] Herrer, L., Ismael, A., Martín, S., Milan, D.C., Serrano, J.L., Nichols, R.J., Lambert, C. and Cea, P., 2019. Single molecule vs. large area design of molecular electronic devices incorporating an efficient 2-aminepyridine double anchoring group. *Nanoscale*, *11*(34), pp.15871-15880.

[8] O'Driscoll, L.J. and Bryce, M.R., 2021. A review of oligo (arylene ethynylene) derivatives in molecular junctions. *Nanoscale*, *13*(24), pp.10668-10711.

[9] Wang, X., Ismael, A., Ning, S., Althobaiti, H., Al-Jobory, A., Girovsky, J., Astier, H.P., O'Driscoll, L.J., Bryce, M.R., Lambert, C.J. and Ford, C.J., 2022. Electrostatic Fermi level tuning in large-scale self-assembled monolayers of oligo (phenylene–ethynylene) derivatives. *Nanoscale Horizons*, *7*(10), pp.1201-1209.

[10] Liu, S.X., Ismael, A.K., Al-Jobory, A. and Lambert, C.J., 2023. Signatures of Room-Temperature Quantum Interference in Molecular Junctions. *Accounts of chemical research*, *56*(3), pp.322-331.

[11] Camarasa-Gómez, M., Hernangómez-Pérez, D., Inkpen, M.S., Lovat, G., Fung, E.D., Roy, X., Venkataraman, L. and Evers, F., 2020. Mechanically Tunable Quantum Interference in Ferrocene-Based Single-Molecule Junctions. *Nano Letters*, *20*(9), pp.6381-6386.

[12] Wilkinson, L.A., Bennett, T.L., Grace, I.M., Hamill, J., Wang, X., Au-Yong, S., Ismael, A., Jarvis, S.P., Hou, S., Albrecht, T. and Cohen, L.F., 2022. Assembly, structure and thermoelectric properties of 1, 1′-dialkynylferrocene 'hinges'. *Chemical Science*, *13*(28), pp.8380-8387.

[13] Milan, D.C., Vezzoli, A., Planje, I.J. and Low, P.J., 2018. Metal bis (acetylide) complex molecular wires: concepts and design strategies. *Dalton Transactions*, *47*(40), pp.14125-14138.

[14] Bennett, T.L., Alshammari, M., Au-Yong, S., Almutlg, A., Wang, X., Wilkinson, L.A., Albrecht, T., Jarvis, S.P., Cohen, L.F., Ismael, A. and Lambert, C.J., 2022. Multi-component self-assembled molecular-electronic films: towards new high-performance thermoelectric systems. *Chemical Science*, *13*(18), pp.5176-5185.

[15] Ponce, J., Arroyo, C.R., Tatay, S., Frisenda, R., Gaviña, P., Aravena, D., Ruiz, E., Van Der Zant, H.S. and Coronado, E., 2014. Effect of metal complexation on the conductance of single-molecular wires measured at room temperature. *Journal of the American Chemical Society*, *136*(23), pp.8314-8322.

[16] Al-Owaedi, O.A., Milan, D.C., Oerthel, M.C., Bock, S., Yufit, D.S., Howard, J.A., Higgins, S.J., Nichols, R.J., Lambert, C.J., Bryce, M.R. and Low, P.J., 2016. Experimental and computational studies of the single-molecule conductance of Ru (II) and Pt (II) trans-Bis (acetylide) complexes. *Organometallics*, *35*(17), pp.2944-2954.

[17] Schwarz, F., Kastlunger, G., Lissel, F., Egler-Lucas, C., Semenov, S.N., Venkatesan, K., Berke, H., Stadler, R. and Lörtscher, E., 2016. Field-induced conductance switching by charge-state alternation in organometallic single-molecule junctions. *Nature nanotechnology*, *11*(2), pp.170-176.

[18] Frisenda, R., Harzmann, G.D., Celis Gil, J.A., Thijssen, J.M., Mayor, M. and Van Der Zant, H.S., 2016. Stretching-induced conductance increase in a spin-crossover molecule. *Nano letters*, *16*(8), pp.4733-4737.

[19] González, M.T., Ismael, A.K., Garcia-Iglesias, M., Leary, E., Rubio-Bollinger, G., Grace, I., Gonzalez-Rodriguez, D., Torres, T., Lambert, C.J. and Agrait, N., 2021. Interference Controls Conductance in Phthalocyanine Molecular Junctions. *The Journal of Physical Chemistry C*, *125*(27), pp.15035-15043.

[20] Papadopoulos, T.A., Grace, I.M. and Lambert, C.J., 2006. Control of electron transport through Fano resonances in molecular wires. *Physical review b*, *74*(19), p.193306.

[21] Vezzoli, A., Grace, I., Brooke, C., Wang, K., Lambert, C.J., Xu, B., Nichols, R.J. and Higgins, S.J., 2015. Gating of single molecule junction conductance by charge transfer complex formation. *Nanoscale*, *7*(45), pp.18949-18955.

Chapter 7

Summary and Future works

This thesis has theoretically investigated the thermoelectric behaviour of single molecules using density functional theory (DFT) in combination with Green's function scattering techniques. Their electrical conductance G and the Seebeck S coefficient have been evaluated with the aim of understanding fundamentals of their transport properties, which may underpin future designs for high performance thermoelectric materials. However, if we are interested in increasing the efficiency of molecular nanodevices, we need to do more than merely calculate the G and S. The technical applicability of these devices is governed by their thermoelectric efficiency, which is characterised by the dimensionless figure of merit ZT, defined by $ZT = GS^2T/(G_{th}^{el} + G_{th}^{ph})$, where G_{th}^{el} and G_{th}^{ph} are electron and phonon thermal conductance, respectively. For the first suggestion, it would be of interest to compute the thermal conductance for the series of molecules that have been studied in this thesis. The approach to performing phonon transport calculations an extensions of methodologies developed for phonon transport in inhomogeneous media [1] and is almost identical to that of the electron transport calculation but with a few different input parameters [2].

The figure of merit should be larger than unity for an efficient thermoelectric device, and therefore, enhancement of G and S and suppression of thermal conductance are needed for efficient conversion of heat into electricity. Several parameters can modify the thermoelectric properties of molecular junctions such as the length of the molecule, the chemical nature of the anchor groups or the presence of the side groups. The Fano resonance feature in chapter 5 had

no role in enhancing the Seebeck coefficient, because of the simple structure of the pendant group and its lack of degrees of freedom. Thus, the chemical modification of the side group to be more complicated will offer many degrees of freedom to manipulate and then tune this resonance to be near the Fermi level of the electrodes [3], [4].

Another suggestion for this research is to change the molecular core structure to have two positions of pendant groups. Since one position of a side group has an important influence on the electron transport due to quantum interference effects, I think that adding two of them may enhance the thermopower even more [5]. According to this study [6], it has been shown that thermal conductance is suppressed with increasing the number of differing length pendant branches in molecules (a molecular Christmas trees). Furthermore, Charge transfer complexes [7] by adding an electron acceptor molecule (TCNQ) or donor (TTF) are another mechanism for regulating quantum interference.

In chapter 6, I have investigated the transport properties of para- and meta-connected molecules with and without metal atoms (i.e. $PdCl_2$), and the results showed that the presence of this metal atom in molecular wires results in a slight increase in the conductance due to the shift of the LUMO resonance to the Fermi energy. In this project it might be useful to think about studying the π-stacking of these molecules in more detail, understanding electron transport through them, and how different configurations may control QI [8]–[10]. The weak interaction between parallel π-stacked molecular systems may exhibit low conductance due to the appearance of destructive interference feature, and the decrease in conductance might indicate an increase in the thermopower. Moreover, the charge transport depends not only on the nature of ligands but also on the type of metal ion entrapped in the complex, thus studying a series of different metal ions, such as Zn, Fe, Cu, Co, Ni and Mn, is of fundamental interest to investigate their effect on electron transport. It has been found that the molecular energy levels can be tuned relative to the Fermi energy of the electrodes through the choice of the metal atom [11]. Besides

that, it would be interesting to calculate the charge transfer of these different metal elements, and study how the electron transfer between the metal and the molecular backbone would affect the transmission and the Seebeck behaviours. Furthermore, since the palladium is attached to two Cl atoms we can apply a reduction process by taking off both Cl atoms, which may cause a shift in the position of the electrode Fermi energy to the other side near the Fano resonance, leading to more enhancement in the conductance [11].

The other possibility to improve this work is to investigate other types of molecules containing Pt and Pd atoms for different connectivity [12], [13]. Platinum is more than 60% heavier than palladium, and thus it would be interesting to understand the role of the mass of the metal atom in terms of the thermal conductance.

Finally, alternative electrode materials for molecular electronics such as using graphene electrodes in all these projects is another interesting point to consider. Graphene as an electrode requires new anchor groups capable of preserving coherent electron transport across the molecule-graphene interface, and its unique properties make it an ideal electrode material for molecular electronics [14]–[16].

Bibliography

[1]   Kambili, A., Fagas, G., Fal'ko, V.I. and Lambert, C.J., 1999. Phonon-mediated thermal conductance of mesoscopic wires with rough edges. *Physical review b*, *60*(23), p.15593.

[2]   Sadeghi, H., 2019. Quantum and phonon interference-enhanced molecular-scale thermoelectricity. *The Journal of Physical Chemistry C*, *123*(20), pp.12556-12562.

[3]   Papadopoulos, T.A., Grace, I.M. and Lambert, C.J., 2006. Control of electron transport through Fano resonances in molecular wires. *Physical review b*, *74*(19), p.193306.

[4]   Ismael, A.K., Al-Jobory, A., Grace, I. and Lambert, C.J., 2017. Discriminating single-molecule sensing by crown-ether-based molecular junctions. *The Journal of chemical physics*, *146*(6), p.064704.

[5]   Valkenier, H., Guédon, C.M., Markussen, T., Thygesen, K.S., van der Molen, S.J. and Hummelen, J.C., 2014. Cross-conjugation and quantum interference: a general correlation?. *Physical Chemistry Chemical Physics*, *16*(2), pp.653-662.

[6]   Famili, M., Grace, I., Sadeghi, H. and Lambert, C.J., 2017. Suppression of phonon transport in molecular Christmas trees. *ChemPhysChem*, *18*(10), pp.1234-1241.

[7]   Wang, K., Vezzoli, A., Grace, I.M., McLaughlin, M., Nichols, R.J., Xu, B., Lambert, C.J. and Higgins, S.J., 2019. Charge transfer complexation boosts molecular conductance through Fermi level pinning. *Chemical science*, *10*(8), pp.2396-2403.

[8]   Al-Khaykanee, M.K., Ismael, A.K., Grace, I. and Lambert, C.J., 2018. Oscillating Seebeck coefficients in π-stacked molecular junctions. *RSC advances*, *8*(44), pp.24711-24715.

[9]   Shen, P., Huang, M., Qian, J., Li, J., Ding, S., Zhou, X.S., Xu, B., Zhao, Z. and Tang, B.Z., 2020. Achieving efficient multichannel conductance in through-space conjugated single-molecule parallel circuits. *Angewandte Chemie*, *132*(11), pp.4611-4618.

[10]   Markin, A., Ismael, A.K., Davidson, R.J., Milan, D.C., Nichols, R.J., Higgins, S.J., Lambert, C.J., Hsu, Y.T., Yufit, D.S. and Beeby, A., 2020. Conductance Behavior of Tetraphenyl-Aza-BODIPYs. *The Journal of Physical Chemistry C*, *124*(12), pp.6479-6485.

[11] Al-Galiby, Q.H., Sadeghi, H., Algharagholy, L.A., Grace, I. and Lambert, C., 2016. Tuning the thermoelectric properties of metallo-porphyrins. *Nanoscale*, *8*(4), pp.2428-2433.

[12] J. Rees, M., 2005. Magnetic fields in the early universe. In *Cosmic Magnetic Fields* (pp. 1-8). Berlin, Heidelberg: Springer Berlin Heidelberg.

[13] García-Suárez, V.M., Rocha, A.R., Bailey, S.W., Lambert, C.J., Sanvito, S. and Ferrer, J., 2005. Conductance oscillations in zigzag platinum chains. *Physical review letters*, *95*(25), p.256804.

[14] Lu, Y., Merchant, C.A., Drndic, M. and Johnson, A.C., 2011. In situ electronic characterization of graphene nanoconstrictions fabricated in a transmission electron microscope. *Nano letters*, *11*(12), pp.5184-5188.

[15] Bailey, S., Visontai, D., Lambert, C.J., Bryce, M.R., Frampton, H. and Chappell, D., 2014. A study of planar anchor groups for graphene-based single-molecule electronics. *The Journal of chemical physics*, *140*(5), p.054708.

[16] Barreiro, A., Borrnert, F., Rummeli, M.H., Buchner, B. and Vandersypen, L.M., 2012. Graphene at high bias: Cracking, layer by layer sublimation, and fusing. *Nano letters*, *12*(4), pp.1873-1878.